Doctoral Dissertation
PhD program in Bioengineering and Medical-Surgical Sciences (35th Cycle)

Detecting neuromechanical properties of single motor unit by combining high-density electromyography and ultrafast ultrasonography

Marco Carbonaro

* * * * * *

Supervisors

Prof. Alberto Botter
Prof. Filippo Molinari
Prof. Marco Gazzoni

Doctoral Examination Committee:

Prof. Aleš Holobar, Referee, Institute of Computer Science, Faculty of Electrical Engineering and Computer Science, University of Maribor, Slovenia

Prof. Javier Navallas Irujo, Referee, Departamento de Ingeniería Eléctrica, Electrónica y de Comunicación Universidad Pública de Navarra, Pamplona, Spain

Politecnico di Torino – Università degli studi di Torino

October 2023

I hereby declare that, the contents and organisation of this dissertation constitute my own original work and does not compromise in any way the rights of third parties, including those relating to the security of personal data.

…….....

Turin, October, 2023
Marco Carbonaro

"..limits, liker fears, are often just an illusion."
Micheal J. Jordan

To my Family.

Thank you, Mum and Dad, for your unwavering support, encouragement, and understanding throughout my entire life.

Thank you, my brothers, Matteo and Andrea. Your belief in me has been a constant source of motivation.

This thesis is dedicated to the love of my life, Clelia.

Academic Acknowledgment

I would like to express my sincere appreciation and gratitude to the individuals and institutions who have played a significant role in the successful completion of my academic journey and research project.

First and foremost, I would like to thank my academic advisor, Prof. Alberto Botter, for giving me the opportunity to start this project with him. His expertise, patience, and dedication have been instrumental in shaping my research, refining my technical skills, and pushing me to reach my full potential. Thank you not only for being my supervisor, but also a guide and mentor.

I am also grateful to the senior LISiN members, Prof. Marco Gazzoni, Prof. Taian Vieira, and Dr. Giacinto Luigi Cerone, for their insightful feedback, encouragement, and the valuable knowledge they imparted during my research.

A part of this work has been carried-out in collaboration with Prof. Emma Hodson-Tole who assisted me with good advices during the first work of the project.

I would like to acknowledge Prof. Kristen Meiburger and Dr. Silvia Seoni for their collaboration in the field of ultrafast ultrasound and I hope we will continue working together in future.

My gratitude is also extended to Prof. Christer Grönlund for his help and fruitful discussion during the last work of my PhD. I also look forward to continuing the collaboration with Dr. Robin Rohlén in future endeavours and I am excited about the possibilities that lie ahead.

Without my fellow researcher Alessandra Giangrande, the successful completion of this project would have been significantly more challenging. We have shared our ideas, perspectives, and experiences. Your camaraderie and collaboration have enriched my academic journey and made it all the more enjoyable.

Summary

Advancements in surface electromyography and ultrasonography have provided new technologies for acquiring highly-informative experimental data, opening new avenues for innovative processing techniques. Surface electromyography detected with multiple electrodes over the muscle (high-density surface electromyography - HDsEMG) allows to study electrophysiological events in time and space domain enabling the decomposition of the signals into their constituent motor unit action potential trains. Similarly, owing to its high frame rate, ultrafast ultrasonography enables the detection of rapid tissue displacements associated with single motor unit activation. The combined use of these two complementary techniques has therefore the potential to provide a detailed neuromechanical characterization of motor units, from the neural excitation to the tissue strain. Currently, the feasibility of this integration, as well as the systematic evaluation of its limitations and advantages, are not described in literature. This type of assessment is necessary to guide future developments both in experimental signal acquisition and data processing, as well as to identify clinical applications that could benefit from this integration. In this context, this thesis describes and tests a novel approach aimed at providing a comprehensive description of individual motor units based on the combination of high-density electromyography and ultrafast ultrasonography. The workflow of this project was divided into three main topics.

In the first part, two methods integrating information from high-density surface electromyography and ultrafast ultrasound sequences to detect the characteristics of single motor units were developed, analyzed, and tested in simulated conditions. The first algorithm was based on spike-triggered averaging of the tissue velocity sequence, using single motor unit firings obtained from HDsEMG as trigger source. The second one was based on the correlation between spatio-temporal independent components decomposed from the ultrasound tissue velocity sequence and the neural input obtained from HDsEMG decomposition. Simulations were carried out to evaluate the performance of the proposed algorithms in identifying the anatomical characteristics of the motor unit for different levels of neural input and motor unit synchronization. The results demonstrated that both algorithms were suitable for anatomical and mechanical analyses of individual motor units,

with the second method providing better performance compared to the first one in terms of accuracy of MU territories identification.

Afterwards, the algorithms were tested in experimental conditions. In vivo high-density electromyography and ultrafast ultrasound were detected simultaneously from biceps brachii using a grid of electrodes transparent to ultrasound. The algorithms were applied and compared to expand upon the simulation results. The spatial association between motor unit action potential distributions and the corresponding muscle fiber displacement areas was observed, proving the feasibility of the proposed approach. Multivariate analysis revealed the dependence of this association on the depth of the motor unit territory. Although both the suggested approaches were found to be feasible for the in vivo identification of motor unit fiber location in the muscle cross-section, the experimental results confirmed the simulations, indicating higher robustness of the algorithm based on the spatio-temporal tissue velocity decomposition.

The final part of the project focused on the ultrasound components decomposed from the tissue velocity sequence, being the accurate identification of these components of crucial importance for the performance of the combined algorithm based on this spatio-temporal decomposition. This study introduced a new criterion based on the spatial repeatability to improve the selection of the decomposed ultrasound components putatively associated with actual motor unit activity. Experimental results showed that only a subgroup of the initial components were highly repeatable across sequences of 2-s epochs. Moreover, repeatable components were those displaying the highest association with the motor unit action potential firings, identified independently from HDsEMG. The proposed criterion for the selection of spatial components can be used to reduce the number of ultrasound components to process, with possible implications in the improvement of the combined algorithm proposed in the previous studies.

In conclusion, the integrated approach combining high-density electromyography and ultrafast ultrasonography was proved suitable for assessing the electromechanical properties of motor units in vivo, opening interesting perspectives into the non-invasive investigation of skeletal muscles and their control. This research lays the basis for future developments and applications in the investigation of fundamental pathophysiological aspects of muscle function, such as studying changes in neuromechanical properties associated with aging, training, rehabilitation interventions, or neuromuscular diseases.

Table of Contents

1. Aim and structure of the project 1

1.1 Structure of the thesis 2
1.2 References 3

2. Background and state of art 5

2.1 Anatomy and physiology of the motor unit 5

2.1.1 Muscle fiber 6
2.1.2 Motoneuron 6
2.1.3 MU territories 6

2.2 MU properties 8

2.2.1 Electrical properties: action potential 8
2.2.2 Mechanical properties 10
2.2.3 Electromechanical properties: the excitation-contraction coupling 12
2.2.4 MU recruitment and rate coding 12

2.3 Methods to assess muscle excitation and contraction 14

2.3.1 Electromyography 14
2.3.2 Mechanomyography 17
2.3.3 Magnetic resonance imaging 18
2.3.4 Ultrasonography 18
2.3.5 Combination of techniques 23

2.4 References 27

3. Topic 1 39

3.1 Integration of HDsEMG and UUS data 39

3.1.1 Algorithm based on the averaging of the tissue velocity with single MU firings (*STA-based*) 41
3.1.2 Algorithm based on the decomposition of displacement velocity and correlation with MU firing activity (stICA-based) 42

3.2 Comparison of the algorithm for the detection of anatomical characteristic of single MU 45

3.2.1 Simulation model 46
3.2.2 Metrics for the performance assessment 49

3.3 Simulation results 50
3.4 Conclusions of the simulation study 55
3.5 References 56

4. Topic 2 59

4.1 In vivo testing of the HDsEMG and ultrafast US integration for single MU characterization 59
4.2 Methods 60

4.2.1 Algorithm 60
4.2.2 Experimental protocol 60
4.2.3 Data processing 63
4.2.4 Association between electrical and mechanical activity 64

4.3 Experimental results 65

4.3.1 General comments 65
4.3.2 Association between electrical and mechanical activity 65

4.4 Discussion of the experimental analysis 66

4.4.1 HDsEMG decomposition as gold standard 66
4.4.2 Comparison with simulation results and limitations 68
4.4.3 Generalization of this experimental result 70

4.5 Experimental comparison between STA and STICA approach 71

4.5.1 Methodological considerations 71
4.5.2 Results 72

4.6 References 74

5. Topic 3 79

5.1 Spatial repeatability approach to enhance the identification of US components associated with MU activity 79
5.2 Methods 81

5.2.1 Experimental protocol 81
5.2.2 UUS and HDsEMG data processing 81
5.2.3 Spatiotemporal decomposition of displacement velocity image 83
5.2.4 Repeatability analysis: selecting similar spatial maps across epochs (intra-sequence approach) 83
5.2.5 Association of components with MUs from HDsEMG 83
5.2.6 Number of MU-matched components: intra- and full-sequence approaches comparison 85

5.2.7 Statistical analysis 85
5.3 Results 86
5.3.1 MU identification and repeatable components 86
5.3.2 Association of components with MUs from HDsEMG 86
5.4 Discussion 90
5.5 References 95
6. Conclusions 97
6.1 Main findings 97
6.2 Relevance and future works 99
6.3 References 100
7. List of Publications (2019-2023) 103
Peer-reviewed publications in international journals 103
Peer-reviewed international conference proceedings 103
Conference abstracts 104

List of Figures

Figure 2.1 Schematic representation of three MU territories. 7
Figure 2.2 Action potential. 9
Figure 2.3 Single motor unit twitch. 11
Figure 2.4 Example of MU recruitment. 13
Figure 2.5 Schematic representation of the generation of EMG. 15
Figure 2.6 MU decomposition. 17
Figure 2.7 Example of conventional US imaging for studying MU recruitment. 19
Figure 2.8 Example of tissue velocity imaging in electrically-elicited contractions 22
Figure 2.9 Simultaneous recording of EMG and MMG signals. 24
Figure 2.10 Fasciculation investigation with combine EMG and US analysis. 25
Figure 2.11 High-density surface electromyography (HDsEMG) ultrasound-transparent electrodes. 26
Figure 3.1 Integration of HDsEMG and ultrafast US. 40
Figure 3.2 Theoretical considerations about muscle motion. 41
Figure 3.3 Spike Triggered Averaging of the tissue velocities. 41
Figure 3.4 Overview of the algorithm based on the decomposition of tissue velocities and correlation with MU firings. 44
Figure 3.5 Simulation model of cylindrical muscle. 47
Figure 3.6 Mechanical model of single motor units. 48
Figure 3.7 Simulation results. 51
Figure 3.8 Temporal analysis results. 53
Figure 3.9 Examples of detected MU with STICA. 54
Figure 3.10 Medio-lateral US-EMG coordinates correlation. 55
Figure 4.1 Experimental setup overview. 61
Figure 4.2 Experimental procedure. 62
Figure 4.3 Processing of HDsEMG and UUS data. 63
Figure 4.4 *In vivo* identified MU. 65
Figure 4.5 Group results of experimental data. 67
Figure 4.6 Effect of the muscle physiological cross-sectional area (PCSA) on the transversal MUAP amplitude distribution. 69
Figure 4.7 Comparison of MU identifications with STA and STICA 72
Figure 4.8 STA and STICA distances between ultrasound and EMG centroid. 73
Figure 5.1 Illustration of the ultrasound data processing and intra-sequence repeatability approach. 82
Figure 5.2 Association of components with MUs from HDsEMG. 84
Figure 5.3 Noise threshold computation. 85
Figure 5.4 Example of repeatability analysis. 87

Figure 5.5 Relationship between Jaccard Similarity Coefficient (JSC) and putative twitches with the highest spike-triggered averaged twitch amplitude. 88
Figure 5.5 Examples of spatial maps. 88
Figure 5.7 Three representative matches between repeatable components and the motor units (MUs). 89
Figure 5.8 Examples of multiple components associated with the same MU. 93
Figure 6.1 Output of the EMG-US method 98

List of Tables

Table 2.1 Neural-Muscle electrochemical and mechanical signaling. 12
Table 3.1 Parameters of the cylindrical muscle model. 46
Table 5.1 Descriptive statistics about the motor unit-matched repeatable components. 89
Table 5.2 Descriptive statistics about the recordings, decomposed EMG MUs and ultrasound components. 92

Detecting neuromechanical properties of single motor unit by combining high-density electromyography and ultrafast ultrasonography

General objective of this thesis

Develop methods and technologies integrating high-density surface electromyography and ultrafast ultrasound to provide a complete neuromechanical description of single motor units: from neural excitation to force production.

Background knowledge for the reader

Anatomy and physiology of the skeletal muscle: motor unit mechanical and electrical properties

Methods for the assessment of the muscle excitation and contraction: from the global to the motor unit level.

Topics addressed in this thesis

Topic 1

Development, analysis, and testing of two algorithms designed to detect single motor units' characteristics by integrating high-density surface electromyography and ultrafast ultrasonography

Topic 2

Application of the developed approaches to an experimental protocol of simultaneous high-density electromyographic and ultrafast ultrasound measurements

Topic 3

Enhancement of the decomposition of displacement velocities from ultrafast ultrasound: repeatability of spatial components across short epochs as a criterion of component selection.

Chapter 1

Aim and structure of the project

The PhD project presented in this thesis aimed to develop innovative methods for the in vivo characterization of electrical and mechanical single motor unit properties using an integrated approach based on high-density electromyography and ultrafast ultrasound. This unique combination can provide a complete neuromechanical description of individual motor units from neural excitation to the resulting tissue displacement.

Surface electromyography and ultrasonography can be considered complementary tools to investigate the neuromuscular system. Indeed, they measure different quantities related to muscle contraction: electrophysiological features that carry information about muscle excitation and fiber membrane properties [2], anatomical muscle tissue characteristics that provide information about the morphology of the muscle-tendon unit and its active and passive movement [1]. The detection of both EMG signals and ultrasound images has considerably improved over the past 20 years because of technological advancements [3], [4]. This has enhanced the amount of information available in experimental data and opened up new possibilities for innovative processing techniques. For example, by recording electromyographic signals from several locations above the skin (high-density surface electromyography), it is possible to describe electrical events with high spatial resolution, allowing the decomposition of the signal in the constituent motor units [5]. New ultrasound systems provide the possibility of sampling images at a high frame rate (over thousands per second), leading to a new branch of ultrasonography (ultrafast ultrasonography) that enables the description of fast tissue displacement, such as those associated to single motor unit activation [6], [7]. Therefore, the combination of electromyography and ultrasonography has the potential to provide key insights into the

electromechanical properties of skeletal muscles and fine details of their functioning, not only at the global level, but also at single motor unit level.

1.1 Structure of the thesis

The first part of the thesis (Chapter 2) aims to provide a background about the physiology of muscle contraction and its fundamental constituents, with emphasis on the electrical and mechanical properties of the motor unit. Subsequently, the state-of-the-art of the current methods to assess excitation and contraction of the muscle (and motor unit) is presented, along with recent works that combine electromyography with ultrasonography.

The workflow of the project is presented on three topics.

The first topic (Chapter 3) describes the development, analysis, and testing of two methods designed to detect the anatomical characteristics of single motor units by integrating the information extracted from high-density surface electromyographic signals and ultrafast ultrasound sequences. The two algorithms were compared in a simulated environment to control the contraction and motor unit parameters, and systematically assess the outcomes of the algorithms. A simulation model of electromyographic signals was adapted by adding the model generating tissue velocities in the muscle cross-section. This study provided a better understanding of the advantages and drawbacks of the tested US-EMG approaches, and allowed to set the basic algorithms' parameters that were fine-tuned in the experimental study.

The second topic (Chapter 4) concerns the application of the developed approaches to an experimental protocol including high-density electromyography and ultrafast ultrasonography measurements of biceps brachii contraction. The algorithms were applied to experimental data and compared to expand the simulation results and provide evidence of their suitability for in vivo anatomical and mechanical characterization of single motor units. The best-performing algorithm was further investigated with the aim of studying the local association between the action potentials of single motor units and the corresponding muscle tissue displacement. This investigation helped to evaluate to what extent the results obtained in simulated conditions apply to the in vivo data and to enlighten on the experimental limitations of the technique.

The third topic (Chapter 5) of this thesis focuses on the assessment of the repeatability of the identification of displacement areas computed from experimental ultrafast ultrasound data associated to motor unit activity. A new process based on the temporal segmentation of the recorded signals in short epochs was used to enhance the estimation of motor unit activity considering the spatial repeatability of the decomposed ultrasound components throughout the contraction. High-density surface electromyography served as a ground truth for verifying that spatially repeatable components were indeed associated with motor unit activity.

In the Conclusions (Chapter 6), the applied relevance of the thesis findings is discussed considering the future developments of the technique and its applications for the investigation of fundamental pathophysiological aspects of muscle function, such as the study of changes in neuromechanical properties resulting from aging or neurodegenerative diseases.

1.2 References

[1] J. V. Basmajian and C. J. de Luca, *Muscles Alive: Their Functions Revealed by Electromyography*. Baltimore; London; Sydney: Williams & Wilkins, 1985. doi: 10.1249/00005768-197621000-00002.

[2] P. W. Hodges, L. H. M. Pengel, R. D. Herbert, and S. C. Gandevia, 'Measurement of muscle contraction with ultrasound imaging', *Muscle Nerve*, vol. 27, no. 6, pp. 682–692, 2003, doi: 10.1002/mus.10375.

[3] R. Merletti, M. Aventaggiato, A. Botter, A. Holobar, H. Marateb, and T. M. M. Vieira, 'Advances in surface EMG: Recent progress in detection and processing techniques', *Crit. Rev. Biomed. Eng.*, vol. 38, no. 4, pp. 305–45, 2010, doi: 10.1615/CritRevBiomedEng.v38.i4.10.

[4] M. Tanter and M. Fink, 'Ultrafast imaging in biomedical ultrasound', *IEEE Trans. Ultrason. Ferroelectr. Freq. Control*, vol. 61, no. 1, pp. 102–119, 2014, doi: 10.1109/TUFFC.2014.2882.

[5] A. Holobar and D. Farina, 'Noninvasive Neural Interfacing With Wearable Muscle Sensors: Combining Convolutive Blind Source Separation Methods and Deep Learning Techniques for Neural Decoding', *IEEE Signal Process. Mag.*, vol. 38, no. 4, pp. 103–118, Jul. 2021, doi: 10.1109/MSP.2021.3057051.

[6] T. Deffieux, J. L. Gennisson, M. Tanter, M. Fink, and A. Nordez, 'Ultrafast imaging of in vivo muscle contraction using ultrasound', *Appl. Phys. Lett.*, vol. 89, no. 18, pp. 2006–2008, 2006, doi: 10.1063/1.2378616.

[7] T. Deffieux, J. L. Gennisson, M. Tanter, and M. Fink, 'Assessment of the mechanical properties of the musculoskeletal system using 2-D and 3-D very high frame rate ultrasound', *IEEE Trans. Ultrason. Ferroelectr. Freq. Control*, vol. 55, no. 10, pp. 2177–2190, 2008, doi: 10.1109/TUFFC.917.

Chapter 2

Background and state of art

Muscle contraction is associated with a cascade of electrochemical and mechanical events, from the excitation of motor unit's muscle fibers to the binding of actin-myosin and thus the generation of muscle force [1], [2]. The motor unit (MU) is the basic functional unit that can be activated and controlled by the neuromuscular system to produce and grade the muscle force [3]. In this Chapter, the basic anatomy and physiology of the MU is reported describing all its elements and properties with a particular focus on electrical and mechanical characteristics. Afterwards, an overview of all the methods and technologies to assess muscle excitation and contraction are reported with a focus on those relevant for the study of anatomical, electrical and mechanical characteristics of the MU. The final part of this Chapter includes an overview of the studies combining some of these techniques to achieve an in-depth understanding of all the mechanisms involved in the muscle contraction and excitation.

2.1 Anatomy and physiology of the motor unit

The MU anatomically consists in a group of muscle fibers and an alpha motoneuron innervating them [3]. The peripheral element of the MU (i.e. the group of fibers) is also known as muscle unit. Whereas the motoneuron belongs to the central nervous system (CNS). Each motoneuron innervates several muscle fibers (ranging from about 5 to 2000) [4], thus few hundreds of motoneurons activate the thousands of fibers composing each muscle.

2.1.1 Muscle fiber

The muscle fibers are the cells constituting the muscle tissue. The skeletal muscle is composed of bundles of striated muscle fibers called fascicles. Inside the muscle fiber, the sarcomeres are repeated in small bundles (named as myofibril). The sarcomeres represent the basic contractile units of the muscle [1]. These units comprise two interdigitated myofilaments, known as thick and thin filaments: the thin one is mostly composed of actin, whereas the thick one contains myosin. These proteins are also known as contractile proteins and their interactions (through the cross-bridge cycle) generate the sliding of the filaments relative to one another [5]. The force exerted by the fiber is a consequence of the concurrent cycling of this sliding of all its sarcomeres [6].

The fiber is surrounded by an excitable membrane: the sarcolemma. This membrane maintains a constant potential difference between the interior of the muscle fiber and extracellular environment. Another important anatomical structure is the sarcoplasmic reticulum which surrounds each myofibril with its channels releasing ions during the muscle fiber functioning.

An important characteristic of the muscle fiber is the cross-sectional area, which is usually known to increase between the type I, IIa, or IIb (session 2.2.2). However, the relative size of different fiber types appears to vary among human muscles and also between women and men.

The muscle fibers are activated (controlled) by the neural signals coming from the CNS. These signals are generated and conducted by neurons called motoneurons. In particular, the alpha motoneuron sends a control command that reaches the muscle fibers producing their synchronous contraction [1].

2.1.2 Motoneuron

The alpha motoneuron is a cell of the CNS which innervates a group of fibers, forming together the MU. It comprises three main anatomical structures: the soma, the axon, and the terminal branches. As all the neurons, the motoneuron has an excitable membrane (axolemma) with sodium-potassium channels that works to control the potential between the interior and exterior of the cells moving ions through the membrane. The control command of the motoneuron consists of an electric pulse traveling through the axon, branching out into axonal ramifications, and ultimately reaching the neuromuscular junctions of various MU fibers.

2.1.3 MU territories

Early investigations have shown that muscle units occupy specific regions of the muscle [3]. Therefore, the muscle fibers belonging to a single MU are limited within a specific area of the muscle cross-section known as the MU territory (Figure 2.1). The

number of MUs present in a muscle and the area they occupy within the muscle cross-section are dependent on the size of the muscle. In general, larger muscles typically have a greater number of MUs and occupy a larger area within the muscle cross-section, while smaller muscles tend to have fewer MUs and occupy a smaller area [7]. The size of the muscle directly influences the distribution and organization of MUs within its structure. Moreover, a given region of a muscle contains more intermingled MUs. In fact, within a MU territory, the corresponding fibers are intertwined with fibers from other MUs, resulting in overlapping MU territories within the same muscle cross-section region (Figure 2.1). In certain human muscles, the degree of overlapping between MUs can vary depending on the specific muscle with impacts on the coordination and control of the contractions. For example, fine-function muscles (small muscles, e.g. hand muscles [8]) have more MUs per unit volume.

The spatial arrangement of MU fibers within their territories lacks a consensus, and the MU territories are considered to be irregular in shape, circular, and oval [7], [9]. Several studies indicate that the distribution of MU fibers is not homogenous within the MU territory. Various descriptions have been provided, such as uniform distribution [10]

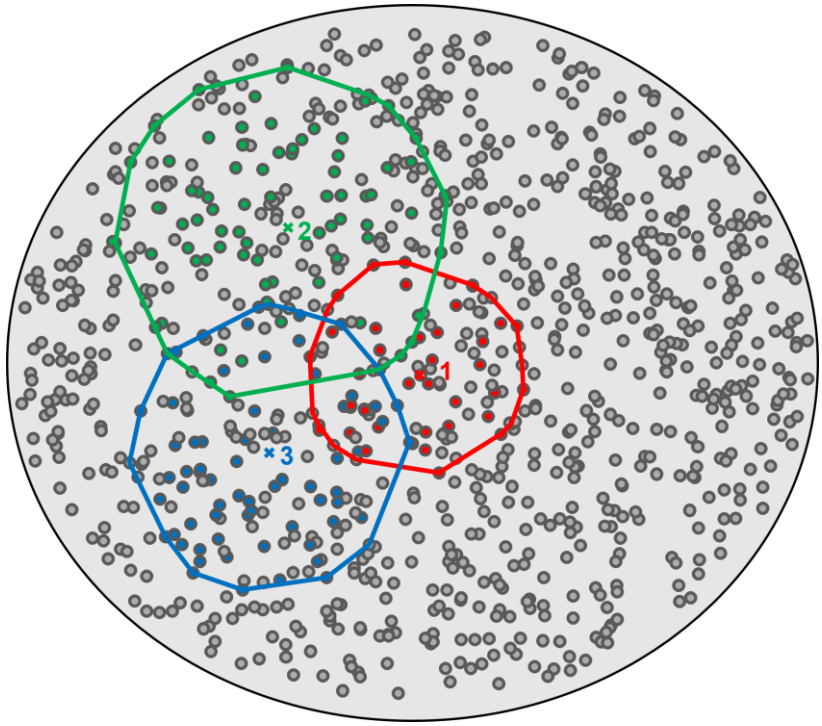

Figure 2.1 Schematic representation of three MU territories. Cross-sectional view of a cylindrical muscle comprising 1000 fibers. The muscle fibers are represented by small gray circles. Three example MUs whose territories overlap are shown highlighting the corresponding fibers in three different colors. The fibers colored in red belong to MU "1", the ones colored in green belong to MU "2", and the blue ones are of MU "3".

without localized clusters [3], even distribution [11], quasi-Gaussian pattern [12], and random arrangement [7]. The ratio between the number of fibers and the area of the territory of a MU exhibits different ranges depending on the type of MU [13].

The area occupied by a MU within the muscle cross-section is influenced by the number of muscle fibers it innervates, with larger MUs typically having larger territory areas. Due to the relationship between the number of MU fibers and the force exerted by a MU (session 2.2.2) and considering the skewed distribution of twitch forces among different MUs, the majority of MU territories within a muscle tend to be small in size. Since smaller MUs, which are more numerous, typically generate relatively lower twitch forces, their territory areas reflect this characteristic. Therefore, within a muscle, the majority of MUs have smaller territory areas due to their association with smaller twitch forces. This distribution pattern reflects the heterogeneity of MUs and their varying capabilities in force production (see next session 2.2.2).

2.2 MU properties

Muscle force and the production of movement is the result of a complex neural interaction occurring at the supraspinal level that generates the so-called neural drive to the spinal alpha-motoneurons. These neurons integrate the neural drive with the afferent, inhibitory or excitatory feedback to generate the neural input to the MU fibers. This signal is transmitted along the axons of the neurons, across the neuromuscular junction to the muscle fiber, and finally into the muscle fiber to the contractile proteins. The underlying mechanism that allows the electrical signal generation and transmission is the excitability of the nerve and muscle membranes (axolemma and sarcolemma) that has been described and modeled by Hodgkin & Huxley [5]. The different ions' concentration across the membrane is associated with a trans-membrane electrical potential that evolves in time and space due to local changes in ion's concentration (section 2.2.1). As a result of the propagation of this signal, all the fibers of a MU contract [6]. This contraction produces a force which is called mechanical twitch (section 2.2.2). These electrical (action potential) and mechanical (twitch) aspects are concatenated with a sequence of chemical events, and they are overall referred to as excitation-contraction coupling (section 2.2.3).

2.2.1 Electrical properties: action potential

At rest, the cell membrane is stable on a resting membrane potential of about 60 to 90 mV, and the inside is negative with respect to the outside. This resting potential is the result of a dynamic equilibrium of ionic distribution across the membrane, that is a balance between the positive and negative ions and concentration-gradient force experienced by each ion. This balance is ensured by specific voltage-dependent ions channels and ions pumps that force the ions' movement against the gradient of concentration. The shift in ions

(K^+, Na^+) across the membrane from inside to outside and vice versa produces changes on the membrane potential (i.e. depolarization and hyperpolarization). This movement of ions can be induced by chemical, electrical, or mechanical factor. Figure 2.2 shows the action potential as a voltage-time event which is characterized by four main phases: depolarization, overshoot (phase over 0 V), repolarization, and hyperpolarization. The action potential is an all-or-none electrical command that is issued by an excitable cell in response to inputs that it receives [1]. A neurotransmitter (i.e. acetylcholine, ACh) released at the synapse level (i.e. connection between to excitable cells) generates a synaptic potential that conducts and decreases in amplitude traveling along the cell membrane. If the sum of synaptic potentials reaches the axon with an amplitude over the trigger level (threshold), the action potential generates and propagates (Figure 2.2).

Each motoneuron conducts electrical pulses that determine the excitation of all muscle fibers belonging to a MU. Thus, both motoneuron and muscle fiber conduct the action potential. When the axonal (motoneuron) action potential reaches the neuromuscular junction of the muscle fiber, another action potential in the muscle fiber is propagated in both directions towards the tendon endings. As a result, each muscle fiber generates a single fiber action potential (SFAP). These SFAPs propagate along the muscle fibers, moving from the neuromuscular junction towards the tendon regions, triggering the contraction of the muscle fibers. The action potential is not only function of time but also of

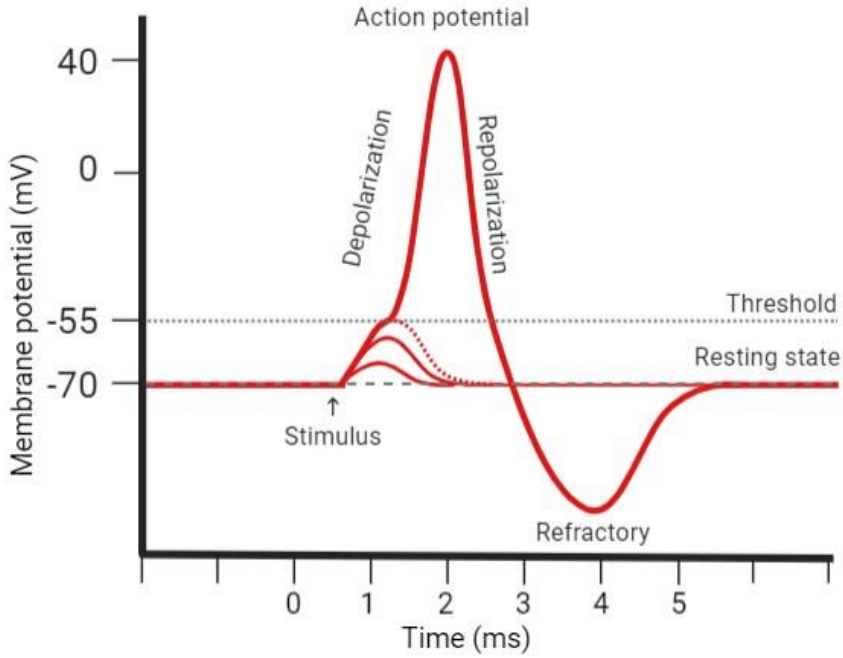

Figure 2.2 Action potential. Schematic diagram of the action potential with the characteristic phases: the stimulus, the depolarization, the overshoot (phase over 0 V), the repolarization, and the hyperpolarization (refractory period). Image originated in BioRender.com

space, as it spreads out along the muscle fiber. The velocity with which the action potential is propagated is called conduction velocity. When referring to the muscle fibers the conduction velocity mainly depends on their diameter: a higher conduction velocity corresponds to a larger fiber diameter. In healthy adult muscles, the conduction velocity is typically within the range of 1.5 to 6.5 m/s.

The synchronous sum of SFAPs belonging to the fibers of a single MU is referred to as compound motor unit action potential (MUAP). Consequently, each axonal action potential corresponds to a time-locked MUAP. These concepts are further discussed in the "Electromyography" section 2.3.1.

2.2.2 Mechanical properties

During contractions, the generated tensile force is accompanied by the displacement of the contracting and non-contracting fibers. The exerted force is, indeed, accompanied by the sliding of the thick and thin filaments [6], [14]. At the single-fiber level the development of force depends on the cycling of the cross-bridge attachment and detachment: the greater the number of cycles occurring at once, the greater the force.

The ability of muscle to generate power depends on its force capacity and shortening velocity (muscle mechanics) which in turn depend on the mechanical properties of the MU. The mechanical properties refer to the contractile behaviour in terms of force-time response of the MU. All the fibers of a MU contract in unison when excited by the neural input coming from its alpha motoneuron. This contraction produces a force (or tension) which is referred as the quantal contractive property of a MU: the *twitch* (Figure 2.3). This response in time is characterized by three components: the latent period (i.e. the time of the onset of the response after the input), the contraction period (i.e. the time from onset to the peak force), the relaxation period (i.e. the time it takes for the force to decline to zero). This response can be characterized by three measurements: the contraction time that corresponds to the contraction period, the magnitude of the peak (in terms of force or tension), and the half-relaxation time that is the time the force takes to decline to one-half of its peak value. The contraction time defines the MU as slow-twitch MU if the time is long, or as fast-twitch MU when the contraction is brief. The twitch force generated by MUs within a single muscle exhibits a wide range of variation, characterized by a highly skewed distribution. This distribution is characterized by the presence of numerous MUs that produce relatively small twitch forces, while only a few MUs generate large twitch forces. In other words, there is a significant diversity in the force-generating capabilities of MUs within a muscle, with a majority of MUs contributing to lower levels of force and a minority of MUs responsible for higher force outputs [15].

The actual force produced by an active MU during a contraction is greater since the input typically comprises a sequence of action potentials and subsequent overlapping twitch responses. The rate of received action potentials from the motor neuron determines the magnitude and smoothness of the motor unit force (force-frequency relation) [4], [16]. This

phenomenon, known as tetanus, can be unfused if the frequency of the inputs is low producing an irregular force profile, or fused when the force reaches a smooth plateau at higher frequency.

The resistance to fatigue is the ability of a MU to prevent the decline of force over time, due to the prolonged series of tetani. In general, the MUs are distinguished in fatigue-resistance and fatigable MUs. Combining the time and fatiguing properties, the MUs can be classified as slow-contracting, fatigue-resistant (type S), fast-contracting, fast to fatigue (type FF), and fast-contracting, fatigue resistant (type FR) [16].

Furthermore, histochemical, biochemical, and molecular properties of the muscle fibers, related to physiological properties (e.g. contraction speed, magnitude of force, fatigue resistance), can distinguish MU types [17], [18]. For example, the distinction between type I and II (based on the amount of ATPase activity), is associated respectively with slow- and fast- twitch muscle fibers. The type II can be further separated into two groups (IIa and IIb), defining the relative fatigue-resistance according to the oxidative state. The muscle fiber cross-sectional area is known to increase between the type I, IIa, or IIb. It is worth noting that smaller MUs are primarily composed of type I fibers, which tend to have smaller diameters compared to type II fibers. Type I fibers are more prevalent in smaller MUs. Conversely, larger MUs tend to have a higher proportion of type II fibers. These type II fibers have larger diameters and are more commonly found in larger MUs [19].

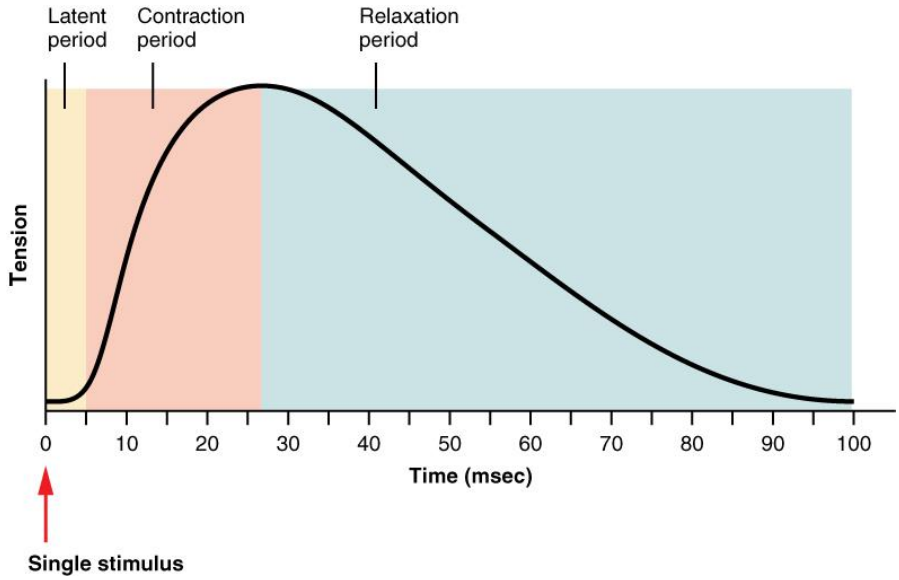

Figure 2.3 Single motor unit twitch. Scheme of the tension-time response of a single MU. Three components characterized the response: the latent period, the contraction period, and the relaxation period. The Author: OpenStax College; License: Creative Commons Attribution 3.0.

2.2.3 Electromechanical properties: the excitation-contraction coupling

When the action potential reaches the neuromuscular junction (connection between a neuron and muscle cell), the neurotransmitter diffuses triggering the generation of the action potential of the fiber membrane (i.e. the sarcolemma). Subsequent processes transform the sarcolemmal action potential into muscle fiber force [1]. These processes are referred to as excitation-contraction coupling. As already mentioned, the fiber force is produced by the sliding of the sarcomere contractile proteins. This molecular interactions (cross-bridge cycle) is in turn triggered by an increase of intracellular Ca^{2+} caused by the depolarization of the muscle membrane. The events linking the excitation and the contraction can be discerned into electrical and mechanical domains as summarized in Table 2.1.

2.2.4 MU recruitment and rate coding

The previous section explained that the force exerted by a muscle depends on several factors such as the types of MU and fiber. We mentioned that, the number of active MUs, defined as the MU recruitment, and the rate at which motoneurons discharge action potentials (rate coding), are two properties affecting the force production [1], [20].

Table 2.1 Neural-Muscle electrochemical and mechanical signaling.

		Sequence of events
Electrical domain	1	The arrival of a motoneuron action potential at the axon terminal leads to the release of ACh.
	2	ACh diffuses into the synaptic cleft and binds to receptors on the motor endplate of the muscle fiber causing a change in potential and triggering a muscle fiber action potential.
	3	The action potential travels through the sarcolemma opening calcium release channels, thus allowing Ca^{2+} ions to enter the sarcoplasm.
	4	The Ca^{2+} binds to troponin on the thin filament, which exposes the binding sites for myosin.
Mechanical domain	5	The thin filaments is pulled toward the center of the sarcomere after the binding to actin of myosin heads using ATP.
	6	ATP is used by the active transport pumps to restore a low level of Ca^{2+} in the sarcoplasm after Ca2+ release channels close.
	7	The troponin-tropomyosin complex returns to its original position, blocking the myosin-binding sites on actin.

ACh = acetylcholine, ATP = adenosine triphosphate

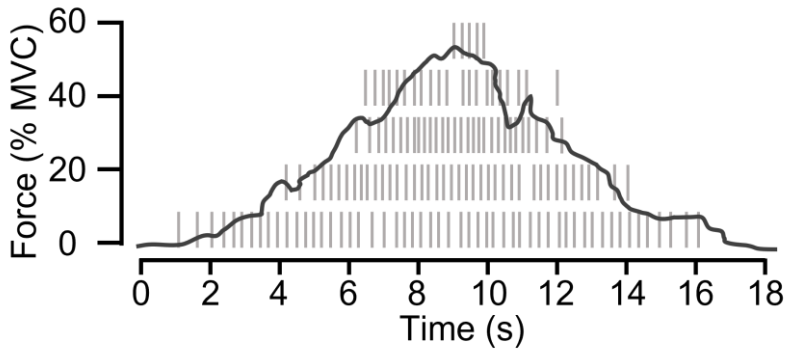

Figure 2.4 Example of MU recruitment. Recruitment and discharge pattern of five (of many) MUs during an isometric muscle contraction of increasing force up to 50% of the maximum voluntary contraction (MVC).

The sequence of MU activation has been shown to be relatively fixed: during the increase of exerted force additional MUs are activated/recruited. This is commonly known as orderly recruitment. The first recruited MU remains active as long as the force does not decrease and the increase of the force is related to the continuous recruitment of MUs (and increase of the rate of activation, see next paragraph). The recruitment of MUs is ordered such that smaller motoneurons with weaker muscle units (i.e. with low number of fibers) and longer contraction times are recruited first, followed by progressively larger motoneurons with stronger muscle units (i.e. with great number of fibers) and faster contraction times. This recruitment pattern forms the foundation of the size principle [21] and allows for graded muscle contractions and efficient motor control. The sequential activation of motor units in an orderly recruitment pattern primarily results from variances in motor neuron size, with smaller motor neurons having lower current requirements to reach the voltage threshold [15]. The recruitment threshold of MUs within a pool exhibits an exponential relationship, whereby a majority of MUs are recruited at lower force levels, while fewer units are progressively recruited as force requirements increase to moderate-to-high levels.

Moreover, the force contributed by a MU to an action depends on the rate at which the motoneuron discharges action potentials (force-frequency relation) [16]. The modulation of the discharge rate, referred to as rate coding, varies substantially across motor tasks. The rate coding together with the recruitment of more MUs are the strategies used by the CNS to control and modulate the force production (Figure 2.4). While the target force increases, more MUs are recruited and the discharge rate rises which means that earlier recruited MUs achieves greater discharge rate [15].

2.3 Methods to assess muscle excitation and contraction

Methods and technologies to assess muscle excitation and contraction play a crucial role in understanding the complex mechanisms and performance of the human musculoskeletal system, reported in the previous sections. Muscle excitation refers to the initiation of electrical signals that activate muscle fibers, while muscle contraction involves the generation of force by these fibers. Accurate assessment of these processes is essential for diagnosing and monitoring neuromuscular disorders, evaluating athletic performance, designing rehabilitation programs, and more in general advancing the knowledge of human movement.

2.3.1 Electromyography

Electromyography (EMG) is one of the most widely used techniques, which involves recording and analyzing the electrical activity produced by muscles during contraction [22]. Surface EMG provides non-invasive measurements by placing electrodes on the skin overlying the muscle of interest [23], while intramuscular EMG involves inserting fine needle electrodes directly into the muscle tissue for more in-deep recordings [24].

There exist many types of EMG techniques within the intramuscular EMG and surface EMG. These techniques differ for the detection systems, such as the type of electrode (e.g., single-fiber, concentric, etc.) and the use of multiple electrodes. The multielectrode EMG allows for simultaneous recordings to be performed in multiple locations, obtaining information about the MU territory [25], and enabling the decomposition between different MUAPs [26]. A similar technique is based on the insertion of a needle electrode in the muscle and its motion along a line allow recording electrical activity of the MU in multiple locations. This technique is known as scanning EMG [27]–[29] and its signal is a collection of MUAPs recorded in time and in space. This signal gives information on the changes of the electrical MU activity in relation to the relative distance between MU fibers and electrode. Therefore, the distribution of the MU fibers within the MU territory can be extracted through the spatio-temporal analysis of this signal [30].

For the purposes of this thesis, after a brief description of the EMG signal generation, more details about the use of surface EMG with multiple electrodes arrangement (high-density surface electromyography, HDsEMG) are presented. The last paragraph of this section reports a description of the decomposition of the EMG signal in its continuent elements (single MUAP) using specific signal procesing of HDsEMG data.

EMG signal generation

The EMG signal is generated by the electrical activity of the muscle fibers active during a contraction [31] (Figure 2.5). This signal originates from the depolarizing and repolarizing regions within the muscle fibers (Figure 2.5a). The propagation of the action

potential through the fiber generates an electric potential which can be detected externally: the SFAP. The characteristics of the recorded SFAP, i.e. the amplitude, the duration, and the delay with respect to the firing (i.e. motoneuron excitation) are mainly affected by several factors, such as the distance between the fiber and the point at which the potential is detected, the diameter of the muscle fiber (with larger diameters correlating to greater amplitudes), the length of the fiber, and the muscle fiber conduction velocity (Figure 2.5a) [32]. The summation of the SFAPs of all the muscle fibers of the MU produces the MUAP (Figure 2.5a). The shape of the MUAP is determined by the amplitudes and time delays of its constituent SFAPs, with fibers closer to a specific detection point contributing with higher amplitudes. As already mentioned, the diameters of MU fibers affect the amplitude and time delays of SFAPs. Moreover, the distribution of neuromuscular junctions within the innervation zone (IZ) also affects the time delays of SFAPs (Figure 2.5a). All these factors influence the MUAP shape. Changes in MU fiber diameters or neuromuscular junction positions lead to complex shapes with multiple peaks and phases. During voluntary contractions, the asynchronous activation of a large number of MUs (often

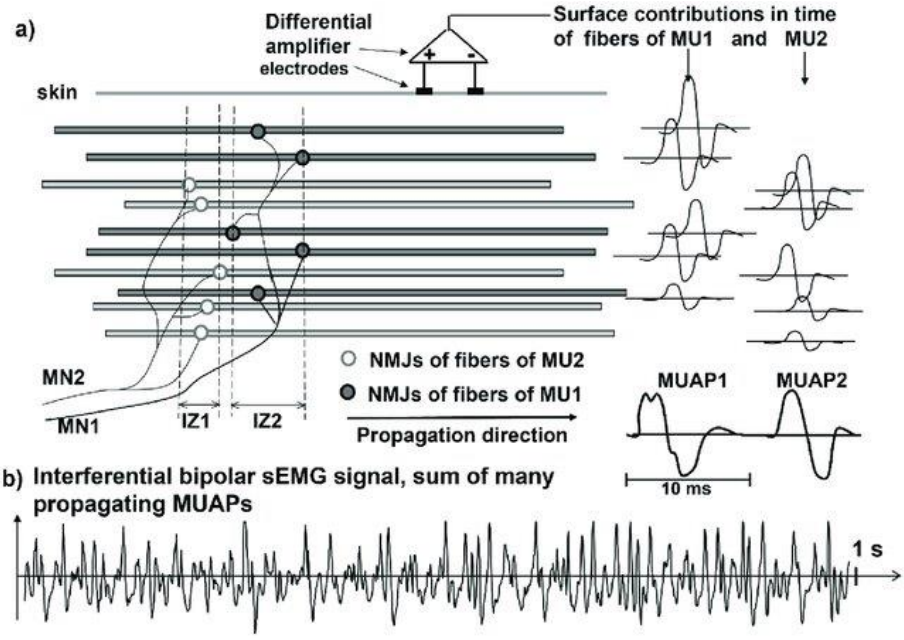

Figure 2.5 Schematic representation of the generation of EMG. (a) The fibers of two motor units (MU1 and MU2) receive input from two motoneurons (MN1 and MN2) in two innervation zones (IZ1 and IZ2 defined by the positions of the neuromuscular junctions, NMJs). The combined skin signals of the propagating action potentials are represented as MUAP1 and MUAP2, which are detected by a differentially amplified (bipolar or single differential detection) signal. It should be noted that the single fiber action potentials (SFAP) of deeper muscle fibers are smaller compared to the contributions of the superficial fibers of each MU. (b) The interferential signal is depicted, which is the summation of the MUAP trains from multiple active motor units. This figure has been taken from *Barbero, M.; Merletti, R.; Rainoldi, A. Atlas of Muscle Innervation Zones*.

ranging from tens to hundreds) generates the interferential EMG signal (Figure 2.5b) [33]

When recording the signal using electrodes (whether they are intramuscular or surface electrodes), the signal sources are physically separated from the electrodes by biological tissues. These tissues act as spatial and temporal low-pass filters, affecting the distribution of the electrical potential [22]. The EMG signal characteristics depend on a number of anatomical, physical, and detection system parameters, such as the thickness of the subcutaneous tissue layer, the depth/distance from the source to the electrodes, the orientation of the muscle fiber with respect to the detection system (mainly for surface recordings), the length of the fibers, the location of the electrode (over the muscle or within the muscle), the spatial filter for signal detection (and the inter-electrode distance), and the shape and size of the electrode [34]–[38].

High-density surface electromyography (HDsEMG)

By combining multiple EMG electrodes placed on the surface of the skin, it is possible to create 1D or 2D arrays of electrodes. This arrangement effectively expands the detection volume of surface electrodes, allowing for a larger area of coverage on the skin plane. The use of high dense arranged multiple electrodes to sample EMG activity (high-density surface electromyography, HDsEMG) from a target region is expected to provide valuable insights into both muscle physiology and anatomy, at the MU level [39], [40]. Over the past two decades, advancements in the processing of HDsEMG, have led to improvements in the understanding of how the central nervous system controls the activation of MU populations during force production [41], [42]. The development of these technologies (for detection and processing) is crucial for the progress of our fundamental comprehension of movement neurophysiology and the advancement of human-machine interaction systems [43], [44].

HDsEMG signal decomposition

Generally speaking, motor unit decomposition aims to separate and identify the activity of individual MUs from the recorded compound EMG signal (Figure 2.6) [45], [46], providing valuable insights into the motor control and coordination of muscles [47], [48]. The decomposition of HDsEMG signals aims to identify the spiking activity of motor neurons in the spinal cord by decoding the electrical activity that they produce in the innervated skeletal muscles [45], [49]. Using spike-triggered averaging [50], [51] is then possible to reconstruct how the individual MUAPs appear on the skin surface [37]. The single MUAPs hold valuable information about muscle anatomy, such as fiber length, innervation zone placement, and conduction velocity [25], [52]–[59]. On the other hand, the patterns of MUAP discharges provide insights into the control strategies employed by the central nervous system [48], [60]–[64].

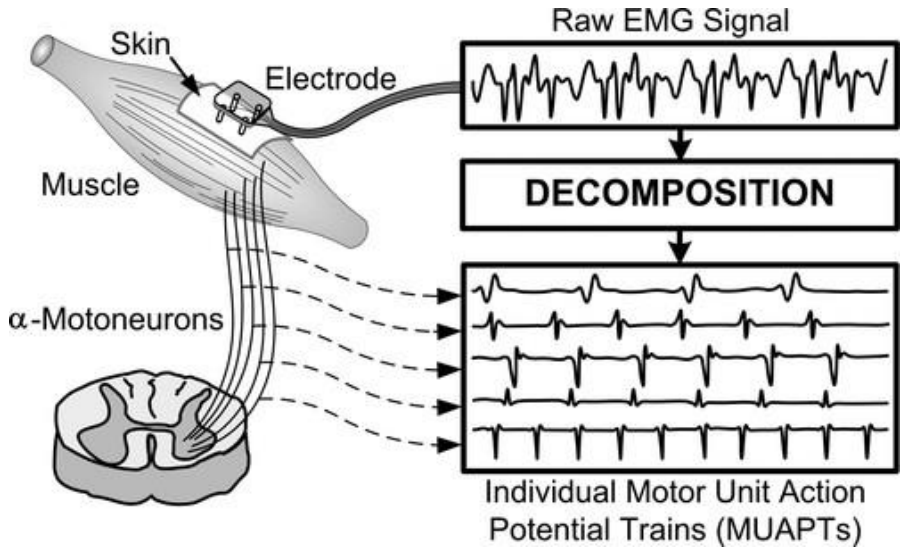

Figure 2.6 MU decomposition. Outline of the decomposition of the surface EMG signal into its constituent motor unit action potentials. Taken from *De Luca et al. 2006*.

Several automatic decomposition algorithms were developed in the last twenty years [65]–[70]. Most of the algorithms are based on the model of the sEMG mixing process that can be inverted with mathematical approaches, such as principal component analysis (PCA) [71], instantaneous independent component analysis (i-ICA) [72], nonnegative matrix factorization (NMF) [73], and convolutive blind source separation (BSS) [65], [67], [74]. The general aim of the algorithms is to find a set of separation vectors which, multiplied by a multichannel sEMG observation vector, provides a number of sEMG components [43]. PCA, i-ICA, and NMF rely on assumptions that are not fully satisfied by MU activities. Convolutive BSS method is considered to be more robust since it is based on the sparsity of MU spike trains. The accuracy and performance of BSS-based algorithm were evaluated under several experimental conditions [75]–[77].

The advancements in multichannel surface sEMG recordings and decomposition techniques have introduced new possibilities in clinical diagnosis and monitoring. For instance, the aforementioned technology can be used to monitor the recruitment and the firing rates of MUs. These mechanisms, that are well known in voluntary contractions of healthy muscles (as explained in section 2.2.4), may be affected in different ways in pathological conditions (e.g. essential tremors, stroke, cerebral palsy, Parkinson disease) [78]–[80].

2.3.2 Mechanomyography

Another valuable tool for assessing the contractile properties of the muscle is mechanomyography (MMG), which measures the mechanical vibrations generated by

contracting muscle fibers [81], [82]. Since the muscle works as a near-constant volume system, the muscle fibers are shortening and concurrently linked to a radial displacement (transversely) [82]. The expansion of the fiber produces a pressure wave that propagates to the skin, and it can be measured through accelerometer, displacement sensor, piezoelectric sensor, microphone, and laser device [83]. MMG can provide information about the force and timing of muscle contractions at the global level, and single MU level [84]–[88].

2.3.3 Magnetic resonance imaging

Magnetic resonance imaging (MRI) was recently applied for the investigation of the neuromuscular system [89], [90]. MRI is a medical imaging method that employs magnetic fields, magnetic field gradients, and radio waves to obtain a visualization and tissues of the body [91]. Through brief bursts of radio waves, the magnetic properties of atoms within the body can be manipulated, aligning the spins of protons in the same direction. Subsequently, when the magnetic vector returns to its original state, radio frequency waves are emitted and they can be detected. These signals are elaborated to produce detailed images. By adjusting the parameters of an MRI sequence, diverse contrasts can be generated based on the distinct relaxation properties of various tissues.

While conventional MRI primarily offers structural information, diffusion-weighted MRI (DW-MRI) is capable of providing functional insights [92]. DW-MRI enables the assessment of molecular movement measuring the diffusion of water molecules within a voxel of tissue. Recent advancements in DW-MRI have demonstrated its potential to visualize electro-stimulated contractions of individual MUs in both healthy conditions [93] and pathological states [94], [95]. Moreover, this technique has been employed to investigate the muscle twitch profile [96].

2.3.4 Ultrasonography

Ultrasonography (US) has recently gained popularity as a non-invasive method to assess muscle structure, size, and contractile properties in real-time. Ultrasound imaging is often applied to study muscle properties [97] from both an anatomical (e.g., tissue architecture and texture [98]–[102]) and functional (e.g., muscle contraction patterns, tissue elasticity, and muscle anisotropy [103]–[107]) perspective.

The conventional US technique relies on the properties of different acoustic impendances of the biological tissues. Ultrasonic waves are sent by a probe into the tissue and reflections of the waves (i.e. echoes) are then received. The delays and the intensities of the reflections depend respectively on the distance between the probe and tissue and on its acoustic impedances [100]. This procedure occurs sequentially using focused beams (ultrasonic waves). In the standard B-mode imaging the echoes are transformed into pixels of different position and brightness depending on their delays and intensities. Each focused beam allows the reconstruction of one image line, and an image usually consists of a few

tens of lines (64 to 512). When sequences of images are acquired in this modality (i.e. B-mode) the frame rate is constrained by the number of lines and the time required to transmit a beam, as well as to receive and process backscattered echoes.

One of the most common applications of conventional ultrasound is the study of muscle architecture [108]–[115] through the analysis of B-mode images. Furthermore, acquiring videos of the muscle during contraction is also of interest for muscle architecture tracking. The movement of muscle fibers can be investigated by manually or automatically [116]–[120] detecting and tracking the fascicles (i.e., bundles of fibers surrounded by high echogenic connective tissue) during contraction. For example, as shown in Figure 2.7, we analyzed B-mode US sequences to investigate the dynamics of the muscle fibers in the superficial and deep compartments of the tibialis anterior during electrical stimulation directly over the muscle or stimulation of the nerve [121].

Over the years, other techniques have been developed from ultrasonography, providing new insights and perspectives on muscle characteristics such as muscle contraction patterns, tissue elasticity, and muscle anisotropy [103]–[107]. One of the first

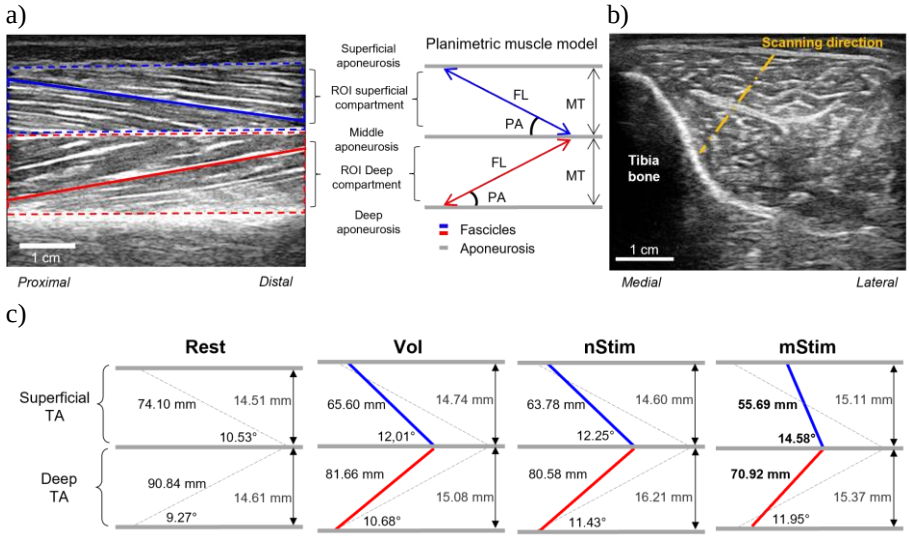

Figure 2.7 Example of conventional US imaging for studying MU recruitment. Upper panel: (a) US longitudinal scan of TA. All the aponeuroses are clearly visible and consequently the two compartments (superficial in blue and deep in red). For each muscle compartment one fascicle (solid line) and the region of interest (dashed lines) are highlighted. Planimetric muscle model of the longitudinal US image reporting all the morphometric variables considered. FL = fascicle length; PA = pennation angle; MT = muscle thickness. (b) Trasversal US image of TA to visually inspect the scanning direction (yellow dash-dotted line) and achieve good quality of the longitudinal image. It is possible to notice the deep and central aponeurosis and the tibia bone. Lower panel: (c) Architectural changes induced by Vol, nStim and mStim contractions of TA at 25% MVC in one representative subject. Pennation Angle (PA), Fascicle Length (FL) and Muscle Thickness (MT) are represented on a planimetric model of the superficial and deep TA compartments. Blue and red lines represent muscle fascicles. The inclination of the representing muscle fascicles was emphasized for representation purposes.

applications in this field is known as elastography [122]–[124], which involves the quantitative imaging of strain and elastic modulus of muscle tissue. This noninvasive assessment of the mechanical properties of muscles has evolved from quasi-static elastography [122] to dynamic shear wave elastography [125], [126] and transient elastography [127], [128], necessitating more sophisticated ultrasound equipment. In particular, shear wave imaging requires real-time imaging of the propagation of shear mechanical waves in the tissue, which reflects tissue viscoelasticity properties. The minimum frame rate required to accurately sample these waves is about a few thousands Hertz. The requirements for high spatial and temporal sampling rates have been achieved with a novel powerful imaging technique known as ultrafast ultrasound imaging [128]–[130].

Ultrafast ultrasound and tissue velocity imaging

Ultrafast US (UUS) imaging significantly increases the frame rate by transmitting plane waves and using parallel reception of the backscattered echoes from the tissue. The ultrafast architecture functions as a fully parallelized platform, transmitting unfocused waves and recording the resulting backscattered echoes by storing the raw radiofrequency (RF) signals. The image is then reconstructed using beamforming techniques in post-processing [129]. This imaging technique can achieve frame rates of up to 10,000 Hz, as the only constraint is determined by the time it takes for a single pulse (plane wave) to propagate in the tissue and for the echoes to return to the transducer.

The beamformed plane-wave images have lower spatial resolution compared to conventional ultrasound, but several approaches can be adopted to enhance image quality. For example, compounding multiple tilted plane waves [131] can improve resolution or reduce speckle, and new beamforming processing techniques [132] can also be employed.

The high frame rate acquisition opens up new possibilities for analyzing functional information. This includes shear wave imaging, as previously mentioned, which allows for the evaluation of shear wave propagation and real-time quantitative measurements of muscle elasticity [103], [105], [106], [126], [133], [133]–[135]. Additionally, ultrafast ultrasound imaging can be used for precise detection of contraction onset [104], [136]–[138]. In the case of electrical stimulation-induced muscle fascicle and tendon motion, the very high frame rate ultrasound (4 kHz) can be used to determine the onset of these movements [139].

Ultrafast ultrasound imaging approach enables the evaluation of transient mechanical behaviour of the entire muscle with millimetric precision [138], [140], [141]. Tissue displacements can generally be estimated from the time delays between echo signals, and a phase shift between consecutive RF signals of image lines occurs when they are reflected against a moving object (known as the “Doppler effect”) [142]. By measuring this phase shift, the axial velocity can be estimated based on a comprehensive evaluation of the Doppler equation using a two-dimensional autocorrelation approach [142]. This method

allows for the measurement of relative displacements between two consecutive frames at the micron scale, providing an estimation of tissue local velocity. This technique, also known as tissue velocity imaging, has been applied in skeletal muscle to characterize the patterns of contraction. Deffieux and colleagues used ultrafast ultrasound tissue velocity imaging to investigate the behavior of contracting tissues in the biceps brachii muscle during electrical stimulation [143], [144]. They employed a high frame rate of 2500 fps to capture real-time muscle contraction during transient electro-stimulation, imaging the muscle's cross-sectional plane perpendicular to the fibers (Figure 2.8a). Velocity measurements of the tissue were obtained using radio frequency-based speckle tracking techniques (Figure 2.8b). The profiles of these velocities were analyzed (Figure 2.8c) in relation to various electrostimulation intensities and pulse repetition frequencies, involving different volunteers. In addition to temporal information, spatial information was also obtained by measuring the tissue velocity field within the contracting sources. For example, the spatial extension of the contracting fiber bundle (contracting area), consisting of the true contracting bundle and the passive surrounding elastic tissue, could be determined at increasing stimulation intensities (Figure 2.8d).

Studying the muscle tissue velocity during voluntary contractions is not straightforward due to the complexity of muscle activation processes. Multiple MUs are concurrently active during voluntary contractions, with overlapping territories and intricate firing patterns coordinated by the nervous system. Recently, new methods have been developed to identify the mechanical responses of individual MUs in ultrasound image sequences [145], [146]. The 2-D cross-sectional velocity image sequence theoretically captures the thickening of fibers perpendicular to the image plane during the contraction phase. By using a spatio-temporal decomposition, it is possible to separate components with different spatio-temporal characteristics, which can be attributed to MU mechanical responses or noise [145], [147]. The core of the separation algorithm is the spatio-temporal independent component analysis (stICA), which considers the signals as linear combinations of sources [148].

Promising results in the decomposition of MUs mechanical responses were obtained by Rohlén et al. in the biceps brachii muscle at low force levels, revealing similarities in terms of the number of units, territory sizes, and firing rates compared to the existing literature on MUs described by EMG [145]. The authors validated their decomposition method by comparing it to the gold standard needle electromyography [147], although they found a relatively low number of highly reliable mechanical responses associated with MUs in EMG. It is worth noting that the non-linear nature of the measured system (muscle tissue), resulting from the heterogeneous mix of linear and non-linear elastic constituents [149], could have influenced the method's performance, as well as the mechanical coupling introduced by inserting the needle into the muscle [147]. However, under controlled conditions (stable, isometric, weak force contraction), the oscillatory physiological

mechanical responses of individual MUs were successfully detected and separated from the global signals.

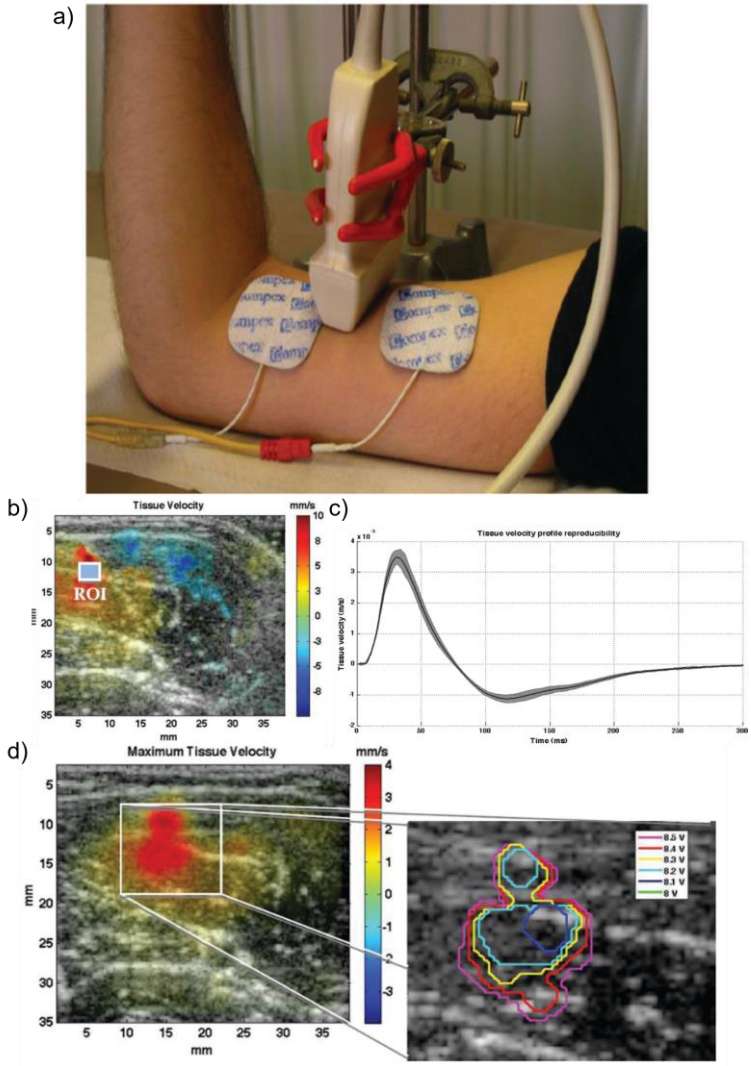

Figure 2.8 Example of tissue velocity imaging in electrically-elicited contractions. (a) Experimental setup adopted by Deffieux et al. for an acquisition. The imaging probe is positioned perpendicular to the muscle fibers. (b) Tissue velocity field in a transverse image of the biceps brachii 14 ms after an 9 V (11 mA) electrostimulation. an approximately 3 × 3 mm2 region of interest (ROI) is defined around the maximum to track the tissue velocity profile. (c) Tissue velocity profile: mean of the 30 acquisitions with its standard deviation envelope. (d) Map (left) of the maximum of the tissue velocity field (8.3 V stimulation) and spatial extension (right) of the contraction as visualized by an isocontour on the velocity tissue field. All the parts of this figure are extracted from Deffiuex et al.

In general, these studies have demonstrated the potential of a novel neuromuscular functional imaging approach that can provide new possibilities for investigating various aspects of muscle physiology (also at the MU level) that were previously challenging or inaccessible to study.

2.3.5 Combination of techniques

Various methods and technologies have been developed to assess muscle excitation and contraction, each offering unique insights into different aspects of muscle function. Advancements in technology have led to the development of sophisticated equipment and analysis techniques to enhance the accuracy and precision of muscle excitation and contraction assessments. Overall, the methods and technologies employed to assess muscle excitation and contraction can be combined for unravelling the complexities of human movement control. In fact, all the aforementioned techniques, individually, provide partial descriptions of the complex phenomena of the muscle contraction and force production. The anatomical, physical, electrical, and mechanical properties of the generation of the muscle force (and MU force) can be detected and interpretated separately with these methods and technologies. It is straightforward that the combination of two or more of these techniques enables the muscle and MU characterization of different aspects of the same phenomenon. Therefore, a MU can be investigated anatomically, electrically, and mechanically with applications for analysis of the modifications of MU properties following, for instance, fatigue or pathological conditions.

In this regard, a striking example is provided by the study of Cescon et al. [86] in which a method for non-invasive assessment of single MU properties is proposed. This method combined EMG, MMG (Figure 2.9, top panel taken from [150]), and force signals providing the analysis of electromechanical properties of single MUs. The mechanical twitch responses in the MMG and the force signal were obtained by averaging the signals using the time points of occurrence of single MUAPs as triggers (Figure 8, bottom panel taken from [86]). These occurrences were obtained from the decomposition of the array EMG signals.

Combination of electromyography and ultrasonography

By combining EMG and ultrasound techniques, it becomes possible to obtain a more comprehensive and detailed description of the events underlying muscle force generation. In fact, the US-EMG combination would enable simultaneous assessment of the muscle activation and mechanical tissue displacement. For instance, we conducted a study where B-mode ultrasound imaging and multichannel EMG with an array of 32 electrodes on the calf muscles were used to enhance the detection sensitivity of muscle fasciculations (Figure 2.10) [151], [152]. Fasciculations are spontaneous activations of motoneurons often associated with neurological disorders such as amyotrophic lateral sclerosis and motor

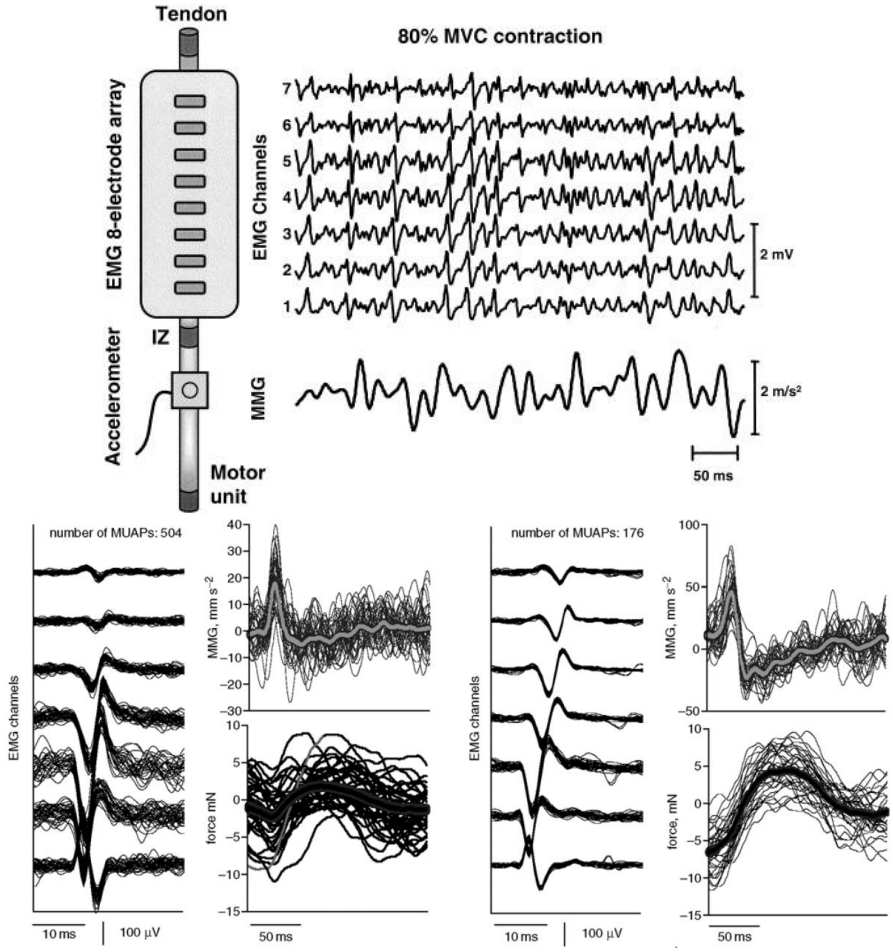

Figure 2.9 Simultaneous recording of EMG and MMG signals. Top panel: on the left side, a schematic diagram indicating the location of the electrode array and accelerometer. The electrode array is oriented parallel to the muscle fibers and positioned distally from the innervation zone, while the accelerometer is located proximally. The term "IZ" represents the innervation zone. Bottom panel: examples of single MU MMG and force signals for two representative contractions. The MMG and force responses were obtained by averaging signals using the time points of occurrence of single MU action potentials as triggers. It is important to note the distinct MMG and force twitch responses between the two muscles.

neuron disease [153], [154]. Fasciculation potentials (FP) [154] were identified using single differential EMGs with inter-electrode distances (IEDs) of 10 mm (SD1), 20 mm (SD2), and 30 mm (SD3), while fasciculation events (FE) [155], [156] were detected from sequences of US images. These findings showed that both techniques exhibited comparable sensitivities to muscle fasciculations [157]. However, the agreement between the two techniques in terms of unique detections (FE = FP) was relatively low, which was attributed to the diverse spatial sensitivities of EMG and ultrasound. These results suggest that

combining EMG and ultrasound techniques can maximize the sensitivity to muscle fasciculations, and more in general to detect single MU activity. Other studies have also employed combined EMG and ultrasound analysis to investigate muscle dynamics and characterize electromechanical delays [139].

Recent technological advancements in both EMG and ultrasound have further enhanced the value of the combined EMG-US approach, extending its applicability to the single motor unit (MU) level. The combination of new computational analysis of high frame rate US images with EMG enables the electromechanical imaging of the neural output. Rohlèn et al. combined ultrafast ultrasound with needle electromyography to validate their method for identifying mechanical responses of MUs [147].

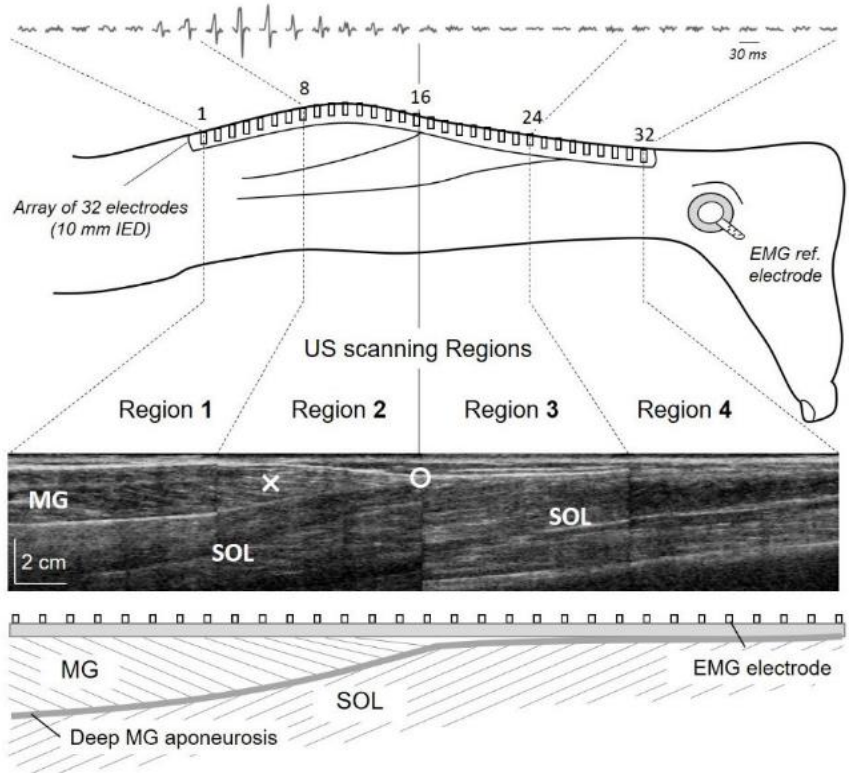

Figure 2.10 Fasciculation investigation with combine EMG and US analysis. Electrode positioning over the posterior leg. Ultrasound (US) videos (80 fps) were detected simultaneously with EMGs from four adjacent regions along the electrode array composed by two linear arrays of 16 electrodes with 10 mm inter-electrode distance (IED). Lower panels: composite image of four longitudinal US scans and schematic representation of calf muscles' architecture. The white circle in the US image indicates the gastrocnemius myo-tendon junction. An example of fasciculation potential detected in single differential configuration (10 mm IED) is reported in the upper part of the figure. The location of the corresponding fasciculation event identified in US images is indicated with a white cross. MG: medial gastrocnemius; SOL: soleus. Figure extracted from Botter et al. 2021.

One important aspect of the integration of HDsEMG and ultrasound imaging is related to the technologies enabling this simultaneous acquisition. Typically, surface electrodes and US probes are placed in close proximity to each other. Whether this is a problem, it may be related to a number of factors. For instance, for small muscles (e.g. hand or forearm muscles) this arrangment is not possible while for larger muscles there might be sufficient space to sample EMG and ultrasound from different portions of the muscle. Moreover, many muscles showed to have different regional patterns of activation and distinct regional variation of fascicle architecture [56]. For these reasons, a grid transparent to US (Figure 2.11A) has been proposed enabling simultaneous regional analysis of the muscle excitation and the resulting tissue displacement [159]. With this technology, the relationship between modulations motor unit (MU) discharge, fascicle length, and dorsiflexion torque was assessed in tibialis anterior muscle (Figure 2.11B) [160].

Overall, the state of the art described in this section suggests that the combined use of the electromyography and ultrasonography has the potential to provide a detailed neuromechanical characterization of motor units, from neural excitation to muscle tissue strain. Currently, the feasibility of this integration, as well as the systematic evaluation of its limitations and advantages, are not described in the literature. This type of assessment is necessary to guide future developments both in experimental signal acquisition and data processing, as well as to identify clinical applications that could benefit from this integration. In this context, this thesis describes and tests a novel approach aimed at providing a comprehensive description of individual motor units based on the combination of high-density electromyography and ultrafast ultrasonography.

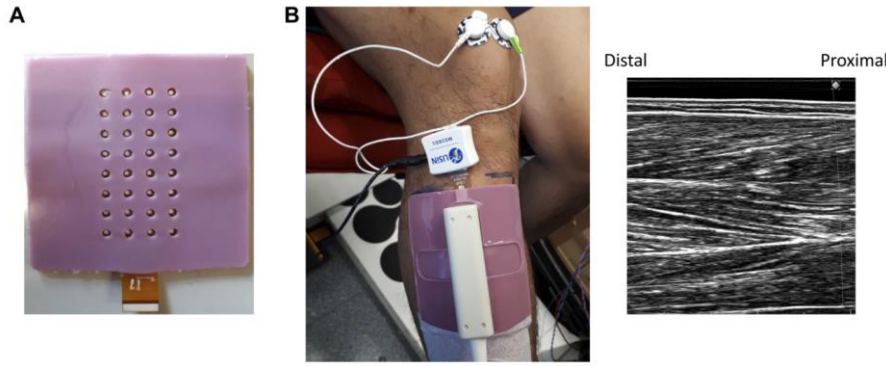

Figure 2.11 High-density surface electromyography (HDsEMG) ultrasound-transparent electrodes. A) 8 x 4, 32-channel (10-mm interelectrode distance) electrode grid. B) HDsEMG electrode grid with 32-channel HDsEMG amplifier (connected on top of the electrode) and flat ultrasound probe can be seen on the left. Ultrasound image of proximal tibialis anterior muscle can be seen on the right. Note the quality of the image with accurate visualization of fascicles and, superficial, intermediate, and deep aponeuroses (n =1, male participant). Figure extracted from Botter et al. 2013.

2.4 References

[1] R. M. Enoka, *Neuromechanics of Human Movement*. Human Kinetics, 2002.

[2] A. J. McComas, B. R. MacIntosh, and P. F. Gardiner, *Skeletal Muscle: Form and Function*. Human Kinetics, 2006.

[3] R. E. Burke, 'Motor Units: Anatomy, Physiology, and Functional Organization', in *Comprehensive Physiology*, John Wiley & Sons, Ltd, 2011, pp. 345–422. doi: 10.1002/cphy.cp010210.

[4] R. M. Enoka and A. J. Fuglevand, 'Motor unit physiology: some unresolved issues', *Muscle Nerve*, vol. 24, no. 1, pp. 4–17, Jan. 2001, doi: 10.1002/1097-4598(200101)24:1<4::aid-mus13>3.0.co;2-f.

[5] A. L. Hodgkin and A. F. Huxley, 'A quantitative description of membrane current and its application to conduction and excitation in nerve', *J. Physiol.*, vol. 117, no. 4, pp. 500–544, Aug. 1952.

[6] A. F. Huxley, 'The origin of force in skeletal muscle', *Ciba Found. Symp.*, no. 31, pp. 271–290, 1975, doi: 10.1002/9780470720134.ch15.

[7] S. Bodine-Fowler, A. Garfinkel, R. R. Roy, and V. R. Edgerton, 'Spatial distribution of muscle fibers within the territory of a motor unit', *Muscle Nerve*, vol. 13, no. 12, pp. 1133–1145, 1990, doi: 10.1002/mus.880131208.

[8] A. J. Fuglevand, 'Mechanical properties and neural control of human hand motor units', *J. Physiol.*, vol. 589, no. Pt 23, pp. 5595–5602, Dec. 2011, doi: 10.1113/jphysiol.2011.215236.

[9] F. Buchthal, F. Erminio, and P. Rosenfalck, 'Motor Unit Territory in Different Human Muscles', *Acta Physiol. Scand.*, vol. 45, no. 1, pp. 72–87, 1959, doi: 10.1111/j.1748-1716.1959.tb01678.x.

[10] I. Gath and E. Stålberg, 'On the measurement of fibre density in human muscles', *Electroencephalogr. Clin. Neurophysiol.*, vol. 54, no. 6, pp. 699–706, Dec. 1982, doi: 10.1016/0013-4694(82)90124-9.

[11] R. G. Willison, 'Arrangement of muscle fibers of a single motor unit in mammalian muscles', *Muscle Nerve*, vol. 3, no. 4, pp. 360–361, 1980, doi: 10.1002/mus.880030414.

[12] A. Miller-Larsson, 'A model of spatial distribution of muscle fibres of a motor unit in normal human limb muscles', *Electromyogr. Clin. Neurophysiol.*, vol. 20, no. 4–5, pp. 281–298, 1980.

[13] J. Navallas, A. Malanda, L. Gila, J. Rodríguez, and I. Rodríguez, 'A muscle architecture model offering control over motor unit fiber density distributions', *Med. Biol. Eng. Comput.*, vol. 48, no. 9, pp. 875–886, Sep. 2010, doi: 10.1007/s11517-010-0642-x.

[14] A. F. Huxley, 'Muscle structure and theories of contraction.', *Prog. Biophys. Biophys. Chem.*, vol. 7, pp. 255–318, 1957.

[15] A. J. Fuglevand, D. A. Winter, and A. E. Patla, 'Models of recruitment and rate coding organization in motor-unit pools', *J. Neurophysiol.*, vol. 70, no. 6, pp. 2470–2488, 1993, doi: 10.1152/jn.1993.70.6.2470.

[16] A. J. Fuglevand, V. G. Macefield, and B. Bigland-Ritchie, 'Force-frequency and fatigue properties of motor units in muscles that control digits of the human hand',

J. Neurophysiol., vol. 81, no. 4, pp. 1718–1729, Apr. 1999, doi: 10.1152/jn.1999.81.4.1718.

[17] G. W. Sypert and J. B. Munson, 'Basis of segmental motor control: motoneuron size or motor unit type?', *Neurosurgery*, vol. 8, no. 5, pp. 608–621, May 1981, doi: 10.1227/00006123-198105000-00020.

[18] R. Bottinelli and C. Reggiani, 'Human skeletal muscle fibres: molecular and functional diversity', *Prog. Biophys. Mol. Biol.*, vol. 73, no. 2–4, pp. 195–262, 2000, doi: 10.1016/s0079-6107(00)00006-7.

[19] M. E. Esbjörnsson, M. S. Dahlström, J. W. Gierup, and E. Ch. Jansson, 'Muscle fiber size in healthy children and adults in relation to sex and fiber types', *Muscle Nerve*, vol. 63, no. 4, pp. 586–592, Apr. 2021, doi: 10.1002/mus.27151.

[20] C. J. Heckman and R. M. Enoka, 'Physiology of the motor neuron and the motor unit', in *Handbook of Clinical Neurophysiology*, A. Eisen, Ed., in Clinical Neurophysiology of Motor Neuron Diseases, vol. 4. Elsevier, 2004, pp. 119–147. doi: 10.1016/S1567-4231(04)04006-7.

[21] E. Henneman, 'Relation between size of neurons and their susceptibility to discharge', *Science*, vol. 126, no. 3287, pp. 1345–1347, 1957, doi: 10.1126/science.126.3287.1345.

[22] J. V. Basmajian and C. J. de Luca, *Muscles Alive: Their Functions Revealed by Electromyography*. Baltimore; London; Sydney: Williams & Wilkins, 1985. doi: 10.1249/00005768-197621000-00002.

[23] R. Merletti, A. Botter, and U. Barone, 'Detection and Conditioning of Surface EMG Signals', in *Surface Electromyography : Physiology, Engineering, and Applications*, John Wiley & Sons, Ltd, 2016, pp. 1–37. doi: 10.1002/9781119082934.ch03.

[24] R. Merletti and D. Farina, 'Analysis of intramuscular electromyogram signals', *Philos. Trans. R. Soc. Math. Phys. Eng. Sci.*, Nov. 2008, doi: 10.1098/rsta.2008.0235.

[25] F. Buchthal, C. Guld, and P. Rosenfalck, 'Multielectrode Study of the Territory of a Motor Unit', *Acta Physiol. Scand.*, vol. 39, no. 1, pp. 83–104, 1957, doi: 10.1111/j.1748-1716.1957.tb01411.x.

[26] C. J. De Luca and A. Adam, 'Decomposition and Analysis of Intramuscular Electromyographic Signals', in *Modern Techniques in Neuroscience Research*, U. Windhorst and H. Johansson, Eds., Berlin, Heidelberg: Springer Berlin Heidelberg, 1999, pp. 757–776. doi: 10.1007/978-3-642-58552-4_27.

[27] E. Stålberg and P. Dioszeghy, 'Scanning EMG in normal muscle and in neuromuscular disorders', *Electroencephalogr. Clin. Neurophysiol.*, vol. 81, no. 6, pp. 403–416, Dec. 1991, doi: 10.1016/0013-4694(91)90001-k.

[28] T. H. J. M. Gootzen, D. J. M. Vingerhoets, and D. F. Stegeman, 'A study of motor unit structure by means of scanning EMG', *Muscle Nerve*, vol. 15, no. 3, pp. 349–357, 1992, doi: 10.1002/mus.880150314.

[29] Í. Corera, A. Malanda, J. Rodriguez-Falces, S. Porta, and J. Navallas, 'Motor unit profile: A new way to describe the scanning-EMG potential', *Biomed. Signal Process. Control*, vol. 34, pp. 64–73, Apr. 2017, doi: 10.1016/j.bspc.2016.12.020.

[30] J. Navallas and E. Stålberg, 'Studying motor end-plate topography by means of scanning-electromyography', *Clin. Neurophysiol.*, vol. 120, no. 7, pp. 1335–1341, Jul. 2009, doi: 10.1016/j.clinph.2009.05.014.

[31] D. Farina, D. F. Stegeman, and R. Merletti, 'Biophysics of the Generation of EMG Signals', in *Surface Electromyography : Physiology, Engineering, and Applications*, John Wiley & Sons, Ltd, 2016, pp. 1–24. doi: 10.1002/9781119082934.ch02.

[32] S. D. Nandedkar and E. Stålberg, 'Simulation of single muscle fibre action potentials', *Med. Biol. Eng. Comput.*, vol. 21, no. 2, pp. 158–165, Mar. 1983, doi: 10.1007/BF02441531.

[33] M. Barbero, R. Merletti, and A. Rainoldi, 'Generation, Propagation, and Extinction of Single-Fiber and Motor Unit Action Potentials', in *Atlas of Muscle Innervation Zones: Understanding Surface Electromyography and Its Applications*, M. Barbero, R. Merletti, and A. Rainoldi, Eds., Milano: Springer Milan, 2012, pp. 21–38. doi: 10.1007/978-88-470-2463-2_3.

[34] N. A. Dimitrova, G. V. Dimitrov, and V. N. Chikhman, 'Effect of electrode dimensions on motor unit potentials', *Med. Eng. Phys.*, vol. 21, no. 6–7, pp. 479–485, 1999, doi: 10.1016/s1350-4533(99)00069-7.

[35] D. Farina, C. Cescon, and R. Merletti, 'Influence of anatomical, physical, and detection-system parameters on surface EMG', *Biol. Cybern.*, vol. 86, no. 6, pp. 445–456, Jun. 2002, doi: 10.1007/s00422-002-0309-2.

[36] D. Farina and R. Merletti, 'Effect of electrode shape on spectral features of surface detected motor unit action potentials', *Acta Physiol. Pharmacol. Bulg.*, vol. 26, no. 1–2, pp. 63–66, 2001.

[37] K. Roeleveld, D. F. Stegeman, H. M. Vingerhoets, and A. Van Oosterom, 'The motor unit potential distribution over the skin surface and its use in estimating the motor unit location', *Acta Physiol Scand*, vol. 161, pp. 465–472, 1997.

[38] D. F. Stegeman, D. Dumitru, J. C. King, and K. Roeleveld, 'Near- and far-fields: Source characteristics and the conducting medium in neurophysiology', *J. Clin. Neurophysiol.*, vol. 14, no. 5, 1997, doi: 10.1097/00004691-199709000-00009.

[39] J. H. Blok, J. P. van Dijk, G. Drost, M. J. Zwarts, and D. F. Stegeman, 'A high-density multichannel surface electromyography system for the characterization of single motor units', *Rev. Sci. Instrum.*, vol. 73, no. 4, pp. 1887–1897, Mar. 2002, doi: 10.1063/1.1455134.

[40] S. Dick F., K. Bert U., L. Bernd G., and V. D. Johannes P., 'High-density Surface EMG: Techniques and Applications at a Motor Unit Level', *Biocybern. Biomed. Eng.*, vol. 32, no. 3, pp. 3–27, Jan. 2012, doi: 10.1016/S0208-5216(12)70039-6.

[41] R. Merletti, M. Aventaggiato, A. Botter, A. Holobar, H. Marateb, and T. M. M. Vieira, 'Advances in surface EMG: Recent progress in detection and processing techniques', *Crit. Rev. Biomed. Eng.*, vol. 38, no. 4, pp. 305–45, 2010, doi: 10.1615/CritRevBiomedEng.v38.i4.10.

[42] R. Merletti, A. Holobar, and D. Farina, 'Analysis of motor units with high-density surface electromyography', *J. Electromyogr. Kinesiol.*, vol. 18, no. 6, pp. 879–890, 2008, doi: 10.1016/j.jelekin.2008.09.002.

[43] A. Holobar and D. Farina, 'Noninvasive Neural Interfacing With Wearable Muscle Sensors: Combining Convolutive Blind Source Separation Methods and Deep

Learning Techniques for Neural Decoding', *IEEE Signal Process. Mag.*, vol. 38, no. 4, pp. 103–118, Jul. 2021, doi: 10.1109/MSP.2021.3057051.

[44] D. Farina and A. Holobar, 'Human?Machine Interfacing by Decoding the Surface Electromyogram [Life Sciences]', *IEEE Signal Process. Mag.*, vol. 32, no. 1, pp. 115–120, Jan. 2015, doi: 10.1109/MSP.2014.2359242.

[45] B. Mambrito and C. J. De Luca, 'Acquisition and Decomposition of the EMG Signal'.

[46] C. J. De Luca, A. Adam, R. Wotiz, L. D. Gilmore, and S. H. Nawab, 'Decomposition of Surface EMG Signals', *J. Neurophysiol.*, vol. 96, no. 3, pp. 1646–1657, Sep. 2006, doi: 10.1152/jn.00009.2006.

[47] C. J. De Luca and Z. Erim, 'Common drive of motor units in regulation of muscle force', *Trends Neurosci.*, vol. 17, no. 7, pp. 299–305, Jan. 1994, doi: 10.1016/0166-2236(94)90064-7.

[48] P. Contessa and C. J. D. Luca, 'Neural control of muscle force: indications from a simulation model', *J. Neurophysiol.*, vol. 109, no. 6, pp. 1548–1570, Mar. 2013, doi: 10.1152/jn.00237.2012.

[49] A. HOLOBAR, D. FARINA, M. GAZZONI, R. MERLETTI, and D. ZAZULA, 'Estimating motor unit discharge patterns from high-density surface electromyogram.', *Clin. Neurophysiol.*, vol. 120, pp. 551–562, 2009.

[50] 'Reliability of spike triggered averaging of the surface electromyogram for motor unit action potential estimation - Hu - 2013 - Muscle & Nerve - Wiley Online Library'. https://onlinelibrary.wiley.com/doi/10.1002/mus.23819 (accessed May 21, 2023).

[51] X. Hu, W. Z. Rymer, and N. L. Suresh, 'Motor unit pool organization examined via spike-triggered averaging of the surface electromyogram', *J. Neurophysiol.*, vol. 110, no. 5, pp. 1205–1220, Sep. 2013, doi: 10.1152/jn.00301.2012.

[52] 'Effects of muscle fiber type and size on EMG median frequency and conduction velocity | Journal of Applied Physiology'. https://journals.physiology.org/doi/abs/10.1152/jappl.1995.79.1.23?rfr_dat=cr_pub++0pubmed&url_ver=Z39.88-2003&rfr_id=ori%3Arid%3Acrossref.org (accessed May 21, 2023).

[53] A. Gallina and A. Botter, 'Spatial localization of electromyographic amplitude distributions associated to the activation of dorsal forearm muscles', *Front. Physiol.*, vol. 4, 2013, doi: 10.3389/fphys.2013.00367.

[54] A. Gallina and T. Vieira, 'Territory and fiber orientation of vastus medialis motor units: A Surface electromyography investigation', *Muscle Nerve*, vol. 52, no. 6, pp. 1057–1065, 2015, doi: 10.1002/mus.24662.

[55] R. Merletti, A. Botter, C. Cescon, M. A. Minetto, and T. M. M. Vieira, 'Advances in surface EMG: Recent progress in clinical research applications', *Crit. Rev. Biomed. Eng.*, vol. 38, no. 4, 2010, doi: 10.1615/CritRevBiomedEng.v38.i4.20.

[56] T. M. Vieira and A. Botter, 'The Accurate Assessment of Muscle Excitation Requires the Detection of Multiple Surface Electromyograms', *Exerc. Sport Sci. Rev.*, vol. 49, no. 1, 2021, doi: 10.1249/JES.0000000000000240.

[57] R. M. Enoka and D. Farina, 'Force Steadiness: From Motor Units to Voluntary Actions', *Physiology*, vol. 36, no. 2, pp. 114–130, Mar. 2021, doi: 10.1152/physiol.00027.2020.

[58] K. Roeleveld and D. F. Stegeman, 'WHAT DO WE LEARN FROM MOTOR UNIT ACTION POTENTIALS IN SURFACE ELECTROMYOGRAPHY?', *Muscle Nerve. Suppl.*, vol. 11, pp. 92–97, 2002, doi: 10.1002/mus.10153.

[59] D. Farina and R. Merletti, 'Estimation of average muscle fiber conduction velocity from two-dimensional surface EMG recordings', *J. Neurosci. Methods*, vol. 134, no. 2, pp. 199–208, Apr. 2004, doi: 10.1016/j.jneumeth.2003.12.002.

[60] C. J. de Luca, R. S. LeFever, M. P. McCue, and A. P. Xenakis, 'Control scheme governing concurrently active human motor units during voluntary contractions', *J. Physiol.*, vol. 329, no. 1, pp. 129–142, 1982, doi: 10.1113/jphysiol.1982.sp014294.

[61] 'Hierarchical control of motor units in voluntary contractions | Journal of Neurophysiology'. https://journals.physiology.org/doi/full/10.1152/jn.00961.2010 (accessed May 21, 2023).

[62] R. M. Enoka and J. Duchateau, 'Rate coding and the control of muscle force', *Cold Spring Harb. Perspect. Med.*, vol. 7, no. 10, 2017, doi: 10.1101/cshperspect.a029702.

[63] C. J. de Luca, P. J. Foley, and Z. Erim, 'Motor unit control properties in constant-force isometric contractions', *J. Neurophysiol.*, vol. 76, no. 3, pp. 1503–1516, Sep. 1996, doi: 10.1152/jn.1996.76.3.1503.

[64] X. Hu, W. Z. Rymer, and N. L. Suresh, 'Control of motor unit firing during step-like increases in voluntary force', *Front. Hum. Neurosci.*, vol. 8, 2014, Accessed: May 21, 2023. [Online]. Available: https://www.frontiersin.org/articles/10.3389/fnhum.2014.00721

[65] A. Holobar and D. Zazula, 'Multichannel blind source separation using convolution Kernel compensation', *IEEE Trans. Signal Process.*, vol. 55, no. 9, pp. 4487–4496, 2007, doi: 10.1109/TSP.2007.896108.

[66] A. Holobar and D. Zazula, 'Correlation-based decomposition of surface electromyograms at low contraction forces', *Med. Biol. Eng. Comput.*, vol. 42, no. 4, 2004, doi: 10.1007/BF02350989.

[67] F. Negro, S. Muceli, A. M. Castronovo, A. Holobar, and D. Farina, 'Multi-channel intramuscular and surface EMG decomposition by convolutive blind source separation', *J. Neural Eng.*, vol. 13, no. 2, 2016, doi: 10.1088/1741-2560/13/2/026027.

[68] M. Chen and P. Zhou, 'A novel framework based on FastICA for high density surface EMG decomposition', *IEEE Trans. Neural Syst. Rehabil. Eng.*, vol. 24, no. 1, pp. 117–127, 2016, doi: 10.1109/TNSRE.2015.2412038.

[69] J. Lundsberg, A. Björkman, N. Malesevic, and C. Antfolk, 'Compressed spike-triggered averaging in iterative decomposition of surface EMG', *Comput. Methods Programs Biomed.*, vol. 228, p. 107250, 2022, doi: 10.1016/j.cmpb.2022.107250.

[70] A. K. Clarke *et al.*, 'Deep Learning for Robust Decomposition of High-Density Surface EMG Signals', *IEEE Trans. Biomed. Eng.*, vol. 68, no. 2, pp. 526–534, Feb. 2021, doi: 10.1109/TBME.2020.3006508.

[71] G. R. Naik, S. E. Selvan, M. Gobbo, A. Acharyya, and H. T. Nguyen, 'Principal Component Analysis Applied to Surface Electromyography: A Comprehensive Review', *IEEE Access*, vol. 4, pp. 4025–4037, 2016, doi: 10.1109/ACCESS.2016.2593013.

[72] A. Hyvärinen and E. Oja, 'Independent component analysis: algorithms and applications', *Neural Netw.*, vol. 13, no. 4, pp. 411–430, Jun. 2000, doi: 10.1016/S0893-6080(00)00026-5.

[73] D. Lee and H. S. Seung, 'Algorithms for Non-negative Matrix Factorization', in *Advances in Neural Information Processing Systems*, MIT Press, 2000. Accessed: May 21, 2023. [Online]. Available: https://proceedings.neurips.cc/paper_files/paper/2000/hash/f9d1152547c0bde01830b7e8bd60024c-Abstract.html

[74] A. Belouchrani and A. Cichocki, 'A Robust Whitening Procedure in Blind Source Separation Context 2 Data Model', pp. 1–7, 2000.

[75] A. Holobar, M. A. Minetto, A. Botter, F. Negro, and D. Farina, 'Experimental analysis of accuracy in the identification of motor unit spike trains from high-density surface EMG', *IEEE Trans. Neural Syst. Rehabil. Eng.*, vol. 18, no. 3, pp. 221–229, 2010, doi: 10.1109/TNSRE.2010.2041593.

[76] E. Martinez-Valdes, F. Negro, C. M. Laine, D. Falla, F. Mayer, and D. Farina, 'Tracking motor units longitudinally across experimental sessions with high-density surface electromyography', *J. Physiol.*, vol. 595, no. 5, pp. 1479–1496, 2017, doi: 10.1113/JP273662.

[77] A. Del Vecchio, A. Holobar, D. Falla, F. Felici, R. M. Enoka, and D. Farina, 'Tutorial: Analysis of motor unit discharge characteristics from high-density surface EMG signals', *J. Electromyogr. Kinesiol.*, vol. 53, p. 102426, 2020, doi: 10.1016/j.jelekin.2020.102426.

[78] P. Povalej Bržan *et al.*, 'New Perspectives for Computer-Aided Discrimination of Parkinson's Disease and Essential Tremor', *Complexity*, vol. 2017, p. e4327175, Oct. 2017, doi: 10.1155/2017/4327175.

[79] R. J. Elble and J. E. Randall, 'Motor-unit activity responsible for 8- to 12-Hz component of human physiological finger tremor', *J. Neurophysiol.*, vol. 39, no. 2, pp. 370–383, Mar. 1976, doi: 10.1152/jn.1976.39.2.370.

[80] A. Holobar, V. Glaser, J. A. Gallego, J. L. Dideriksen, and D. Farina, 'Non-invasive characterization of motor unit behaviour in pathological tremor', *J. Neural Eng.*, vol. 9, no. 5, p. 056011, Oct. 2012, doi: 10.1088/1741-2560/9/5/056011.

[81] M. A. Islam, K. Sundaraj, R. B. Ahmad, and N. U. Ahamed, 'Mechanomyogram for Muscle Function Assessment: A Review', *PLoS ONE*, vol. 8, no. 3, 2013, doi: 10.1371/journal.pone.0058902.

[82] C. Orizio, 'Muscle sound: Bases for the introduction of a mechanomyographic signal in muscle studies', *Crit. Rev. Biomed. Eng.*, vol. 21, no. 3, pp. 201–243, 1993.

[83] C. Meagher *et al.*, 'New advances in mechanomyography sensor technology and signal processing: Validity and intrarater reliability of recordings from muscle', *J. Rehabil. Assist. Technol. Eng.*, vol. 7, p. 205566832091611, 2020, doi: 10.1177/2055668320916116.

[84] Y. Yoshitake, M. Shinohara, H. Ue, and T. Moritani, 'Characteristics of surface mechanomyogram are dependent on development of fusion of motor units in humans', *J. Appl. Physiol.*, vol. 93, no. 5, pp. 1744–1752, Nov. 2002, doi: 10.1152/japplphysiol.00008.2002.

[85] Y. Yoshitake, Y. Kawakami, H. Kanehisa, and T. Fukunaga, 'Surface Mechanomyogram Reflects Length Changes in Fascicles of Human Skeletal muscles', *Int. J. Sport Health Sci.*, vol. 3, no. Special_Issue_2, pp. 280–285, 2005, doi: 10.5432/ijshs.3.280.

[86] C. Cescon, M. Gazzoni, M. Gobbo, C. Orizio, and D. Farina, 'Non-invasive assessment of single motor unit mechanomyographic response and twitch force by spike-triggered averaging', *Med. Biol. Eng. Comput.*, vol. 42, no. 4, pp. 496–501, 2004, doi: 10.1007/BF02350990.

[87] C. Orizio *et al.*, 'Surface mechanomyogram reflects the changes in the mechanical properties of muscle at fatigue', *Eur. J. Appl. Physiol.*, vol. 80, no. 4, pp. 276–284, 1999, doi: 10.1007/s004210050593.

[88] C. Orizio, D. Liberati, C. Locatelli, D. De Grandis, and A. Veicsteinas, 'Surface mechanomyogram reflects muscle fibres twitches summation', *J. Biomech.*, vol. 29, no. 4, 1996, doi: 10.1016/0021-9290(95)00063-1.

[89] G. R. Adams, R. T. Harris, D. Woodard, and G. A. Dudley, 'Mapping of electrical muscle stimulation using MRI', *J. Appl. Physiol.*, vol. 74, no. 2, pp. 532–537, 1993, doi: 10.1152/jappl.1993.74.2.532.

[90] B. Haddock *et al.*, 'Assessment of muscle function using hybrid PET/MRI: comparison of 18F-FDG PET and T2-weighted MRI for quantifying muscle activation in human subjects', *Eur. J. Nucl. Med. Mol. Imaging*, vol. 44, no. 4, pp. 704–711, 2017, doi: 10.1007/s00259-016-3507-1.

[91] A. Berger, 'Magnetic resonance imaging', *BMJ*, vol. 324, no. 7328, p. 35, Jan. 2002.

[92] V. Baliyan, C. J. Das, R. Sharma, and A. K. Gupta, 'Diffusion weighted imaging: Technique and applications', *World J. Radiol.*, vol. 8, no. 9, pp. 785–798, Sep. 2016, doi: 10.4329/wjr.v8.i9.785.

[93] M. G. Birkbeck, L. Heskamp, I. S. Schofield, A. M. Blamire, and R. G. Whittaker, 'Non-invasive imaging of single human motor units', *Clin. Neurophysiol.*, vol. 131, no. 6, pp. 1399–1406, 2020, doi: 10.1016/j.clinph.2020.02.004.

[94] M. G. Birkbeck, A. M. Blamire, R. G. Whittaker, A. A. Sayer, and R. M. Dodds, 'The role of novel motor unit magnetic resonance imaging to investigate motor unit activity in ageing skeletal muscle', *J. Cachexia Sarcopenia Muscle*, vol. 12, no. 1, pp. 17–29, 2021, doi: 10.1002/jcsm.12655.

[95] R. G. Whittaker, P. Porcari, L. Braz, T. L. Williams, I. S. Schofield, and A. M. Blamire, 'Functional magnetic resonance imaging of human motor unit fasciculation in amyotrophic lateral sclerosis', *Ann. Neurol.*, vol. 85, no. 3, pp. 455–459, Mar. 2019, doi: 10.1002/ana.25422.

[96] L. Heskamp, M. G. Birkbeck, R. G. Whittaker, I. S. Schofield, and A. M. Blamire, 'The muscle twitch profile assessed with motor unit magnetic resonance imaging', *NMR Biomed.*, vol. 34, no. 3, pp. 1–15, 2021, doi: 10.1002/nbm.4466.

[97] F. O. Walker, 'Neuromuscular ultrasound', *Neurol. Clin.*, vol. 22, no. 3, pp. 563–590, vi, Aug. 2004, doi: 10.1016/j.ncl.2004.03.004.

[98] J. Wijntjes and N. van Alfen, 'Muscle ultrasound: Present state and future opportunities', *Muscle Nerve*, vol. 63, pp. 455–466, 2020, doi: 10.1002/mus.27081.

[99] P. W. Hodges, L. H. M. Pengel, R. D. Herbert, and S. C. Gandevia, 'Measurement of muscle contraction with ultrasound imaging', *Muscle Nerve*, vol. 27, no. 6, pp. 682–692, 2003, doi: 10.1002/mus.10375.

[100] T. L. Szabo, *Diagnostic Ultrasound Imaging: Inside Out*. New York, NY, USA: Academic Press, 2014. doi: 10.1016/C2011-0-07261-7.

[101] K. M. Meiburger, U. R. Acharya, and F. Molinari, 'Automated localization and segmentation techniques for B-mode ultrasound images: A review', *Comput. Biol. Med.*, vol. 92, no. November 2017, pp. 210–235, 2018, doi: 10.1016/j.compbiomed.2017.11.018.

[102] J. K. Mah and N. V. Alfen, 'Neuromuscular Ultrasound : Clinical Applications and Diagnostic Values', pp. 605–619, 2021, doi: 10.1017/cjn.2018.314.

[103] J. L. Gennisson, T. Deffieux, E. Macé, G. Montaldo, M. Fink, and M. Tanter, 'Viscoelastic and anisotropic mechanical properties of in vivo muscle tissue assessed by supersonic shear imaging', *Ultrasound Med. Biol.*, vol. 36, no. 5, pp. 789–801, 2010, doi: 10.1016/j.ultrasmedbio.2010.02.013.

[104] Y. T. Ling, C. Z. H. Ma, Q. T. K. Shea, and Y. P. Zheng, 'Sonomechanomyography (SMMG): Mapping of skeletal muscle motion onset during contraction using ultrafast ultrasound imaging and multiple motion sensors', *Sens. Switz.*, vol. 20, no. 19, pp. 1–13, 2020, doi: 10.3390/s20195513.

[105] O. Maïsetti, F. Hug, K. Bouillard, and A. Nordez, 'Characterization of passive elastic properties of the human medial gastrocnemius muscle belly using supersonic shear imaging', *J. Biomech.*, vol. 45, no. 6, pp. 978–984, 2012, doi: 10.1016/j.jbiomech.2012.01.009.

[106] A. Nordez and F. Hug, 'Muscle shear elastic modulus measured using supersonic shear imaging is highly related to muscle activity level', *J. Appl. Physiol.*, vol. 108, no. 5, pp. 1389–1394, 2010, doi: 10.1152/japplphysiol.01323.2009.

[107] B. J. Raiteri, A. G. Cresswell, and G. A. Lichtwark, 'Muscle-Tendon length and force affect human tibialis anterior central aponeurosis stiffness in vivo', *Proc. Natl. Acad. Sci. U. S. A.*, vol. 115, no. 14, pp. E3097–E3105, 2018, doi: 10.1073/pnas.1712697115.

[108] T. Fukunaga, Y. Kawakami, S. Kuno, K. Funato, and S. Fukashiro, 'Muscle architecture and function in humans', *J. Biomech.*, vol. 30, no. 5, pp. 457–463, 1997, doi: 10.1016/S0021-9290(96)00171-6.

[109] C. N. Maganaris, 'Force-length characteristics of in vivo human skeletal muscle', *Acta Physiol. Scand.*, vol. 172, no. 4, pp. 279–285, 2001, doi: 10.1046/j.1365-201X.2001.00799.x.

[110] C. N. Maganaris, V. Baltzopoulos, and A. J. Sargeant, 'In vivo measurements of the triceps surae complex architecture in man: Implications for muscle function', *J. Physiol.*, vol. 512, no. 2, pp. 603–614, 1998, doi: 10.1111/j.1469-7793.1998.603be.x.

[111] I. D. Loram, C. N. Maganaris, and M. Lakie, 'Use of ultrasound to make noninvasive in vivo measurement of continuous changes in human muscle contractile length', *J. Appl. Physiol.*, vol. 100, no. 4, pp. 1311–1323, 2006, doi: 10.1152/japplphysiol.01229.2005.

[112] C. N. Maganaris and V. Baltzopoulos, 'Predictability of in vivo changes in pennation angle of human tibialis anterior muscle from rest to maximum isometric

dorsiflexion', *Eur. J. Appl. Physiol.*, vol. 79, no. 3, pp. 294–297, Jan. 1999, doi: 10.1007/s004210050510.

[113] H. Yamada, N. Ihara, and Y. Sano, 'Determination of fascicle length and pennation in a contracting human muscle in vivo', *J. Appl. Physiol.*, vol. 34, no. 2, pp. 319–323, 1997, doi: 10.1507/endocrj1954.34.319.

[114] R. D. Herbert, A. M. Moseley, J. E. Butler, and S. C. Gandevia, 'Change in length of relaxed muscle fascicles and tendons with knee and ankle movement in humans', *J. Physiol.*, vol. 539, no. 2, pp. 637–645, 2002, doi: 10.1013/jphysiol.2001.012756.

[115] O. R. Seynnes and N. J. Cronin, 'Simple Muscle Architecture Analysis (SMA): an ImageJ macro tool to automate measurements in B-mode ultrasound scans', *PLOS ONE*, vol. 15, no. 2, 2020.

[116] J. G. Gillett, R. S. Barrett, and G. A. Lichtwark, 'Reliability and accuracy of an automated tracking algorithm to measure controlled passive and active muscle fascicle length changes from ultrasound', *Comput. Methods Biomech. Biomed. Engin.*, vol. 16, no. 6, pp. 678–687, 2013, doi: 10.1080/10255842.2011.633516.

[117] T. Miyoshi, T. Kihara, H. Koyama, S. I. Yamamoto, and T. Komeda, 'Automatic detection method of muscle fiber movement as revealed by ultrasound images', *Med. Eng. Phys.*, vol. 31, no. 5, pp. 558–564, 2009, doi: 10.1016/j.medengphy.2008.11.004.

[118] D. J. Farris and G. A. Lichtwark, 'UltraTrack: Software for semi-automated tracking of muscle fascicles in sequences of B-mode ultrasound images', *Comput. Methods Programs Biomed.*, vol. 128, pp. 111–118, 2016, doi: 10.1016/j.cmpb.2016.02.016.

[119] N. J. Cronin, C. P. Carty, R. S. Barrett, and G. Lichtwark, 'Automatic tracking of medial gastrocnemius fascicle length during human locomotion', *J. Appl. Physiol.*, vol. 111, no. 5, pp. 1491–1496, 2011, doi: 10.1152/japplphysiol.00530.2011.

[120] J. Darby, E. F. Hodson-Tole, N. Costen, and I. D. Loram, 'Automated regional analysis of B-mode ultrasound images of skeletal muscle movement', *J. Appl. Physiol.*, vol. 112, no. 2, pp. 313–327, 2012, doi: 10.1152/japplphysiol.00701.2011.

[121] M. Carbonaro, O. R. Seynnes, N. A. Maffiuletti, C. Busso, M. A. Minetto, and A. Botter, 'Architectural changes in superficial and deep compartments of the tibialis anterior during electrical stimulation over different sites', *IEEE Trans. Neural Syst. Rehabil. Eng.*, vol. 28, no. 10, pp. 2557–2565, 2020.

[122] J. Ophir, I. Céspedes, H. Ponnekanti, Y. Yazdi, and X. Li, 'Elastography: A quantitative method for imaging the elasticity of biological tissues', *Ultrason. Imaging*, vol. 13, no. 2, pp. 111–134, 1991, doi: 10.1177/016173469101300201.

[123] J. Ophir *et al.*, 'Elastography: Ultrasonic estimation and imaging of the elastic properties of tissues', *Proc. Inst. Mech. Eng. [H]*, vol. 213, no. 3, pp. 203–233, 1999, doi: 10.1243/0954411991534933.

[124] J. Ophir *et al.*, 'Elastography: Imaging the elastic properties of soft tissues with ultrasound', *J. Med. Ultrason.*, 2002, doi: 10.1007/bf02480847.

[125] A. P. Sarvazyan, O. V. Rudenko, S. D. Swanson, J. B. Fowlkes, and S. Y. Emelianov, 'Shear wave elasticity imaging: A new ultrasonic technology of medical diagnostics', *Ultrasound Med. Biol.*, vol. 24, no. 9, pp. 1419–1435, 1998, doi: 10.1016/S0301-5629(98)00110-0.

[126] T. Deffieux, G. Montaldo, M. Tanter, and M. Fink, 'Shear wave spectroscopy for in vivo quantification of human soft tissues visco-elasticity', *IEEE Trans. Med. Imaging*, vol. 28, no. 3, pp. 313–322, 2009, doi: 10.1109/TMI.2008.925077.

[127] L. Sandrin, M. Tanter, S. Catheline, and M. Fink, 'Shear modulus imaging with 2-D transient elastography', *IEEE Trans. Ultrason. Ferroelectr. Freq. Control*, vol. 49, no. 4, pp. 426–435, 2002, doi: 10.1109/58.996560.

[128] L. Sandrin, S. Catheline, M. Tanter, X. Hennequin, and M. Fink, 'Time-resolved pulsed elastography with ultrafast ultrasonic imaging', *Ultrason. Imaging*, vol. 21, pp. 259–272, 1999, doi: 10.1177/016173469902100402.

[129] J. Souquet and J. Bercoff, 'Ultrafast Ultrasound Imaging', *Ultrasound Med. Biol.*, vol. 37, no. 8, p. S17, 2011, doi: 10.1016/j.ultrasmedbio.2011.05.098.

[130] M. Tanter and M. Fink, 'Ultrafast imaging in biomedical ultrasound', *IEEE Trans. Ultrason. Ferroelectr. Freq. Control*, vol. 61, no. 1, pp. 102–119, 2014, doi: 10.1109/TUFFC.2014.2882.

[131] M. Fink and M. Tanter, 'Multiwave imaging and super resolution', *Phys. Today*, vol. 63, no. 2, pp. 28–33, 2010, doi: 10.1063/1.3326986.

[132] S. Seoni, G. Matrone, and K. M. Meiburger, 'Texture analysis of ultrasound images obtained with different beamforming techniques and dynamic ranges – A robustness study', *Ultrasonics*, vol. 131, p. 106940, May 2023, doi: 10.1016/j.ultras.2023.106940.

[133] M. Shinohara, K. Sabra, J. L. Gennisson, M. Fink, and M. L. Tanter, 'Real-time visualization of muscle stiffness distribution with ultrasound shear wave imaging during muscle contraction', *Muscle Nerve*, vol. 42, no. 3, pp. 438–441, 2010, doi: 10.1002/mus.21723.

[134] J. L. Gennisson, S. Catheline, S. Chaffaï, and M. Fink, 'Transient elastography in anisotropic medium: Application to the measurement of slow and fast shear wave speeds in muscles', *J. Acoust. Soc. Am.*, vol. 114, no. 1, pp. 536–541, 2003, doi: 10.1121/1.1579008.

[135] K. Sasaki, S. Toyama, and N. Ishii, 'Length-force characteristics of in vivo human muscle reflected by supersonic shear imaging', *J. Appl. Physiol.*, vol. 117, no. 2, pp. 153–162, 2014, doi: 10.1152/japplphysiol.01058.2013.

[136] F. Hug, T. Gallot, S. Catheline, and A. Nordez, 'Electromechanical delay in biceps brachii assessed by ultrafast ultrasonography', *Muscle Nerve*, vol. 43, no. 3, pp. 441–443, 2011, doi: 10.1002/mus.21948.

[137] A. Nordez, T. Gallot, S. Catheline, A. Guével, C. Cornu, and F. Hug, 'Electromechanical delay revisited using very high frame rate ultrasound', *J. Appl. Physiol.*, vol. 106, no. 6, pp. 1970–1975, 2009, doi: 10.1152/japplphysiol.00221.2009.

[138] C. Grönlund, K. Claesson, and A. Holtermann, 'Imaging Two-Dimensional mechanical waves of skeletal muscle contraction', *Ultrasound Med. Biol.*, vol. 39, no. 2, pp. 360–369, 2013, doi: 10.1016/j.ultrasmedbio.2012.09.005.

[139] R. Waasdorp *et al.*, 'Combining Ultrafast Ultrasound and High-Density EMG to Assess Local Electromechanical Muscle Dynamics: A Feasibility Study', *IEEE Access*, vol. 9, pp. 45277–45288, 2021, doi: 10.1109/ACCESS.2021.3067162.

[140] M. Peolsson, B. Larsson, L. Å. Brodin, and B. Gerdle, 'A pilot study using tissue velocity ultrasound imaging (TVI) to assess muscle activity pattern in patients with

chronic trapezius myalgia', *BMC Musculoskelet. Disord.*, vol. 9, pp. 1–15, 2008, doi: 10.1186/1471-2474-9-127.

[141] F. Lindberg, M. Mårtensson, C. Grönlund, and L. Å. Brodin, 'Evaluation of ultrasound Tissue Velocity Imaging: A phantom study of velocity estimation in skeletal muscle low-level contractions', *BMC Med. Imaging*, vol. 13, no. 1, 2013, doi: 10.1186/1471-2342-13-16.

[142] T. Loupas, R. W. Gill, and J. T. Powers, 'An Axial Velocity Estimator for Ultrasound Blood Flow Imaging, Based on a Full Evaluation of the Doppler Equation by Means of a Two-Dimensional Autocorrelation Approach', *IEEE Trans. Ultrason. Ferroelectr. Freq. Control*, vol. 42, no. 4, pp. 672–688, 1995, doi: 10.1109/58.393110.

[143] T. Deffieux, J. L. Gennisson, M. Tanter, M. Fink, and A. Nordez, 'Ultrafast imaging of in vivo muscle contraction using ultrasound', *Appl. Phys. Lett.*, vol. 89, no. 18, pp. 2006–2008, 2006, doi: 10.1063/1.2378616.

[144] T. Deffieux, J. L. Gennisson, M. Tanter, and M. Fink, 'Assessment of the mechanical properties of the musculoskeletal system using 2-D and 3-D very high frame rate ultrasound', *IEEE Trans. Ultrason. Ferroelectr. Freq. Control*, vol. 55, no. 10, pp. 2177–2190, 2008, doi: 10.1109/TUFFC.917.

[145] R. Rohlen, E. Stalberg, K. H. Stoverud, J. Yu, and C. Gronlund, 'A Method for Identification of Mechanical Response of Motor Units in Skeletal Muscle Voluntary Contractions Using Ultrafast Ultrasound Imaging - Simulations and Experimental Tests', *IEEE Access*, vol. 8, pp. 50299–50311, 2020, doi: 10.1109/ACCESS.2020.2980053.

[146] R. Rohlén, J. Lundsberg, N. Malesevic, and C. Antfolk, 'A fast blind source separation algorithm for decomposing ultrafast ultrasound images into spatiotemporal muscle unit kinematics', 2022.

[147] R. Rohlén, E. Stålberg, and C. Grönlund, 'Identification of single motor units in skeletal muscle under low force isometric voluntary contractions using ultrafast ultrasound', *Sci. Rep.*, vol. 10, no. 1, pp. 1–11, 2020, doi: 10.1038/s41598-020-79863-1.

[148] J. V. Stone, J. Porrill, N. R. Porter, and I. D. Wilkinson, 'Spatiotemporal independent component analysis of event-related fMRI data using skewed probability density functions', *NeuroImage*, vol. 15, no. 2, pp. 407–421, 2002, doi: 10.1006/nimg.2001.0986.

[149] E. Lubel *et al.*, 'Non-linearity in motor unit velocity twitch dynamics: Implications for ultrafast ultrasound source separation'. bioRxiv, p. 2023.03.24.533983, Mar. 25, 2023. doi: 10.1101/2023.03.24.533983.

[150] C. Cescon, E. Sguazzi, R. Merletti, and D. Farina, 'Non-invasive characterization of single motor unit electromyographic and mechanomyographic activities in the biceps brachii muscle', *J. Electromyogr. Kinesiol.*, vol. 16, no. 1, pp. 17–24, Feb. 2006, doi: 10.1016/j.jelekin.2005.02.005.

[151] A. Botter, T. Vieira, M. Carbonaro, G. L. Cerone, and E. F. Hodson-Tole, 'Electrodes' Configuration Influences the Agreement between Surface EMG and B-Mode Ultrasound Detection of Motor Unit Fasciculation', *IEEE Access*, vol. 9, pp. 98110–98120, 2021, doi: 10.1109/ACCESS.2021.3094665.

[152] A. Botter, M. Carbonaro, T. M. Vieira, and E. F. Hodson-Tole, 'Identification of muscle fasciculations from surface EMG: comparison with ultrasound-based detection', in *41st Annual International Conference of the IEEE Engineering in Medicine and Biology Society, EMBC 2019*, 2019, pp. 5117–5120.

[153] B. Chen and P. Zhou, 'Detection of fasciculation potentials in amyotrophic lateral sclerosis using surface EMG', in *Lecture Notes in Electrical Engineering*, 2014. doi: 10.1007/978-94-007-7618-0_302.

[154] M. De Carvalho and M. Swash, 'Fasciculation potentials: A study of amyotrophic lateral sclerosis and other neurogenic disorders', *Muscle Nerve*, vol. 21, no. 3, pp. 336–344, 1998, doi: 10.1002/(SICI)1097-4598(199803)21:3<336::AID-MUS7>3.0.CO;2-B.

[155] P. J. Harding, I. D. Loram, N. Combes, and E. F. Hodson-Tole, 'Ultrasound-Based Detection of Fasciculations in Healthy and Diseased Muscles', *IEEE Trans. Biomed. Eng.*, vol. 63, no. 3, pp. 512–518, 2016, doi: 10.1109/TBME.2015.2465168.

[156] S. Misawa *et al.*, 'Ultrasonographic detection of fasciculations markedly increases diagnostic sensitivity of ALS', *Neurology*, vol. 77, no. 16, pp. 1532–1537, 2011, doi: 10.1212/WNL.0b013e318233b36a.

[157] C. D. Reimers, U. Ziemann, A. Scheel, P. Rieckmann, M. Kunkel, and C. Kurth, 'Fasciculations: Clinical, electromyographic, and ultrasonographic assessment', *J. Neurol.*, 1996, doi: 10.1007/BF00900945.

[158] A. Botter, T. M. Vieira, I. D. Loram, R. Merletti, and E. F. Hodson-Tole, 'A novel system of electrodes transparent to ultrasound for simultaneous detection of myoelectric activity and B-mode ultrasound images of skeletal muscles', *J. Appl. Physiol.*, vol. 115, no. 8, pp. 1203–1214, 2013, doi: 10.1152/japplphysiol.00090.2013.

[159] E. Martinez-Valdes *et al.*, 'Modulations in motor unit discharge are related to changes in fascicle length during isometric contractions', *J. Appl. Physiol.*, vol. 133, no. 5, pp. 1136–1148, Nov. 2022, doi: 10.1152/japplphysiol.00758.2021.

Chapter 3

Topic 1

3.1 Integration of HDsEMG and UUS data

The previous Chapter provided an overview of the current state of the art of technologies and methods for evaluating muscle excitation and contraction. It was shown that HDsEMG can provide information about muscle activation at the global level and at single motor units (MUs) level, while ultrafast ultrasound (UUS) can assess movements with fast dynamics through the analysis of cross-sectional tissue velocity sequences and it was thus proposed for the study of single MU activity. The integration of both techniques has therefore the potential to provide a more comprehensive description of the neuromechanical MU properties.

To achieve this, we propose an integrated HDsEMG-UUS approach to simultaneously identify and analyze the neural, electrical, anatomical, and mechanical characteristics of single motor units (Figure 3.1). This approach involves extracting single MU firings from HDsEMG and using this information to identify the corresponding muscle movements in US images, which define the motor unit territory and twitching characteristics of the tissue. This integration represents an innovative approach in this field of investigation. In fact, we used an extensively validated method for the identification of MU activity (HDsEMG decomposition) and we used this information in the pipeline for the identification of the corresponding MU representation in UUS images.

Two algorithms were evaluated in this study to process the data detected from joint HDsEMG-UUS measures. The first algorithm (*STA-based algorithm*) makes use of spike-

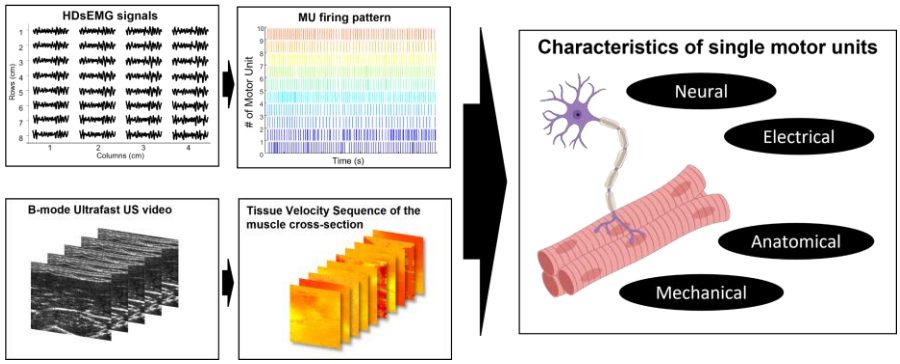

Figure 3.1 Integration of HDsEMG and ultrafast US. Scheme of the proposed approach integrating HDsEMG and ultrafast ultrasound data to achieve the description of the neural, electrical, anatomical, and mechanical characteristics of single motor units.

triggered averaging (STA) of the tissue displacement velocity sequence based on the individual MU firings [1]. This technique has been previously used in this context to study the representation in mechanomyograms of single MU activity [2]. The second algorithm (*stICA-based algorithm*) employs spatio-temporal independent component analysis (stICA) for processing ultrafast US muscle images [3]. This technique has been suggested as a method to decompose the displacement velocity sequence and obtain information about individual mechanical responses of muscle units [4]–[6]. Both algorithms (STA-based and stICA-based) characterize each MU by its *spatial representation* in ultrasound images and its *velocity profile* in the time domain.

In the following sections, the pipelines of the two algorithms are described in detail. Afterwards, the development of a simulated environment of HDsEMG and UUS data is proposed to systematically assess the two algorithms outcome in the identification of the anatomical and electrophysiological characteristics of the simulated MUs.

Underlying assumptions

The algorithms described in the following sections are based on the hypothesis that the movement of the muscle region comprising the active fibers is related with the corresponding MU neural input. While this is a reasonable, initial hypothesis, it is worth noting that it is based on a simplified model of muscle tissue dynamic where possible non-linearities due to the multiple MU interactions are neglected and where the region of movement strictly corresponds to the MU territory (Figure 3.2). Mechanical interactions between active MUs increase with the number of active MUs (i.e. contraction level), moreover the movement associated to MU activation can be represented in other muscle regions in case of pinnate muscle architecture (Figure 3.2b). Therefore, in order to limit the effect of the aforementioned factors we considered low contraction levels and fusiform muscle geometry (Figure 3.2a).

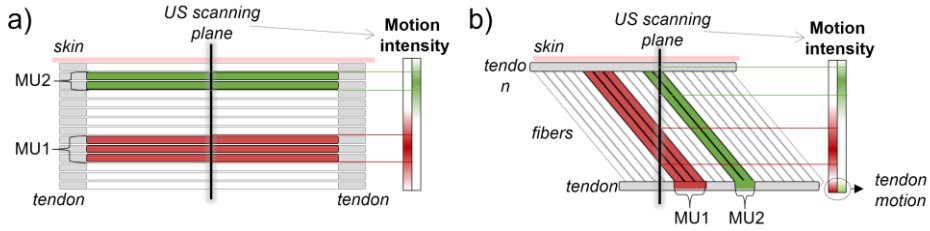

Figure 3.2 Theoretical considerations about muscle motion. (a) Example of 2 active MUs in a fusiform muscle creating regions of movement in the ultrasound scanning plane limited to the MU territory. (b) In case of a pinnate muscle, motions are detectable in the tendon region, other than in the MU territory.

3.1.1 Algorithm based on the averaging of the tissue velocity with single MU firings (*STA-based*)

Figure 3.3 shows an outline of the first algorithm considered (STA-based algorithm). The spike-triggered averaging (STA) technique is based on the averaging of epochs of signal using spike instants as reference input. We used the firing instants of single MU (either simulated or obtained from HDsEMG decomposition) to trigger epochs of the tissue velocity sequence of the muscle cross-section. A 125-ms averaging epoch was selected as it corresponds approximately to the contracting and half relaxation time of an electrically-elicited bundle of muscle fibers [7]. The averaging process resulted in a velocity sequence in which the contribution of the triggering MU to the tissue velocity should be emphasized. We aimed to extract a localized twitching region in the average sequence separated from the background activity. From the average sequence, we removed the mean value computed across frames and we then identified the frame with maximum velocity. It was assumed that the image region where the maximum velocities was observed in the averaged

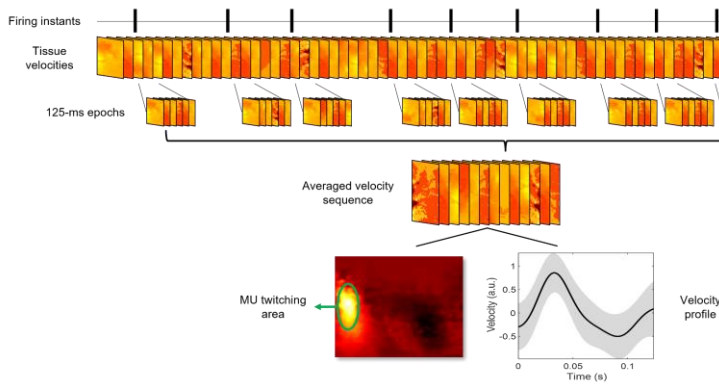

Figure 3.3 Spike Triggered Averaging of the tissue velocities. Example of the averaging technique of the tissue velocity sequence estimate from ultrafast ultrasound data. 125-ms epochs around each firing instant were considered and averaged such to obtain a sequence in which the contribution of a motor unit is emphasized. In the final step, an image of the spatial representation and temporal profile of the twitching MU were extracted.

sequence corresponds to the area where MU fibers are located, as all the movements associated with other MU activity should be uncorrelated, thus filtered by the averaging process. We further averaged the velocity sequence across the 20 ms frames around the maximum frame (10 ms before and 10 ms after) to create a single image. This image can be considered as a spatial representation of the twitching MU. We applied a global threshold of 70% of the maximum to this image to segment the area of twitching (*MU twitching area*). It is worth noting that this twitching area does not correspond to the MU territory as classically defined, it is instead the tissue area where the MU contraction induces movements within the muscle cross section. Due to passive force transmission in the transversal plane this area is an overestimation of the actual MU territory which likely depends on the muscle architecture. The brightness (i.e. velocities) of the segmented pixels may follow a velocity profile similar (*velocity twitch*) to that shown in electrically stimulated contraction in time [7]. During electrically stimulated contractions, the muscle tissue showed a specific pattern, with an initial increase in velocity (contraction) followed by a gradual decrease (relaxation) as the contraction progresses [7]. The segmented pixels, which likely represent specific regions possibly related to MU contraction and relaxation, may show a similar trend in their brightness when followed in time, i.e. increasing brightness at the beginning (increasing velocities) and a decreasing towards the end of the sequence (Figure 3.3).

3.1.2 Algorithm based on the decomposition of displacement velocity and correlation with MU firing activity (stICA-based)

Figure 3.4 shows the processing of the stICA-based algorithm. The method was always based on a combination of HDsEMG (Figure 3.4a) and 2D tissue velocity sequences (TVS) computed from ultrafast US images of muscle cross-section (Figure 3.4d,e). Unlike the first algorithm, the TVS was further processed applying spatio-temporal independent component analysis (stICA) [3] to regions of interest (ROI) covering the entire image [5] (Figure 3f, see paragraph *"Spatio-temporal independent component analysis"*). The output of the stICA provided the time courses and associated images of the independent components, hereafter referred to as *temporal* and *spatial components* respectively. Afterwards, the combined analysis with EMG was performed. The discharge instants of the individual MUs were obtained from HDsEMG decomposition [8] (Figure 3.4b). For each decomposed MU we computed the convolution between the firing instants and a synthetic waveform representing the average velocity profile of the contracting fibers in the superficial-deep axis. This convolution provided, for each decomposed MU, a synthetic signal referred to as *train of the MU velocity twitches* (thick line in Figure 3.4c). This signal was cross-correlated with the temporal components obtained for each ROI (see paragraph *"Cross-correlation with MU firing activity"*) allowing to identify pairs of temporal and spatial components maximally correlated with the MU activity. Finally, the identified

spatial components were used to determine the spatial representation of the mechanical response in US images (Figure 3.4g). This spatial representation can be considered equivalent to the MU twitching area identified by the first algorithm.

Spatio-temporal independent component analysis

We decomposed the TVS by sliding a ROI of 12 × 12 mm across the entire image (40 × 40 mm) (Figure 3.4d) [5]. The sliding step was 1.6 mm in both directions (2.56 mm^2). We chose the size and step of the ROI based on two factors: the estimated size of MU territories in the biceps brachii muscle and the spatial resolution of the correlation maps obtained from the sliding ROIs. The ROI size was determined to encompass all fibers of a single contracting MU, with an estimated maximal territory size of approximately 80 mm^2 (territory diameter < 10 mm). This size was selected to minimize the influence of other sources on the velocity values. The sliding step, set at 1.6 mm in both directions (equivalent to 2.56 mm^2), aimed to provide around 30 samples (i.e., ROIs) per image within the territory of the largest MU observed in the experimental protocol conducted on the biceps brachii muscle (MU territory: 80 mm^2) [9].

We applied singular value decomposition (SVD) to each ROI and retained the 50 most significant eigenimages and corresponding eigensequences [4]. Finally, spatio-temporal independence between the sets of eigenimages and eigensequences was optimized with independent component analysis (ICA) obtaining 50 *ultrasound components* per ROIs, comprising the spatial components (i.e. images) and corresponding temporal components (i.e. time courses) (Figure 3.4f) [5]. We used a greater number of components compared to previous studies to enhance the probability of isolating distinct contributions of individual MUs to the tissue velocity sequence [5].

Cross-correlation with MU firing activity

We performed an analysis between the decomposed ultrasound components and the decomposed MU firing instants for each ROI. The following procedure was considered: (i) the convolution between the firing instants of each MU and a synthetic waveform (representing the velocity of the contracting phase of fibers lasting 50 ms [7]) produced what we refer to as the *train of MU velocity twitches* (Figure 3.4c); (ii) the cross-correlation between these trains and each of the time courses of the component was computed (Figure 3.4g); (iii) the component with the maximum correlation coefficient within a ±20 ms time lag was selected [10]. The length of the time lag was selected considering the electromechanical delay between the neural input and the movement of the muscle tissue [11], [12].

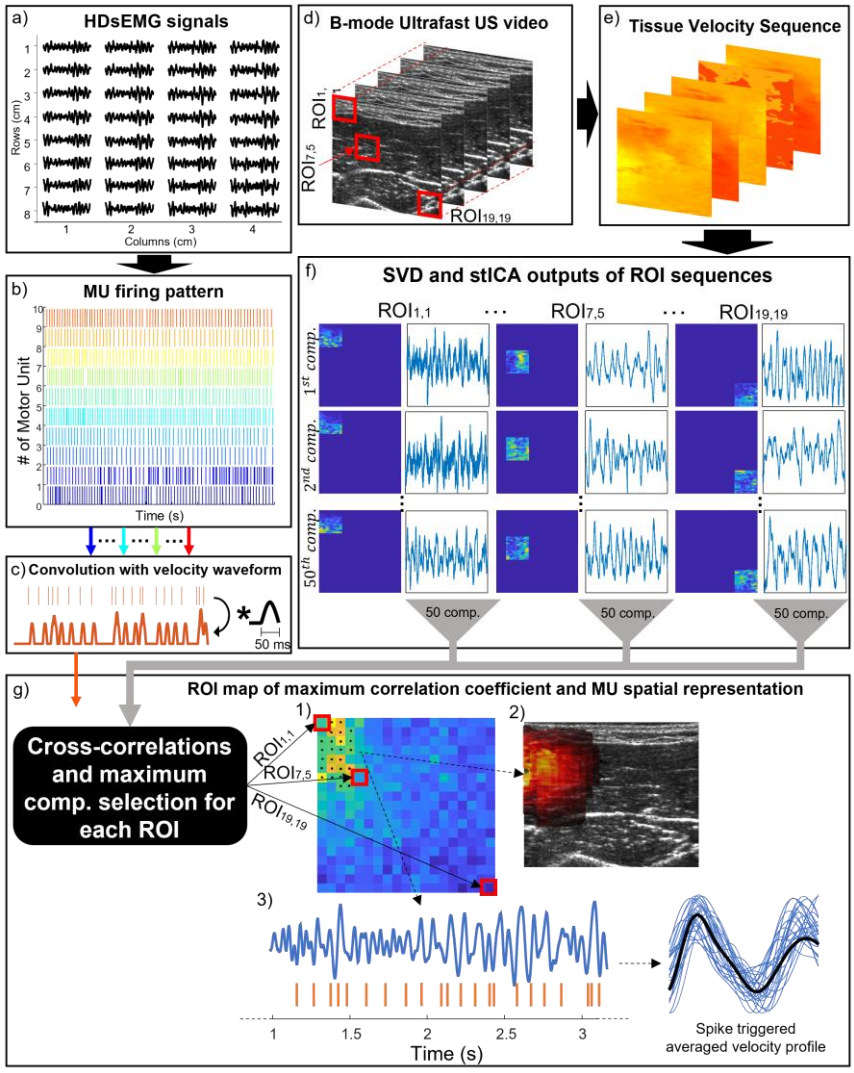

Figure 3.4 Overview of the algorithm based on the decomposition of tissue velocities and correlation with MU firings. (a) HDsEMG signals of a grid of electrodes. (b) Decomposed MU firing pattern from HDsEMG signals. (c) Generation of the train of MU displacement velocities through the convolution of the MU firing pattern with the synthetic velocity profile. (d) Ultrafast US B-mode sequence with 3 examples of ROI used in the analysis. (e) Tissue Velocity Sequence estimated using 2D autocorrelation approach. (f) Output of the Singular Value Decomposition and spatiotemporal Independent Component Analysis of the three example ROIs with 50 components (comp.) each composed by a time course (temporal component) and a correspondent image (spatial component). (g) Integration between EMG and US variables: cross-correlations between all the temporal components of the tissue velocity sequence of the ROIs and the synthetic train of MU displacement velocities, and example outcome for a single MU. (1) Map of maximum correlation coefficient of all the ROIs (19 × 19). The algorithm extracted the component with the maximum correlation within ± 20 ms time lag for each ROI. The selected ROIs (cluster) are highlighted with black dots. (2) heatmap of the MU spatial representation in US images extracted summing the spatial components of the most correlated ROIs in the coefficient map (black dots); (3) tissue displacement velocity profile (black solid line) calculated from spike triggered averaging of the temporal signal (average of all identified [i.e. black dots] temporal components) with the MU firing instants.

The correlation coefficient values of the selected component for each ROI were used to generate a *correlation map* for each decomposed MU (Figure 3.4g_1), in which each pixel represented a ROI and its color was scaled with the peak of the cross-correlation. To obtain a spatial representation of the MU mechanical response (region of movement, Figure 3.4g_2), a larger cluster of connected ROIs in the correlation map with values higher than 50% of the maximum correlation was retained (black dots in Figure 3.4g_1), and the corresponding spatial components of the ROIs were summed to obtain an image of a single MU region of activation/movement. As for the STA-based algorithm, a global thresholding at 70% of the maximum was applied to this image to determine the *MU twitching area*. The threshold for identifying the cluster of connected ROIs was determined through preliminary analysis conducted under simulated conditions. The analysis revealed that a threshold of 50% yielded the smallest error between the centroids of the simulated MU territory and the estimated representation of MU spatial distribution (refer to the following section 3.2.2).

The temporal components of the identified cluster were averaged for each time instant to obtain an individual temporal signal representing the time evolution of the contracting tissue associated with a specific MU. Using spike-triggered averaging based on the MU firing pattern, the tissue displacement velocity profile (*velocity twitch*) was calculated from the previously computed time evolution of the contracting tissue (Figure 3.4g_3).

3.2 Comparison of the algorithm for the detection of anatomical characteristic of single MU

The algorithms described in the previous sections were initially analyzed and tested under simulated conditions. The comparison of these two algorithms in a simulated environment allows to systematically control the testing conditions and parameters leading to the generation of MU firing patterns and TVS. Two important aspects of muscle contraction are the degree of neural excitation (i.e., the number of active MUs) and the level of MU synchronization (i.e. the degree of dependency between firing instants of different MUs). These aspects are critical for our algorithms. As previously mentioned, the spatial and temporal overlapping of active MUs produce more interferential mechanical responses. The degree of neural excitation increases when higher force levels are reached, with more MUs that fire at higher frequency and produce overlapping tissue movements. The other aspect affecting the system is related to the MU synchronization. The mechanical response of synchronous MU might not be separated by our algorithms resulting in fused territories.

The performance of the two methods outlined in the previous section was evaluated in a simulated fusiform muscle adjusting these parameters. The comparison was based on metrics quantifying the anatomical characteristics of MU, such as the location and the dimension of the identified MU twitching area, and the comparison with respect to simulated territory.

3.2.1 Simulation model

The simulations were built on a Matlab-implemented cylindrical volume conductor model with skin-parallel fibers (R2020b, The MathWorks Inc., MA, USA) [13]. A muscle with an elliptical cross-sectional area (CSA) of anisotropic tissue, an outer isotropic subcutaneous tissue covered by a layer of skin [14] made up the cylindrical volume conductor (Figure 3.5a). The anatomical model's parameters, which were chosen to accurately reflect the human biceps brachii (BB) muscle [15], are listed in Table 3.1. MU territories were modelled as having circular boundaries and being dispersed randomly throughout the muscle (Figure 3.5b). The MU territory is defined as the circular area encompassing all the MU fibers.

MU firing patterns

A model of recruitment of a population of MUs [16] was used to replicate a fixed percentage of maximum voluntary contraction (MVC). In particular, we simulated four ten-second steady contractions with an increasing number of MUs and correspondingly higher MVC percentages for each contraction. In total, 32, 74, 106, and 138 active MUs were recruited during the 2%, 5%, 10%, and 20% MVC contractions, respectively. We applied also two degrees of synchronization between active MUs for each contraction, using the method suggested by Yao et al. [17]. In summary, the firing pattern was first generated on the basis of the mean firings rates and inter-pulse variability following the standard model of recruitment proposed by Fuglevand et al. [16]. Afterwards, some firing instants were

Table 3.1 Parameters of the cylindrical muscle model.

	Model Parameter	Value
Motor unit properties	Fiber density	~135 fib/mm^2
	Discharge rate	8–15 pps
	CoV of interspike interval	15%
Muscle properties	Number of motor units	200
	Number of muscle fibers	80 000
	Number of MU fibers (range)	150–1500
	Muscle CSA	598 mm^2
Limb properties	Skin thickness	1 mm
	Subcutaneous tissue thickness	2.5 mm
	Bone (radius)	20 mm

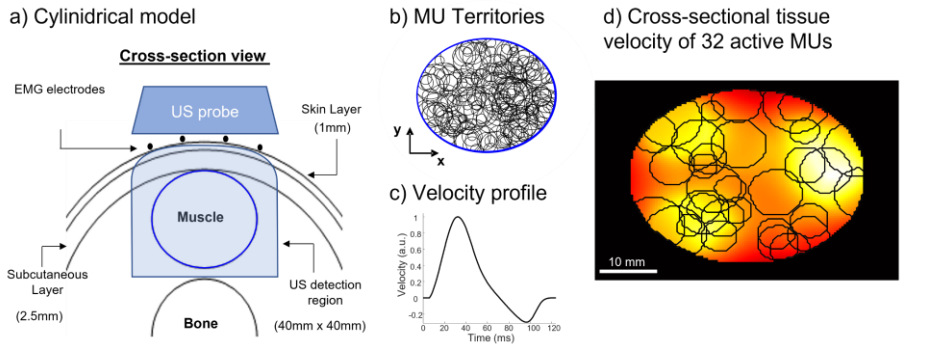

Figure 3.5 Simulation model of cylindrical muscle. (a) Cross-section of the cylindrical volume conductor model of the limb: 1 mm skin layer, 2.5 mm subcutaneous layer and elliptical-shaped muscle (598 mm^2 physiological cross-section area). The blue-shaded area is the US detection region (40 mm × 40 mm), including the whole muscle. (b) Distribution of MU territories (area range 5–44 mm2) inside the simulated muscle. (c) Normalized velocity profile of the tissue velocity simulation model. (d) Example of a frame of the simulated TVS at 2% MVC with the location of the 32 active MUs (gray circles).

adjusted to change the degree of MU synchronization, as it may affect the performance of the algorithms [18]. The percentage of firings in each train of pulses that were synchronized with other firings (%F) and the percentage of MUs firing in synchronization, expressed as a percentage of the total number of MUs (%M), specifically defined the synchronization level. Given %F and %M, the predetermined number of firings for each train were synchronized with others by shifting their firing instants. The firings that were to be synchronized were shifted considering a Gaussian random variable with a mean of 0 and a standard deviation of 2 ms. The two parameters describing MU synchronization (%F and %M) were set to be equal to minimize the number of parameters needed to describe central changes. MU synchronization levels between a medium (15%) and a very high (25%) degree [18] were considered.

EMG generation and detection

The interferential EMG signals were simulated starting from the anatomical characteristic of the muscle and the firing patterns [13], considering an high density grid of four columns in the transverse direction of the cylindrical muscle and eight rows along the fiber direction (Figure 3.5a). The interelectrode distance was set to 10 mm. The grid was centered with respect to the innervation zone of the fibers. The single MUAP was calculated using longitudinal single differential derivation (along the fiber direction) for further analysis.

Tissue velocity sequences

The model of generation of tissue velocity sequences was developed within this project to complement the EMG model described in the previous section. Tissue velocity

sequences (TVS) were simulated at 1024 frames per second. The images were 128 × 128 pixels and had a spatial resolution of 0.3 mm for a field of view of 40 × 40 mm (Figure 3.5d). The sequences of the four contractions were simulated by combining the anatomical characteristics of the muscle model (Table 3.1), firing pattern of the contractions, and mechanical model of single MUs. This model describes the spatiotemporal velocity profiles of the MU fibers in the muscle cross-section in response to a single firing. We considered the simulated velocity profile shown in Figure 3.5c, which represents the contraction (positive) and relaxation (negative) phases of a group of contracting fibers (i.e. *mechanical twitch)*. This profile was based on the work of Deffieux and colleagues, describing the muscle tissue velocity profile of the biceps brachii in response to an electrical stimulus [7]. In this manuscript the Authors used ultrafast ultrasound to characterize changes in tissue velocity profile induced by electrical stimulation at increasing amplitudes. They observed that the maximum tissue velocity was associated quadratically to the stimulation amplitude and consequently the dimensions of the active muscle territory. Therefore, a quadratic law was used to scale the amplitude of the velocity profile with the area of the MU territory (i.e., the number of fibers, Figure 3.6a) and assigned it to each pixel inside the MU territory. A *velocity field* was then created for each MU, associating a velocity value to each point of the image to simulate the passive transmission of velocity to the surrounding non-active fibers (Figure 3.6b) [19]. We used a bidimensional exponential decay centered on the MU territory to scale the velocity profile of nearby pixels outside the MU territory. The velocity field simulated the spatial response of a single MU at the maximum of the mechanical twitch (i.e. velocity profile, Figure 3.5). This procedure provided the spatiotemporal mechanical response of each simulated MU. By computing the convolution between the *mechanical twitch* and the firing pattern of each MU multiplied for the *velocity field* and adding all the mechanical responses of individual MUs, the interferential tissue velocity sequence of the simulated contractions was determined (equation 3.1).

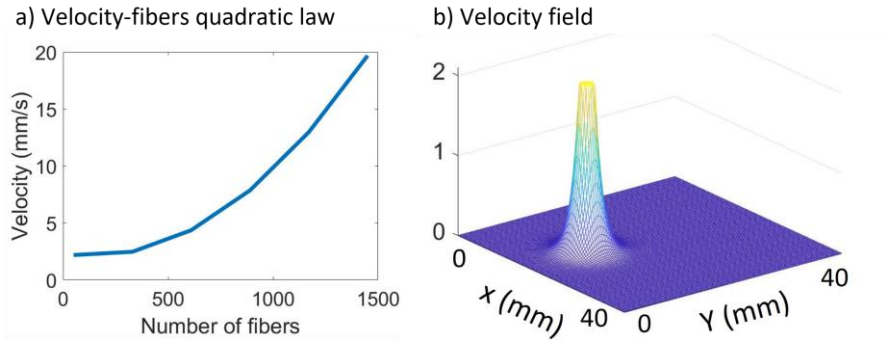

Figure 3.6 Mechanical model of single motor units. (a) Function that links the velocity to the dimension of the motor unit; the curve reflects experimental data found in the literature. (b) Example of velocity field of a MU. The velocity field simulated the spatial response of a single MU at the maximum of the mechanical twitch.

$$\boldsymbol{TVS(x,y,t) = \sum_{i=1}^{n}\sum_{j=1}^{Ni} V_i(x,y)\left[M_i(t) * \delta\left(t - t_{ij}\right)\right] + \varepsilon} \qquad 3.1$$

where n is the number of active MUs, $V_i(x,y)$ is the velocity field of the i-th MU (Figure 3.6b), $M_i(t)$ is the mechanical twitch (velocity profile, Figure 3.5c) of the i-th MU, N_i is the number of firing events and t_{ij} the j-th firing instant of the i-th MU, $\delta(\cdot)$ stands for the Dirac impulse, and $\mathcal{E}$ represents superimposed white noise. The assumption that the total mechanical signal is obtained by the superimposition is valid at low level contraction [20]. The velocity field can be written as:

$$\boldsymbol{V(x,y) = V_m e^{\sigma D(x,y)}} \qquad 3.2$$

where V_m represents the MU maximum velocity value (Figure 3.6a), $D(x,y)$ a spatial curve that expresses the distances of each pixel from the territory center and σ a constant decay [19].

$$\begin{cases} \boldsymbol{D(x,y) = d(x,y) - R_0} & \boldsymbol{if\ d(x,y) \geq R_0} \\ \boldsymbol{D(x,y) = 0} & \boldsymbol{if\ d(x,y) < R_0} \end{cases} \qquad 3.3$$

where $d(x,y)$ is the Euclidean distances of each pixel from the MU center and R_0 is the territory radius. In this model the value of σ was not constant but it changed depending on the size of the MU territory (R_0). Since a comprehensive description of the mechanical signal propagation in non-active tissue was not found in the literature, we arbitrarily defined the decay rate so that the tissue velocity at a distance of twice the MU territory radius, is about 50% of the velocity at the center of the territory.

3.2.2 Metrics for the performance assessment

MU twitching area (territory) and velocity profile

To define the performance of the two algorithms in the identification of MU territories from TVS sequence, we calculated the relative number of MU territories correctly identified with reference to the total number of simulated MUs. An estimated MU territory was regarded as *correctly identified* if the variables Recall and the Precision calculated with respect to the simulated territory were both greater than 0.4 [21]. We defined the MU territory (simulated) as the circular area encompassing all the MU fibers and it can thus be characterised by the x and y coordinates of the center in the space represented by the cross-sectional view of the muscle, and by the radius (Figure 3.5). The MU twitching area (estimated territory) was the output of the algorithm and corresponded to an image of a single MU region of activation/movement. Both the simulated and estimated MU territories are defined as binary maps (128 × 128 pixels) with 1 indicating the territory and 0 the

background. Comparing the two maps, we computed the aforementioned metrics for the definition of correct identification.

Geometrical variables of the territories (errors of center and area estimations) were also considered to define how the simulated parameters affected the identification. We considered: (i) the Euclidean distance between the center of the simulated and the computed territories and (ii) the difference between the area of estimated and simulated MU territories, divided by the size of the simulated one (relative error). As regards to temporal variables, we assessed the estimations of MU displacement velocity profile (twitch profile, Figure 3.5c) through the zero-lag cross correlation coefficients between the simulated velocity profiles and those identified by the two algorithms.

As mentioned in the previous paragraphs, the increasing number of active MUs produces high interference in the TVS resulting in overlapping MU territories that may be difficult to be resolved by the algorithms. Similarly, MU synchronization can affect the identification of MU characteristics. For these reasons both contraction level and degree of MU synchronization were regarded as relevant parameters to test the proposed algorithms.

Comparison between MUAP amplitude distribution and identified MU twitching areas

The metrics described above can be applied to simulated conditions where the ground truth is known and the algorithm characterization can be based on the comparison between simulated and obtained parameters. In experimental conditions this is overtly not possible. Therefore, in order to use a metric that can be adopted in experimental conditions as well, we decided to compare the centroids of the MUAP amplitude distributions with the centroids of the corresponding identified MU territories, provided by the algorithm. Specifically, the mediolateral position of the centroid of the electrical activity (i.e. MUAP) was used as the ground truth of the mediolateral position of the MU in the muscle cross section. Since the muscle was cylindrical and fusiform, we expected a linear relationship between the mediolateral coordinates of the centroids [22], [23]. The centroids of the estimated MU territory were calculated as the weighted centroid of the estimated MU twitching area after the global thresholding (see sections 3.1.1 and 3.1.2 final paragraphs), thus considering the intensities of the pixels in the image (and not the binary maps). The centroids of the MUAP were calculated from the map of the root mean square values of all channels segmented at 70 % of the maximum value [24].

3.3 Simulation results

In this section, the results of the comparison between the two proposed algorithms are presented. Hereafter, the STA-based algorithm (section 3.1.1) is referred to as STA, while the stICA-based algorithm (section 3.1.2) is referred to as STICA. The algorithms were

tested over four contraction levels (i.e. increasing number of active MUs) and two synchronization levels (see section 3.2).

General performance

Figure 3.7a reports two examples of an individual MU territory estimation using STICA in two simulated conditions leading to opposite outcomes. The right image shows a poor identification during a 20% MVC contraction with 25% Synchronization (Precision = 0.12 and Recall = 0.35), while the left image shows a good identification of MU territory obtained during a simulated contraction at 2% MVC with 15% Synchronization. According to the criteria listed in section 3.2.2, the left MU was regarded as successfully identified, whereas the right MU was considered an incorrect identification.

Figure 3.7b shows the group results of the identification of all the simulated MUs for the different force (i.e. number of MUs) and synchronization levels. The comparison of the two techniques revealed that STICA (blue) was more accurate in identifying MU territories than STA (red) (Figure 3.7b). A two-way ANOVA statistical test revealed that, both approaches (factor "method") showed a significant effect of the contraction intensity and degree of MU synchronization (factor "central input") on the percentage of correct identifications with respect to the number of active MUs ($p < 0.05$, Bonferroni correction). Moreover, between 2% and 20% MVC, the percentage of accurate (i.e recall and precision

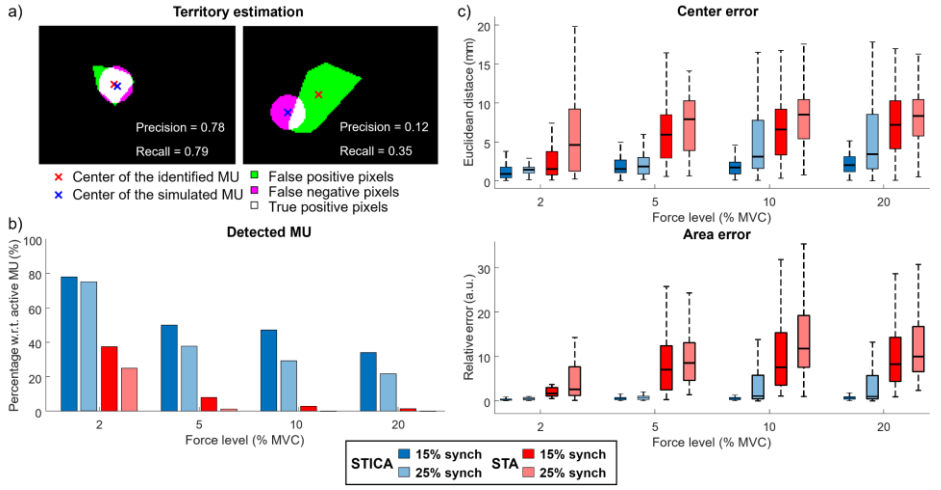

Figure 3.7 Simulation results. a) Two examples of MU territory estimates (white and green pixels) superimposed to the simulated ones (white and pink pixels). White areas include the correctly identified pixels (true positive), while pink and green areas denote the false negative and false positive pixels respectively. The crosses indicate the center of identified (red) and simulated (blue) MU terrirory. b) Percentage of the correctly identified MU territories w.r.t. the number of active MUs for the two methods (STICA and STA) applied to simulated contractions at different contraction and MU synchronization levels. c) Boxplots of center and area errors for methods, contractions and synchronization levels.

< 0.4) MU identification declined less for STICA (78% - 34% of the active MUs) than for STA (37% - 1%). Similar outcomes were observed for the comparisons at various MU synchronization levels. While STICA saw a 3% drop in correct recognition at 2% MVC and a 13% drop at 20% MVC, STA failed (i.e., 0% of MU was recognized) at 10% and 20% MVC.

This outcome was caused by the increased number of sources (MUs) activated for higher contraction levels and the decreased independence between their activation instants due to the increased degree of synchronization. Both these elements suggest a limited application of these techniques for high contraction levels and are well-known issues that limit the ability of STA and STICA to identify the constituent parts of the global signal.

Identification of the MU twitching area (territory)

Figure 3.7c shows the group results concerning the quality of the MU identification in terms of errors of center and area estimations. Both the contraction level and degree of synchronization degraded the performance of MU territory identification in terms of estimation errors (Figure 3.7c) and, consequently, the percentages of correct identification (Figure 3.7b). Indeed, Figure 3.7c displays the errors in the centers (top panels) and areas (bottom panels) of the estimations of the MU territory identified through STICA (blue) and STA (red) for the contraction and synchronization levels taken into consideration. A statistically significant difference with respect to the STA approach ($p < 0,05$, two-way ANOVA test on both variables of error with Bonferroni correction whenever a significant, additive effect was found) demonstrates that the STICA approach provided estimations with lower errors for both MU territory centers and areas, for all tested conditions. Moreover, center and area errors increased to a larger extent with contraction and synchronization levels for STA than STICA . This result suggests that STICA estimations are less affected than STA by the rising number of active MUs, which explains the higher proportion of accurate identification.

Overall, our findings demonstrated that STICA gives a more reliable assessment of the MU territory than STA, however, it is crucial to remember that potential non-linearities affecting experimental signals (i.e. the TVS) could reduce the performance indicated [25]. This concept will be expanded in the following Chapters related to experimental data.

Temporal analysis

Although we demonstrated that STA allows to correctly identify the simulated MU in few cases, STICA outperformed STA in identifying the location of MU territories at different contraction and synchronization levels. For this reason, the temporal comparison of the identified velocity twitch profile was conducted only on the STICA results related to the lower synchronization level (15%).

The zero-lag correlation coefficients between the estimated and simulated (Figure 3.6c) velocity profiles (twitch) for various contraction levels are shown in Figure 3.8. The simulated and reconstructed velocity profiles showed strong agreement, with a median correlation coefficient throughout contraction levels of 0.85. Although the distribution ranges widened at higher contraction levels, we did not observe a statistically significant effect on the contraction level ($p = 0.5$, $F = 0.83$, one-way ANOVA).

Comparison between MUAP amplitude distribution and identified MU twitching areas

The results of the agreement between the MUAP (electrical response) and MU twitching area (anatomical and mechanical response) of three example MUs are shown in Figure 3.9. The top panel of the figure shows the single differential MUAPs computed longitudinally, i.e. along the direction of the simulated fibers, while the middle and bottom panels show the corresponding spatial representation on the simulated TVS images (MU twitching area) and the estimated velocity profiles (twitch) based on the averaging with the MU firing pattern. The middle panel's insets are an extended image that is concentrated on the simulated MU territory (dashed black line) and the identified centroid (represented by a blue cross). The MUAP centroid (red cross in the upper panel), shares a medio-lateral location with the identified area (whose centroid is located in the simulated territory). When group data were considered (Figure 3.10), there was a strong positive correlation between

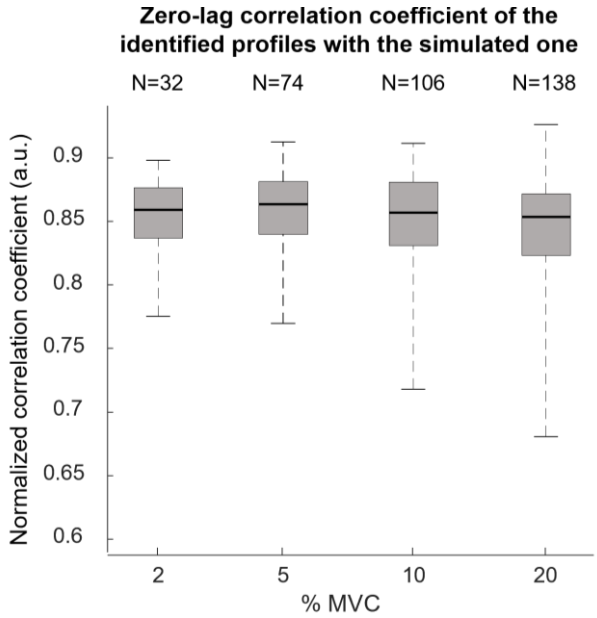

Figure 3.8 Temporal analysis results. a) Boxplots of the zero-lag correlation coefficient of the identified profile with the simulated velocity profile over different simulated contractions.

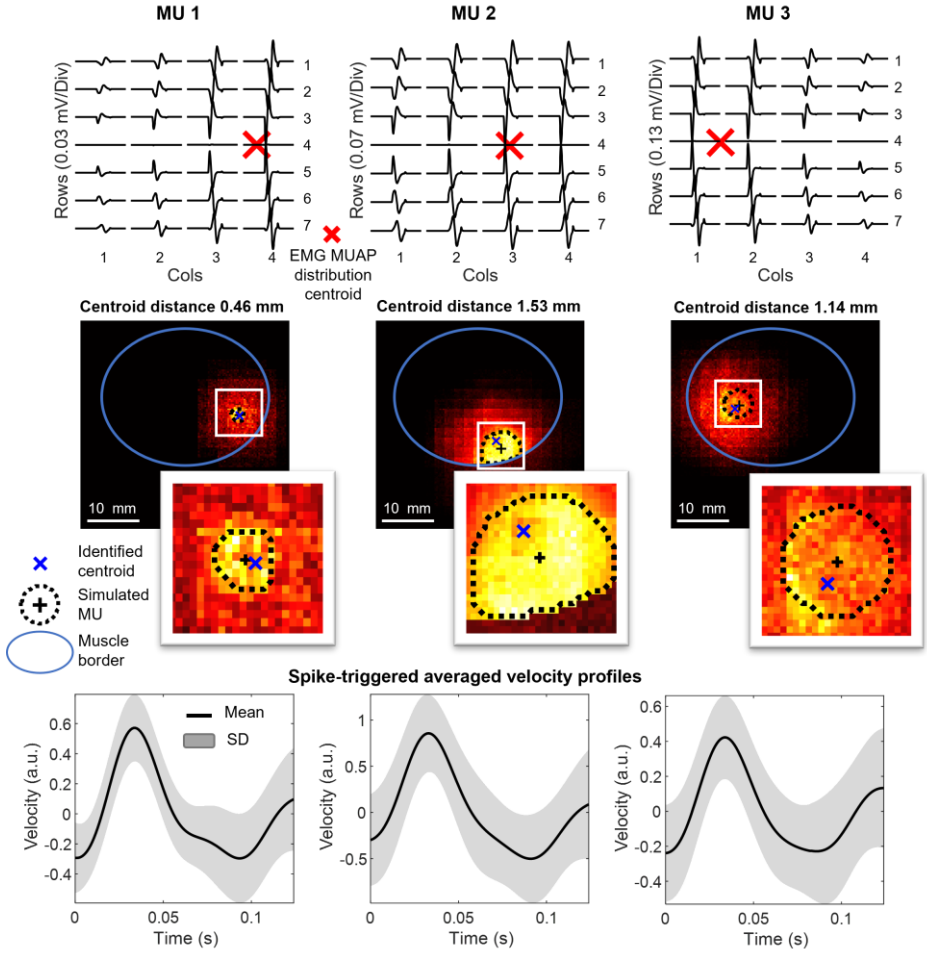

Figure 3.9 Examples of detected MU with STICA. Three representative outputs of the algorithm on simulated MUs. From top to bottom: longitudinal differential MUAP decomposed from EMG with the correspondent centroid (red cross); MU spatial representation in US images identified by the algorithm; a zoom of the simulated MU territory (MU center '+' and contour in black dotted line) and the centroid of identified region (blue cross); mean (black solid line) and the standard deviation (grey band) of the spike-triggered averaged velocity profiles related to the correspondent identified region of tissue displacement.

the mediolateral coordinates of the MUAP centroid of every MU and the mediolateral coordinates of the identified centroids in the simulated image sequences ($R^2 = 0.92$, $p < 0.05$). In other words, we observed a significant association in the mediolateral direction between the skin regions where MU action potentials with greatest amplitude were detected in the electrode array and the muscle regions where MU mechanical responses were represented in US images. Furthermore, regardless the contraction level and therefore the size of simulated units, our STICA approach was able to locate the center of the territory of

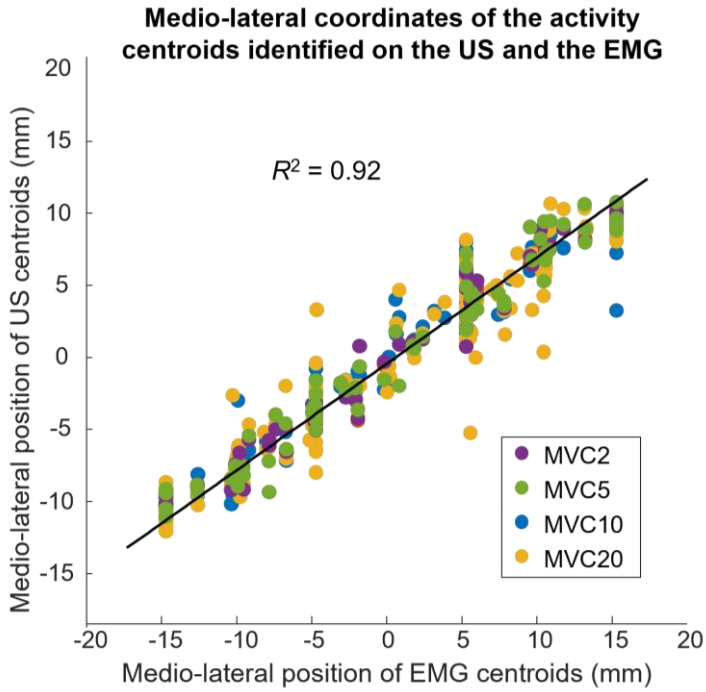

Figure 3.10 Medio-lateral US-EMG coordinates correlation. Scatterplot of the relation between the medio-lateral coordinates of the MUAP centroids and the US centroids

simulated MUs with an accuracy greater than 2 mm (in the case of the lowest synchronization level, Figure 3.7c). Therefore, our theoretical approach supports the idea that anatomical information on single MUs can be inferred from HDsEMGs for the set of conditions simulated in our model. This association would also be used on experimental data to demonstrate the quality of the possible identification of MU.

3.4 Conclusions of the simulation study

In this study, the tissue velocity sequences of muscle cross-sectional images were used to evaluate two techniques (STA and STICA) to identify and physically characterize MU. We demonstrated that STICA performed better than STA in locating the MU regions at various levels of contraction and synchronization. In general, our findings offer quantifiable proof that the two suggested methods are appropriate for anatomically and mechanically characterizing single MUs by using a combined HDsEMG and ultrafast US approach. Although STA is computationally more efficient and it may be suitable under certain conditions, such as long-duration recordings and few active MUs (i.e. very low contraction level), we selected the approach based on the decomposition of the tissue velocity

sequences (STICA) for the experimental identification of MU with a combined HDsEMG and ultrafast ultrasound approach.

3.5 References

[1] E. Lubel, B. Grandi Sgambato, D. Y. Barsakcioglu, J. Ibáñez, M. X. Tang, and D. Farina, 'Kinematics of individual muscle units in natural contractions measured in vivo using ultrafast ultrasound', *J. Neural Eng.*, vol. 19, no. 5, 2022, doi: 10.1088/1741-2552/ac8c6c.

[2] C. Cescon, M. Gazzoni, M. Gobbo, C. Orizio, and D. Farina, 'Non-invasive assessment of single motor unit mechanomyographic response and twitch force by spike-triggered averaging', *Med. Biol. Eng. Comput.*, vol. 42, no. 4, pp. 496–501, 2004, doi: 10.1007/BF02350990.

[3] J. V. Stone, J. Porrill, N. R. Porter, and I. D. Wilkinson, 'Spatiotemporal independent component analysis of event-related fMRI data using skewed probability density functions', *NeuroImage*, vol. 15, no. 2, pp. 407–421, 2002, doi: 10.1006/nimg.2001.0986.

[4] R. Rohlen, E. Stalberg, K. H. Stoverud, J. Yu, and C. Gronlund, 'A Method for Identification of Mechanical Response of Motor Units in Skeletal Muscle Voluntary Contractions Using Ultrafast Ultrasound Imaging - Simulations and Experimental Tests', *IEEE Access*, vol. 8, pp. 50299–50311, 2020, doi: 10.1109/ACCESS.2020.2980053.

[5] R. Rohlén, E. Stålberg, and C. Grönlund, 'Identification of single motor units in skeletal muscle under low force isometric voluntary contractions using ultrafast ultrasound', *Sci. Rep.*, vol. 10, no. 1, pp. 1–11, 2020, doi: 10.1038/s41598-020-79863-1.

[6] R. Rohlén, R. Raikova, E. Stålberg, and C. Grönlund, 'Estimation of contractile parameters of successive twitches in unfused tetanic contractions of single motor units – A proof-of-concept study using ultrafast ultrasound imaging in vivo', *J. Electromyogr. Kinesiol.*, vol. 67, Dec. 2022, doi: 10.1016/j.jelekin.2022.102705.

[7] T. Deffieux, J. L. Gennisson, M. Tanter, and M. Fink, 'Assessment of the mechanical properties of the musculoskeletal system using 2-D and 3-D very high frame rate ultrasound', *IEEE Trans. Ultrason. Ferroelectr. Freq. Control*, vol. 55, no. 10, pp. 2177–2190, 2008, doi: 10.1109/TUFFC.917.

[8] A. Holobar and D. Zazula, 'Correlation-based decomposition of surface electromyograms at low contraction forces', *Med. Biol. Eng. Comput.*, vol. 42, no. 4, 2004, doi: 10.1007/BF02350989.

[9] J. Duchateau and R. M. Enoka, 'Distribution of motor unit properties across human muscles', *J. Appl. Physiol.*, vol. 132, no. 1, pp. 1–13, Jan. 2022, doi: 10.1152/japplphysiol.00290.2021.

[10] A. V. Dieterich *et al.*, 'Spatial variation and inconsistency between estimates of onset of muscle activation from EMG and ultrasound', *Sci. Rep.*, vol. 7, no. February, pp. 1–11, 2017, doi: 10.1038/srep42011.

[11] F. Hug, T. Gallot, S. Catheline, and A. Nordez, 'Electromechanical delay in biceps brachii assessed by ultrafast ultrasonography', *Muscle Nerve*, vol. 43, no. 3, pp. 441–443, 2011, doi: 10.1002/mus.21948.

[12] A. Nordez, T. Gallot, S. Catheline, A. Guével, C. Cornu, and F. Hug, 'Electromechanical delay revisited using very high frame rate ultrasound', *J. Appl. Physiol.*, vol. 106, no. 6, pp. 1970–1975, 2009, doi: 10.1152/japplphysiol.00221.2009.

[13] D. Farina, L. Mesin, S. Martina, and R. Merletti, 'A Surface EMG Generation Model with Multilayer Cylindrical Description of the Volume Conductor', *IEEE Trans. Biomed. Eng.*, vol. 51, no. 3, 2004, doi: 10.1109/TBME.2003.820998.

[14] D. Farina and R. Merletti, 'A novel approach for precise simulation of the EMG signal detected by surface electrodes', *IEEE Trans. Biomed. Eng.*, vol. 48, no. 6, pp. 637–646, 2001, doi: 10.1109/10.923782.

[15] C. S. Klein, G. D. Marsh, R. J. Petrella, and C. L. Rice, 'Muscle fiber number in the biceps brachii muscle of young and old men', *Muscle Nerve*, vol. 28, pp. 62–68, 2003.

[16] A. J. Fuglevand, D. A. Winter, and A. E. Patla, 'Models of recruitment and rate coding organization in motor-unit pools', *J. Neurophysiol.*, vol. 70, no. 6, pp. 2470–2488, 1993, doi: 10.1152/jn.1993.70.6.2470.

[17] W. Yao, A. J. Fuglevand, and R. M. Enoka, 'Motor-unit synchronization increases EMG amplitude and decreases force steadiness of simulated contractions', *J. Neurophysiol.*, vol. 83, no. 1, pp. 441–452, 2000, doi: 10.1152/jn.2000.83.1.441.

[18] D. Farina, L. Fattorini, F. Felici, and G. Filligoi, 'Nonlinear surface EMG analysis to detect changes of motor unit conduction velocity and synchronization', *J. Appl. Physiol.*, vol. 93, no. 5, pp. 1753–1763, 2002, doi: 10.1152/japplphysiol.00314.2002.

[19] H. Maas, 'Significance of epimuscular myofascial force transmission under passive muscle conditions', *J. Appl. Physiol.*, vol. 126, no. 5, pp. 1465–1473, 2019, doi: 10.1152/japplphysiol.00631.2018.

[20] Y. Yoshitake, M. Shinohara, H. Ue, and T. Moritani, 'Characteristics of surface mechanomyogram are dependent on development of fusion of motor units in humans', *J. Appl. Physiol.*, vol. 93, no. 5, pp. 1744–1752, Nov. 2002, doi: 10.1152/japplphysiol.00008.2002.

[21] A. A. Taha and A. Hanbury, 'Metrics for evaluating 3D medical image segmentation: Analysis, selection, and tool', *BMC Med. Imaging*, vol. 15, no. 1, 2015, doi: 10.1186/s12880-015-0068-x.

[22] T. M. Vieira and A. Botter, 'The Accurate Assessment of Muscle Excitation Requires the Detection of Multiple Surface Electromyograms', *Exerc. Sport Sci. Rev.*, vol. 49, no. 1, 2021, doi: 10.1249/JES.0000000000000240.

[23] K. Roeleveld, D. F. Stegeman, H. M. Vingerhoets, and A. Van Oosterom, 'The motor unit potential distribution over the skin surface and its use in estimating the motor unit location', *Acta Physiol Scand*, vol. 161, pp. 465–472, 1997.

[24] A. Botter and T. M. Vieira, 'Optimization of surface electrodes location for H-reflex recordings in soleus muscle', *J. Electromyogr. Kinesiol.*, vol. 34, pp. 14–23, 2017, doi: 10.1016/j.jelekin.2017.03.003.

[25] E. Lubel *et al.*, ‘Non-linearity in motor unit velocity twitch dynamics: Implications for ultrafast ultrasound source separation’. bioRxiv, p. 2023.03.24.533983, Mar. 25, 2023. doi: 10.1101/2023.03.24.533983.

Chapter 4

Topic 2

4.1 In vivo testing of the HDsEMG and ultrafast US integration for single MU characterization

In the previous Chapter, we used simulated conditions to show that an approach combining HDsEMG and ultrafast ultrasound data processing has the potential to provide information about electrical (i.e. MUAP), neural (firing pattern), physical (location and dimension of the anatomic territory), and mechanical (velocity twitch) characteristics of MU. Two algorithms were tested on a cylindrical model of the muscle that was adapted to integrate a mechanical model of single MUs. The simulations provided HDsEMG signals and firing patterns of different contractions together with the cross-sectional tissue velocity sequences of the muscle. Our findings showed that the combined processing of HDsEMG and ultrafast ultrasound based on the decomposition of both signals and on the temporal correlations between electrical and mechanical components (STICA approach) outperformed the approach based on the simple averaging of the tissue velocity based on the single MU firings. Although simulations are necessary to quantify the algorithms output when the MU characteristics are known (input of the simulation model), they rely on several assumptions that limit the generalization of the results to experimental conditions. For instance, the presence of non-active tissue components (connective tissue) and the complex and non-linear tissue interactions between active and passive tissues are not taken into account. All these factors are likely to worsen the outcomes of proposed algorithms when tested with real signals. To evaluate the potential and limitations of the method, it is therefore crucial to conduct an experimental assessment.

In this Chapter, the STICA approach was applied to experimental signals to assess the local relationship between the action potentials of single MUs in surface EMGs and the corresponding mechanical activations in ultrasound images. The regional relationship between the surface action potential distribution and the location of MU fibers in the muscle cross section was previously described in literature [1]–[7]. In fact, the activation of a single motoneuron was shown to result in the excitation and subsequent movement of fibers regionally clustered within the muscle [8]. It is therefore reasonable to hypothesize a substantial correlation between the position in the EMG amplitude distribution and the location of tissue movement in ultrasound images. In this study, this association was used as a quality measure of the identification of MU fibers' location in the muscle cross-section.

4.2 Methods

4.2.1 Algorithm

The approach for the assessment of the spatial association between individual MUAPs and the corresponding representation in US images (STICA) was reported in the previous Chapter. The algorithm is based on the combined analysis of HDsEMG and 2D tissue velocity sequences (TVS). In simulated conditions, we analyzed the simulated firing pattern of the pool of active MUs and the simulated TVS to identify the territory of the simulated MUs. In the experimental data, we added the decomposition of the HDsEMG [9], [10] signals to obtain firing instants of the MUs, and we estimated the TVS from ultrafast US images of the muscle cross-section [11].

In the following paragraphs, after a description of the experimental procedure (Figure 4.2) for measuring the contractions of the biceps brachii (BB) muscle, we present the simultaneous acquisition of HDsEMG signals and ultrafast ultrasound images (Figure 4.1) and the processing pipeline, including the additional processing steps with respect to the simulations (Figure 4.3). We selected the biceps brachii because of its quasi-cylindrical shape, with fibers running parallel to the skin, similar to the simulated conditions.

4.2.2 Experimental protocol

Ten participants (mean ± SD, 29.2 ± 4.6 years, body mass index 23.0 ± 3.0 m/kg2, 6 males, 4 females) with no history of neurological or musculoskeletal impairments or disease were enrolled in the protocol. The study was conducted in accordance with the Declaration of Helsinki. Informed consent was obtained from all participants after receiving detailed explanation of the study procedures.

Procedure

To measure the torque at the elbow joint, the participant's right arm was placed inside an isometric brace with the elbow flexed at 135° (180° corresponded to complete elbow extension; Figure 4.1). The participant completed three MVCs (over a period of 5 s and each separated by 2 min of rest) at the start of each experiment while receiving verbal encouragement and visual input of the torque level. The maximum torque expressed during the three contractions was used as the reference value for the MVC. Five minutes of rest were provided after the MVC measurement. Three 60-second isometric elbow flexions at 2%, 5%, and 10% of MVC were performed by the participant after the placement of HDsEMG electrodes and positioning of the US probe over the muscular belly of the BB. While US images were acquired for approximately 8 s in the middle of the contraction, HDsEMG signals were recorded throughout the entire duration (Figure 4.2). To synchronize EMG-US acquisitions, an external rectangular pulse (StimTrig; LISiN, Politecnico di Torino, Italy) was used to initiate US acquisition and was concurrently captured by the HDsEMG system [12] (Figure 4.2).

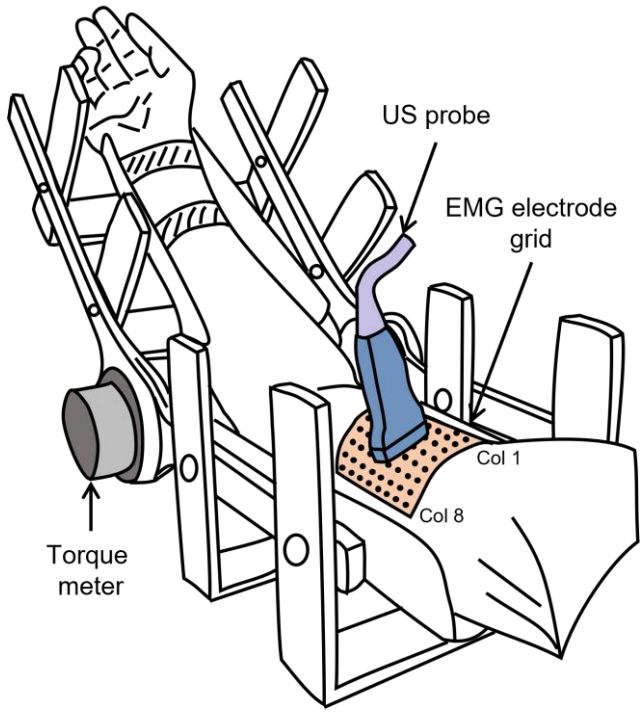

Figure 4.1 Experimental setup overview. The right arm was positioned inside an isometric brace for torque measurements. A grid of 64 EMG electrodes (8 × 8, 1 cm inter-electrode distance) was placed over the biceps brachii. The US probe was positioned between the two central rows of the electrode grid.

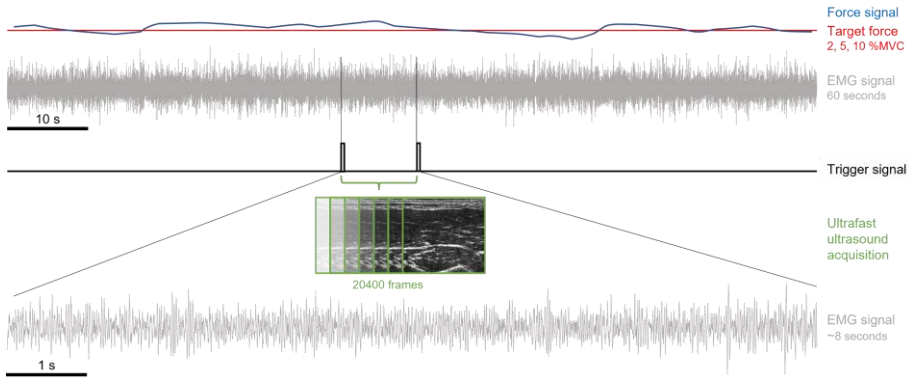

Figure 4.2 Experimental procedure. 60-second isometric elbow flexions at 2%, 5%, and 10% of MVC. HDsEMG signals were recorded throughout the entire duration while US images were acquired for approximately 8 s in the middle of the contraction. An external trigger signal was used to control the US acquisition and was concurrently recorded by the HDsEMG system. For the sake of simplicity, a single EMG channel was shown.

HDsEMG recordings

A grid of electrodes that allows for the simultaneous recording of EMG and US from the same muscle region (modified from Botter et al. [13]) was used to capture muscle activity. Following proper skin preparation [14], the grid of 64 electrodes (8 rows by 8 columns, 10 mm inter-electrode distance) was placed on the BB muscle belly with the columns aligned with the longitudinal axis of the arm and the space between the fourth and fifth row in correspondence to the main muscle innervation zone, previously identified with an array of dry electrodes [15]. Prior to the electrode positioning, ultrasound imaging was used to determine the separation between the two BB heads [16]. The grid's first four columns were put on BB's short head, while the last four were put on its long head (Figure 4.1). Monopolar EMG signals were detected, conditioned (Bandwidth 10-500 Hz, Gain 46 dB), and sampled at 2048 Hz with 16-bit resolution through a wireless HDsEMG acquisition system [17] (MEACS, LISiN, Politecnico di Torino, Turin, Italy). In order to ensure synchronization with ultrasound detection, a wireless synchronization system was used [12].

Ultrasound acquisition

Verasonics Vantage 128 (Verasonics, Inc., Kirkland, WA) programmable ultrasound research platform, and Verasonics L11-5v linear array transducer (7.8125 MHz center frequency) were used to collect radiofrequency (RF) data. The US probe was securely held above the BB muscle and perpendicular to the longitudinal axis of the arm using a probe holder that was fastened to the isometric brace. The two heads of the BB were scanned in the medio-lateral direction (cross-sectional) [18] by positioning the probe between the fourth and fifth row of electrodes and centered with respect to the columns (Figure 3.5).

This position corresponded to the main innervation zone as previously identified in which the main movements of the activated MUs should be visible with the minor delay with respect to the electrical activity. An original MATLAB (MathWorks, Natick, MA) code was utilized to capture plane wave data at a frame rate of 2500 fps while controlling the RF acquisition using an external initiating trigger (Figure 4.2). The RF data was captured at a frequency that was four times the transducer center frequency (31.25 MHz), and it was rebuilt using the common delay-and-sum (DAS) beamforming [19] technique in post-processing.

4.2.3 Data processing

HDsEMG processing and decomposition

HDsEMG signals (Figure 4.3a) were bandpass filtered in the 20–400 Hz range (4-order Butterworth filter), and when necessary, residual power line interference was eliminated [20]. Signals were then decomposed (Figure 4.3b) into individual MU firing patterns using a validated [21], [22] convolution kernel compensation (CKC) approach [9], [23], [24]. The firing pattern was resampled at the same sampling rate as the US images (2500 Hz) for further processing.

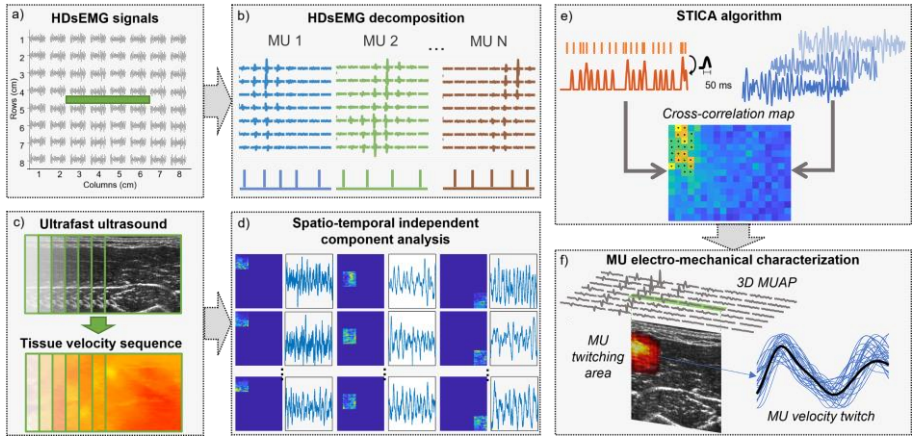

Figure 4.3 Processing of HDsEMG and UUS data. a) Monopolar HDsEMG signals of the 64 electrodes positioned over the biceps brachii. The US probe location was center with respect to the columns and rows (green rectangle). b) Decomposition of HDsEMG giving a number of MU and corresponding firing instants. c) The ultrafast ultrasound (UUS) data are processed to compute the tissue velocity sequence using the 2D autocorrelation method. d) Decomposition of tissue velocities through spatio-temporal independent component analysis. e) STICA approach integrating the analysis of the two decomposition of HDsEMG and UUS with a cross-correlation step between convoluted firings and temporal components (for further details refer to the previous Chapter). f) Example outcome of the algorithm showing the complete electro-mechanical MU characterization with the motor unit action potential, the identified MU twitching area, and the velocity profile of the twitch.

Tissue velocity sequence computation

The analysis of the TVS of muscle cross-section enables the quantification of the deep-superficial movements of bundles of contracting fibers [18], [25]–[27]. Using RF signals and autocorrelation in the time (pulse transmissions) and space (depth samples) dimensions, we calculated the TVS along the ultrasound beam axis [11] (Figure 4.3c). Based on earlier research, we chose a sliding window of 10 ms and a maximum displacement of 1 mm between successive images [25]. After obtaining the velocity data for each frame (time) and pixel (space) in the image, velocity profiles in space and time were filtered. The contribution of isolated pixels with incorrect values was reduced by applying a spatial 2-D median filter (1 × 1 mm kernel) to each frame. Then, to reduce slow motions unrelated to muscular contraction, the temporal development of each pixel was high-pass filtered at 5 Hz (4^{th}-order Butterworth filter). After being axially downscaled from the original data, we obtained 125 × 125 pixels with a final spatial resolution around 0.3 × 0.3 mm (field of view of 40 × 40 mm). Following that, the filtered TVS was processed by sliding a ROI [28] in accordance with the description reported in the previous Chapter using the spatio-temporal independent component analysis (Figure 4.3d).

STICA algorithm for electro-mechanical MU characterization

All the details of the combined analysis of the two decompositions of HDsEMG and UUS (Figure 4.3e, STICA algorithm) are reported in the previous Chapter. The algorithm returns, for each MU decomposed from HDsEMG, the corresponding identified MU twitching area (*MU spatial representation* in UUS images) and the twitch velocity profile (Figure 4.3f). These information together constitute the electro-mechanical MU characterization.

4.2.4 Association between electrical and mechanical activity

We compared the centroids of the MUAP amplitude distributions calculated from the single differential HDsEMG signals [29] with the centroids of the corresponding MU spatial representations in the UUS images provided by the algorithm (i.e. what we refered also as *MU twitching area*).

A multiple regression analysis ($Y_{fit} = \beta_1 + \beta_2 x_1 + \beta_3 x_2 + \beta_4 x_1 x_2$) on the experimental data was implemented to assess the relationship between the medio-lateral coordinates of the US centroids (dependent variable Y) with the mediolateral position of the EMG centroids and the depth of the identified centroids in the US image (independent variables x_1 and x_2, respectively). We also added an interaction term to check whether there was a significant effect of the depth of identification on the mediolateral EMG-US relation [30]. We assumed no collinearity between the independent variables since they were derived from different measurement modalities. Statistical significance was assessed

based on 95% confidence intervals of the model coefficients. All the statistical tests were performed in MATLAB (R2020b, The MathWorks Inc., MA, USA).

4.3 Experimental results

4.3.1 General comments

None of the volunteers experienced any discomfort or fatigue while completing the protocol. After eliminating MUs with fewer than 20 firings in the US acquisition time interval, those with a coefficient of variation of the inter-spike interval greater than 30%, and MUs whose action potentials were of dubious nature, a total of 180 MUs were analyzed (mean SD, 18 ± 8 MUs per participant, average firing rate: 11.3 ± 2.1 pps).

4.3.2 Association between electrical and mechanical activity

Examples of three MUs that were decomposed from a 2% MVC contraction in an examined participant are shown in Figure 4.4. The three MUs were depicted in the surface

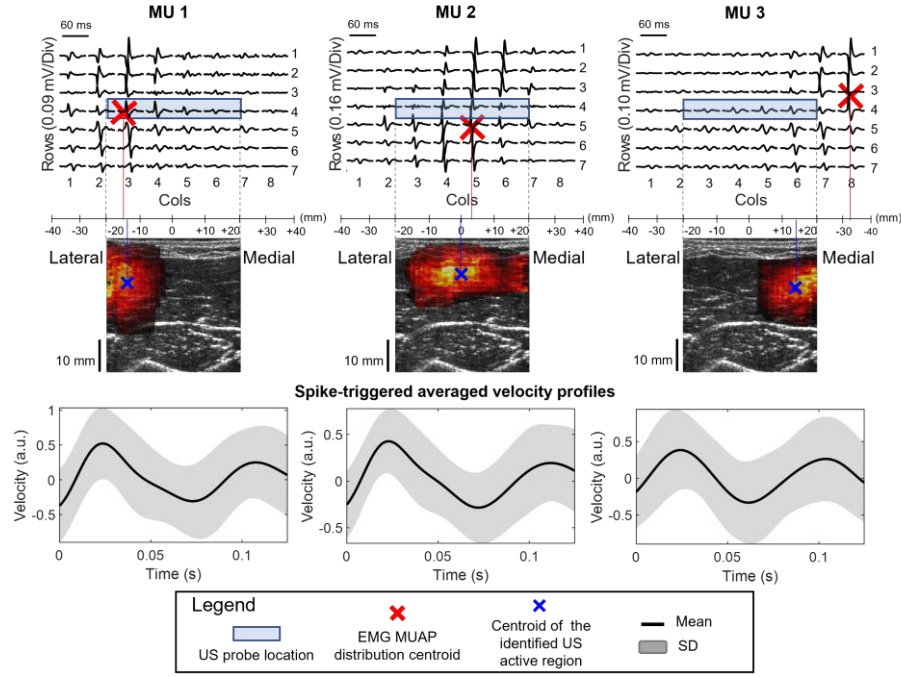

Figure 4.4 ***In vivo*** **identified MU.** Example of three MUs from biceps brachii during a 2% isometric contraction in one representative subject. From top to bottom: MUAPs decomposed from HDsEMG with the correspondent centroids (red crosses); identified MU spatial representation overlapped on the B-mode images of BB with correspondent centroids (blue crosses); means (black solid line) and the standard deviation (grey band) of the spike-triggered averaged velocity profiles related to the correspondent identified areas.

EMGs in three different ways: MUs #1, #2, and #3 were linked to action potentials that were distributed laterally, centrally, and medially, respectively, in the electrode array (Figure 4.4, top panel). In the longitudinal direction, the centroids of the detected MUAPs were grouped around row 4 (80% of all MUs between row 3 and 5), where the US probe was positioned. However, in the transverse muscle direction, they dispersed evenly across the columns. The analysis of US images with identified MU area overlay (i.e., heatmaps in Figure 4.4, middle panels) showed a distinct spatial relationship in the mediolateral direction between the EMG and US identification of the three MUs. The spike-triggered averaged velocity profiles related to the corresponding identified areas are depicted in the bottom panels of Figure 4.4.

Multiple regression analysis showed a significant correlation between the mediolateral location of centroids in EMG and US (Figure 4.5a, $R^2 = 0.20$ and $p < 0.05$). The linear coefficient (β_2) that connects the medio-lateral coordinates of EMG centroids to US centroids had a confidence interval that varied from 0.39 to 0.82 ($p < 0.05$). The range of the confidence interval for the US area's coefficient of depth related to its mediolateral position (β_3) was -0.16 - 0.176 ($p = 0.94$). The coefficient of depth between the EMG centroids (β_4) had a confidence interval of 0.01 - 0.03 mm^{-1} ($p < 0.05$). The relationship between US and EMG identification in the mediolateral direction was more linear for the more superficial MU identifications, as seen in Figure 4.5b. The variance explained by the model was 53% for depths less than 14 mm ($N = 60$, $p < 0.05$), 5% for depths between 14 and 23 mm ($N = 59$, $p = 0.09$), and 1% for depths > 23 mm ($N = 61$, $p = 0.6$).

4.4 Discussion of the experimental analysis

In this study, we developed an algorithm to identify the spatial and physical characteristics of individual motor units in vivo. This approach was used to investigate the relationship between the spatial representation of individual MUs in surface EMGs and US images. We were able to detect the electrical and mechanical responses of 180 MUs during isometric, constant-force contractions by combining HDsEMG decomposition with spatiotemporal decomposition of the ultrasound tissue velocity sequences. According to our findings, both US and EMG include spatially localized regions that show single MU activation.

4.4.1 HDsEMG decomposition as gold standard

The approach used in this study relies on the identification of the precise moment each individual MU fires, which is then used to extract electrical (in EMG signals) and physical (in US images) representations of each MU's activation. It is worth noting that this approach performs an actual integration between HDsEMG and US signal processing. Indeed, an alternative option could consist in applying separately HDsEMG [24] and UUS

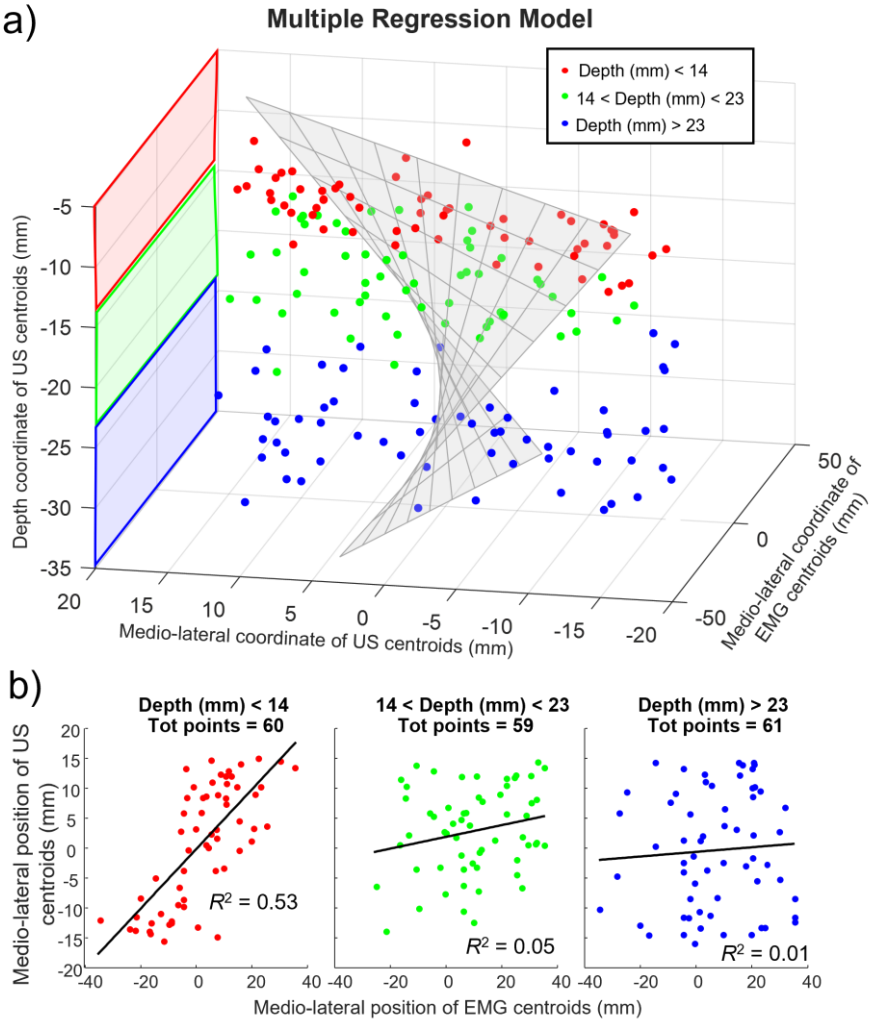

Figure 4.5 Group results of experimental data. (a) 3D scatterplot of the relationship between the medio-lateral coordinates of centroids in EMG and US identified area, considering the effect of the depth in US. The surface represents the best fit of the multiple regression model. (b) Scatterplots of the MU divided by the US identification depth. From left to right: depth < 14 mm (N = 60), depth > 14 mm and < 23 mm (N = 59), depth > 23 mm (N = 61).

decomposition [25] and to retrospectively correlate pairs of single MUs *independently* identified by the two approaches. In this regard, the agreement between MU firing instants obtained by two decomposition methods (e.g., needle and HDsEMG) has previously been used [21], [22]. However, in our case, the relatively high number of mismatches in MU identification between the two methods [28], [31] seem to limit the applicability of this approach (i.e. agreement between firing instants). It was therefore decided to first identify

MU firing instants of single MUs through HDsEMG decomposition [23], [32] and then to process the UUS data using MU firings as input information. We decided to identify MU firings with HDsEMG decomposition (instead of US images decomposition [8], [31]) for two reasons. First, although both techniques have been validated, HDsEMG decomposition has been more extensively validated and used in several experimental conditions [10], [21], [32]–[34], [34]. Second, compared to the decomposition of tissue velocity sequences, the decomposition of HDsEMG has a stronger overall discriminative capability. Indeed, despite having similar high temporal and spatial resolutions, monopolar HDsEMG and ultrafast US imaging detect physiological events with very different time scales. Single action potentials in surface EMGs last less than 30 ms (Figure 4.4), whereas tissue displacements produced by a single MU firing last around 10 times longer [26]. Therefore, surface EMGs are more likely to resolve the superposition of various MUs than ultrasound images because action potentials have shorter durations than tissue displacement. Collectively, these considerations led us to choose in favour of HDsEMG decomposition to provide the initial set of MUs that were used as input to the proposed algorithm.

4.4.2 Comparison with simulation results and limitations

The results of our experiment match with those of the simulated data. In particular, there was a substantial correlation between the mediolateral coordinate of the identified US region and that of the associated MUAP distribution (Figure 4.5a). As expected, the depth of the MU's area in the US images (depth coordinate of ‘x’ in Figure 4.4) had an impact on the strength of this link. In this study we attempted to identify as many MUs as we could by decomposing monopolar EMGs, indiscriminately including superficial and deep units [35]. However, we were able to demonstrate the expected correlation between EMG and US MU representation more clearly by grouping units according to their depth representation in the US images. In fact, the coefficient of determination for MUs with tissue displacements centered deeper than 14 mm was at least twenty times lower than that for MUs with superficial tissue displacements (Figure 4.5b). This is most likely due to the diffusion of the potentials caused by the interposed tissues, which leads to a more uniform distribution of the amplitude of the potentials over the surface EMGs of the deep MUs [29]. Therefore, mediolateral distributions of surface EMGs generated by deep MUs are similar for different MU transverse locations, limiting the discriminative power of EMG centroids. The observed difference between the positions of EMG- and US-based centroids of deep MUs may also be due to surface EMG, which may be biased towards contributions from the upper portion of deep MU territory due to a higher sensitivity to superficial sources [35]. Several reasons can explain the higher sensitivity of surface EMG to superficial sources. Firstly, the electrical signals generated by superficial muscle fibers have less tissue to travel through before reaching the surface electrodes, making them more readily detectable. Additionally, the volume of muscle tissue being sampled by surface EMG decreases with increasing depth, which may further reduce the representation of deep MUs [36], [37].

These factors limits the accurate assessment of deep muscle activity. The significant interaction between the depth coordinate of US image-derived centroids and the medio-lateral coordinate of EMG centroids (Figure 4.5a) provides support for these possible factors.

Despite the good spatial correlation for the superficial MUs, experimental results were not as clear as in simulated conditions. The causes of this might be related to how other factors, in addition to MU depth, affect how MU activation is represented in EMG and US. Inter-individual anatomical variation is the first important source to be mentioned. According to the size and shape of the surrounding tissue, and as schematically illustrated in Figure 4.6, for spatially localized MUs centered at equal depths, the distance between electrodes and the center of the MU territory varies [8]. This also affects the transverse representation of action potentials [38]. Variation is demonstrated in Figure 4.6 in terms of different sizes of the muscle cross-sectional area. However, it should be highlighted that any other anatomical source changing the distance between electrodes and MUs would similarly affect the unit representation in the surface EMG [8], [29], [30]. Any anatomical factor that modifies this distance can influence the recorded EMG signals and subsequently affect the representation of MUs. For example, the presence of subcutaneous tissue, such as connective tissue or fat layers between the electrodes and the muscle fibers, can influence the detection of EMG signals. Subcutaneous tissue can act as a low-pass filter, attenuating higher frequency components of the EMG signal and affecting the representation of MU activity. This problem impacts MUs of various levels, although it probably manifests itself more strongly in deeper units. Furthermore, the fixed inter-electrode distance of 10 mm used to compute bipolar EMGs may convey a different proportion of fibers of single MUs for various individuals: more superficial units were likely less locally represented in our bipolar EMGs for subjects with a thicker subcutaneous adipose tissue.

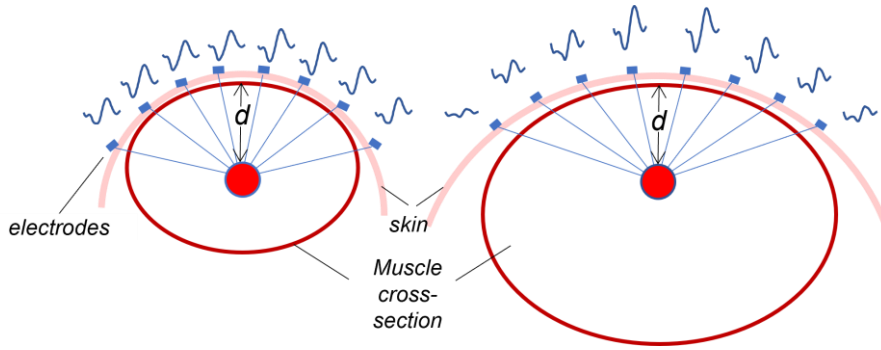

Figure 4.6 Effect of the muscle physiological cross-sectional area (PCSA) on the transversal MUAP amplitude distribution.. Red circles represent the territories of two MUs located at the same depth (d) in two muscles with different PCSA. Right muscle (small PCSA): the distance between active fibers and the skin surface is similar for all the skin locations, leading to a uniform MUAP amplitude distribution across the detecting electrodes. Left muscle (large PCSA): the distance between active fibers and the skin surface changes for different skin locations, leading to a more localized amplitude distribution.

Finally, an additional factor that should be considered is our limited knowledge of how well single MU contractions may be detected in UUS images as a second source of variation. The non-linear summation of mechanical responses plays a crucial role in this regard. The tissue velocities estimated from UUS sequence differed from the simulated ones in which a linear instantaneous superimposition model was adopted. This discrepancy might be related to complex interactions between the motions of the muscle units and their summation. For example, the contraction and relaxation of a group of fibers is known to exert force on the adjacent fibers and connective tissue, creating propagating waves within the muscle tissue [39]. Considering the great number of MUs involved even at low force level, the superimposition of all these complex dynamics might not be considered linear from the velocities perspective. All these factors are acknowledged in the literature and were used to explain the observed mismatches between electrical activity and mechanical responses identified separately [28], [31]. In our case this could have generated some wrong associations between MUAP and of MU tissue displacements affecting the degree of correlation between centroids. In this section we discussed several aspects that could affect the identification of single MUs from UUS images (considering also our EMG-driven approach), however our preliminary results suggested that, at least for superficial MUs, it is possible to obtain reliable identifications.

4.4.3 Generalization of this experimental result

The generalization of these findings to muscles and conditions other than those investigated here require careful considerations. Given that we assessed the component of the tissue velocity in the superficial-depth direction, the first aspect to consider is that the proposed approach requires the use of cross-sectional UUS images, i.e. detected on a plane perpendicular to the muscle fibers's direction in the muscle CSA. The tissue velocities extracted from cross-sectional images should theoretically capture the thickening of MU fiber and they are expected to be influenced by the location of the contracting fibers within the muscle CSA. It is necessary to conduct additional research to determine whether this interpretation is accurate for UUS images detected from a scanning plane not perpendicular to the fiber direction.

The fact that the identification of the mechanical response with our EMG-US approach can be generalized to MUs recruited at higher force levels is another intriguing and relevant issue. Both EMGs and tissue velocity sequences become more interferential at increasing contraction levels as a result of the progressive recruitment of more MUs and rise in firing rate, thus restricting the ability to distinguish between individual MUs. While this constraining problem is being addressed in surface EMG decomposition, further research is needed on the lower frequency tissue displacement velocities and the non-linear summation of mechanical responses (twitches) in US-based decomposition. We want to emphasize that technical constraints unrelated to the method we provided here limit the extent to which our

conclusions can be generalized. Results different to those reported here would be expected for other muscles and contraction levels.

4.5 Experimental comparison between STA and STICA approach

We have previously used an electromechanical computer model to test the capability of the two methods to correctly identify single MU twitching areas in simulated contractions with different degrees of neural excitation (i.e., the number of active MUs) and different levels of MU synchronisation (i.e., degree of dependency between firing instants of different MUs). The first method was based on the spike triggered averaging of the tissue velocities (STA), while the second one was based on the spatio-temporal decomposition of these (STICA). We showed that the performance of both approaches was negatively affected by the number of active MUs and synchronisation levels. However, STICA provided a more robust estimation of the MU displacement areas under all the tested conditions.

Although a thorough experimental examination was performed for the STICA approach, we wanted to further test whether the in silico results of STA and STICA comparison extend to the experimental conditions of isometric elbow flexions. Since the location of the MU fibers within the muscle cross-section is unknown in experimental data, we quantified the agreement between the HDsEMG amplitude distribution of the MUAP and the location of the corresponding MU twitching area identified by applying STA and STICA algorithm to UUS image sequences.

4.5.1 Methodological considerations

The above reported experimental results (section 4.3) highlighted a substantial correlation between the transverse coordinate of the center of the identified MU twitching area and the medio-lateral center of the electrode region where the largest amplitude single MU action potentials were found. The strongest correlation was found for superficial MUs. For this reason, in the following comparison of STA and STICA we elaborated the data considering the US images up to 20 mm depth (instead of the whole 40 mm).

The centroids of the MU twitching areas obtained from STA and STICA were computed (refer to the previous chapter for further details) and compared with the centroids of the amplitude distribution of the MUAP of the corresponding MU (i.e., the MU whose firings were used as input to STA and STICA algorithms). The comparison was performed by computing the *centroid-to-centroid* (EMG-ultrasound) *distance* in the medio-lateral direction. Moreover, the two algorithms were processed considering the entire 8 s of acquisition and only the first 2 s of acquisition to evaluate the effect of the signal duration on their performance. The effect of the factors “method” (STA and STICA) and “duration”

(2 s and 8 s) were tested with a 2-way ANOVA on the centroid-to-centroid distance. Post-hoc assessments were conducted using the Bonferroni test whenever a main effect was verified.

4.5.2 Results

Figure 4.7 shows the identification of the MU twitching areas of four representative MUs using the combined analysis of HDsEMG data and UUS images. The figure shows, in the top panel, the spatial distribution of single differential MUAPs, in the middle panel, and in the bottom panel, the US MU twitching area identified with STA and STICA, respectively. The spatial agreement between the MU twitching area and the EMG amplitude distribution varies in these four examples of Figure 4.7 between the two algorithms. The horizontal distance (*centroid-to-centroid distance)* between the symbols '+' in EMG, '◊' for STA, and '×' for STICA demonstrated that MU#1 had a strong spatial correspondence for both STA and STICA. While only one of the algorithms provided a good match for MU#2 and MU#3 (STA and STICA respectively), MU#4 displacement area identification appeared to be unsuccessful for both STA and STICA.

Figure 4.8 shows the centroid-to-centroid (EMG-ultrasound) distance in the medio-lateral direction (horizontal distance between the '+' in EMG with '◊' for STA and with '×' for STICA as shown in Figure 4.7) for all the 180 MUs for both approaches when 8 s and 2 s of signal duration are considered. First, STICA approach generally provided shorter distances for all the tested durations, as demonstrated by statistically significant differences

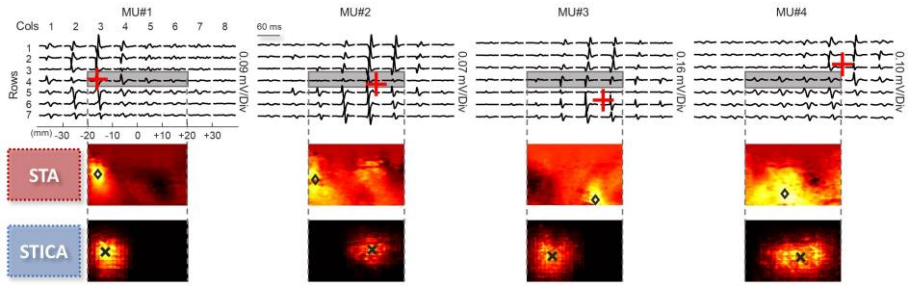

Figure 4.7 Comparison of MU identifications with STA and STICA. Four examples of MUs (column wise) decomposed from HDsEMG and the corresponding identified region of displacement (MU twitching area). First row: template of the motor unit action potential (MUAP) in single differential derivation along the rows of HDsEMG grid. Red + represents the centroid of the MUAP template distribution as calculated in [7]. The grey rectangle shows the region where the ultrasound probe was placed to scan the muscle cross-sectionally. Second row: images obtained with the spike triggered averaging (STA) approach representing the region of displacement of the corresponding MU. ◊ indicates the centroid of the tissue velocity image. Third row: final images of the approach based on the spatio-temporal independent component analysis (STICA) representing the region of displacement of the corresponding MU. × represents the centroid of the tissue velocity image. The figure shows from left to right: a well-detected MU (low centroid-to-centroid distance between EMG and ultrasound) for both approaches; a MU displacement area correctly identified only by STICA; a MU displacement area correctly identified only by the STA approach; a wrong MU displacement area identification for both STA and STICA.

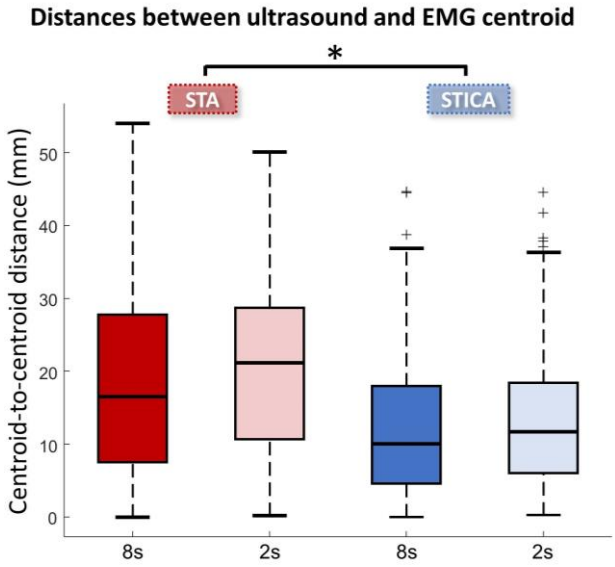

Figure 4.8 STA and STICA distances between ultrasound and EMG centroid. Boxplots of distances between EMG and ultrasound centroid for all the considered MUs for both STA (red) and STICA (blue) when considering 8 seconds (dark color) and 2 seconds (light color) duration of the acquisition. *p<0.001

with respect to STA ($p < 0.001$). Although not significant ($p = 0.054$), a trend associated with signal duration can be appreciated in both STA and STICA and to a larger extent for STA. The ranges of the distances obtained for STA (0 – 53 mm) and STICA (0 – 37 mm) confirmed the results seen in simulated conditions, with STICA providing shorter distances. However, as it might be predicted, these values are higher than those found in simulated settings, where both approaches consistently produced distances of less than 20 mm considering contractions of up to 20% MVC. As a result, even though we considered lower contraction levels (around 5% MVC), both approaches' performances significantly deteriorated under experimental conditions. This result can be explained by the fact that in the experimental analysis, our reference for the "true" medio-lateral location of the MU twitching area was the centroid of the MUAP distribution, which can be identified with a relatively low spatial resolution (inter-electrode distance). In addition, obvious differences between experimental and simulated conditions, e.g. the effect of connective tissue affecting the transversal force transmission between fascicles, may explain the differences. All these limiting factors affected the estimation error.

The length of the EMG and ultrasound time series was expected to have an impact on both approaches in terms of the effect of signal length. However, our findings suggest that STICA might offer more accurate MU displacement area estimates for short-duration recordings (light-colored boxes in Figure 4.8). Given the substantial amount of data involved in the elaboration of sequences of high-frame rate ultrasound images, this can

be a significant advantage. In addition, the ability to estimate displacement area accurately for brief signal epochs may make it possible to implement STICA-based algorithms that use the temporal segmentation of the detected signal to enhance estimation, such as by providing an index of the identified area's repeatability throughout contraction.

In conclusion, although wrong estimations occurred for both methods, the two proposed approaches are suitable for anatomical in vivo identification of individual MU using the combination of HDsEMG and UUS analysis with STICA providing more precise estimation of the location of the MU twitching region.

4.6 References

[1] J. W. Cohen, A. Gallina, T. D. Ivanova, T. Vieira, D. J. McAndrew, and S. J. Garland, 'Regional modulation of the ankle plantarflexor muscles associated with standing external perturbations across different directions', *Exp. Brain Res.*, vol. 238, no. 1, 2020, doi: 10.1007/s00221-019-05696-8.

[2] T. M. M. Vieira, I. D. Loram, S. Muceli, R. Merletti, and D. Farina, 'Postural activation of the human medial gastrocnemius muscle: Are the muscle units spatially localised?', *J. Physiol.*, vol. 589, no. 2, pp. 431–443, 2011, doi: 10.1113/jphysiol.2010.201806.

[3] K. Watanabe, M. Kouzaki, R. Merletti, M. Fujibayashi, and T. Moritani, 'Spatial EMG potential distribution pattern of vastus lateralis muscle during isometric knee extension in young and elderly men', *J. Electromyogr. Kinesiol.*, vol. 22, no. 1, pp. 74–79, 2012, doi: 10.1016/j.jelekin.2011.09.010.

[4] D. Farina, F. Leclerc, L. Arendt-Nielsen, O. Buttelli, and P. Madeleine, 'The change in spatial distribution of upper trapezius muscle activity is correlated to contraction duration', *J. Electromyogr. Kinesiol.*, vol. 18, no. 1, pp. 16–25, 2008, doi: 10.1016/j.jelekin.2006.08.005.

[5] A. V. Dieterich *et al.*, 'Spatial variation and inconsistency between estimates of onset of muscle activation from EMG and ultrasound', *Sci. Rep.*, vol. 7, no. February, pp. 1–11, 2017, doi: 10.1038/srep42011.

[6] J. Navallas, A. Malanda, L. Gila, J. Rodriguez, and I. Rodriguez, 'Comparative evaluation of motor unit architecture models', *Med. Biol. Eng. Comput.*, vol. 47, no. 11, pp. 1131–1142, Nov. 2009, doi: 10.1007/s11517-009-0526-0.

[7] Í. Corera, A. Malanda, J. Rodriguez-Falces, S. Porta, and J. Navallas, 'Motor unit profile: A new way to describe the scanning-EMG potential', *Biomed. Signal Process. Control*, vol. 34, pp. 64–73, Apr. 2017, doi: 10.1016/j.bspc.2016.12.020.

[8] T. M. Vieira and A. Botter, 'The Accurate Assessment of Muscle Excitation Requires the Detection of Multiple Surface Electromyograms', *Exerc. Sport Sci. Rev.*, vol. 49, no. 1, 2021, doi: 10.1249/JES.0000000000000240.

[9] A. Holobar and D. Zazula, 'Correlation-based decomposition of surface electromyograms at low contraction forces', *Med. Biol. Eng. Comput.*, vol. 42, no. 4, 2004, doi: 10.1007/BF02350989.

[10] F. Negro, S. Muceli, A. M. Castronovo, A. Holobar, and D. Farina, 'Multi-channel intramuscular and surface EMG decomposition by convolutive blind source

separation', *J. Neural Eng.*, vol. 13, no. 2, 2016, doi: 10.1088/1741-2560/13/2/026027.

[11] T. Loupas, R. W. Gill, and J. T. Powers, 'An Axial Velocity Estimator for Ultrasound Blood Flow Imaging, Based on a Full Evaluation of the Doppler Equation by Means of a Two-Dimensional Autocorrelation Approach', *IEEE Trans. Ultrason. Ferroelectr. Freq. Control*, vol. 42, no. 4, pp. 672–688, 1995, doi: 10.1109/58.393110.

[12] G. L. Cerone, A. Giangrande, M. Ghislieri, M. Gazzoni, H. Piitulainen, and A. Botter, 'Design and validation of a wireless Body Sensor Network for integrated EEG and HD-sEMG acquisitions', *IEEE Trans. Neural Syst. Rehabil. Eng.*, 2022, doi: 10.1109/TNSRE.2022.3140220.

[13] A. Botter, T. M. Vieira, I. D. Loram, R. Merletti, and E. F. Hodson-Tole, 'A novel system of electrodes transparent to ultrasound for simultaneous detection of myoelectric activity and B-mode ultrasound images of skeletal muscles', *J. Appl. Physiol.*, vol. 115, no. 8, pp. 1203–1214, 2013, doi: 10.1152/japplphysiol.00090.2013.

[14] R. Merletti and G. L. Cerone, 'Tutorial. Surface EMG detection, conditioning and pre-processing: Best practices', *J. Electromyogr. Kinesiol.*, vol. 54, 2020, doi: 10.1016/j.jelekin.2020.102440.

[15] R. MERLETTI, A. BOTTER, A. TROIANO, E. MERLO, and M. A. MINETTO, 'Technology and instrumentation for detection and conditioning of the surface electromyographic signal: state of the art.', *Clin. Biomech.*, vol. 24, pp. 122–134, 2009, doi: 10.1016/j.clinbiomech.2008.08.006.

[16] T. P. Pinto, A. Turolla, M. Gazzoni, M. Agostini, and T. Vieira, 'Assessing structural adaptation of biceps brachii motor units after stroke', *Gait Posture*, vol. 57, 2017, doi: 10.1016/j.gaitpost.2017.07.101.

[17] G. L. Cerone, A. Botter, and M. Gazzoni, 'A Modular, Smart, and Wearable System for High Density sEMG Detection', *IEEE Trans. Biomed. Eng.*, 2019, doi: 10.1109/tbme.2019.2904398.

[18] T. Deffieux, J. L. Gennisson, M. Tanter, M. Fink, and A. Nordez, 'Ultrafast imaging of in vivo muscle contraction using ultrasound', *Appl. Phys. Lett.*, vol. 89, no. 18, pp. 2006–2008, 2006, doi: 10.1063/1.2378616.

[19] F. Molinari, C. Caresio, U. R. Acharya, M. R. K. Mookiah, and M. A. Minetto, 'Advances in Quantitative Muscle Ultrasonography Using Texture Analysis of Ultrasound Images', *Ultrasound Med. Biol.*, vol. 41, no. 9, pp. 2520–2532, Sep. 2015, doi: 10.1016/j.ultrasmedbio.2015.04.021.

[20] A. Botter and T. M. Vieira, 'Filtered virtual reference: A new method for the reduction of power line interference with minimal distortion of monopolar surface EMG', *IEEE Trans. Biomed. Eng.*, vol. 62, no. 11, pp. 2638–2647, 2015, doi: 10.1109/TBME.2015.2438335.

[21] A. Holobar, M. A. Minetto, A. Botter, F. Negro, and D. Farina, 'Experimental analysis of accuracy in the identification of motor unit spike trains from high-density surface EMG', *IEEE Trans. Neural Syst. Rehabil. Eng.*, vol. 18, no. 3, pp. 221–229, 2010, doi: 10.1109/TNSRE.2010.2041593.

[22] A. Holobar, M. A. Minetto, and D. Farina, 'Accurate identification of motor unit discharge patterns from high-density surface EMG and validation with a novel

signal-based performance metric', *J. Neural Eng.*, vol. 11, no. 1, 2014, doi: 10.1088/1741-2560/11/1/016008.

[23] A. HOLOBAR, D. FARINA, M. GAZZONI, R. MERLETTI, and D. ZAZULA, 'Estimating motor unit discharge patterns from high-density surface electromyogram.', *Clin. Neurophysiol.*, vol. 120, pp. 551–562, 2009.

[24] A. Holobar and D. Zazula, 'Multichannel blind source separation using convolution Kernel compensation', *IEEE Trans. Signal Process.*, vol. 55, no. 9, pp. 4487–4496, 2007, doi: 10.1109/TSP.2007.896108.

[25] R. Rohlen, E. Stalberg, K. H. Stoverud, J. Yu, and C. Gronlund, 'A Method for Identification of Mechanical Response of Motor Units in Skeletal Muscle Voluntary Contractions Using Ultrafast Ultrasound Imaging - Simulations and Experimental Tests', *IEEE Access*, vol. 8, pp. 50299–50311, 2020, doi: 10.1109/ACCESS.2020.2980053.

[26] T. Deffieux, J. L. Gennisson, M. Tanter, and M. Fink, 'Assessment of the mechanical properties of the musculoskeletal system using 2-D and 3-D very high frame rate ultrasound', *IEEE Trans. Ultrason. Ferroelectr. Freq. Control*, vol. 55, no. 10, pp. 2177–2190, 2008, doi: 10.1109/TUFFC.917.

[27] C. Grönlund, K. Claesson, and A. Holtermann, 'Imaging Two-Dimensional mechanical waves of skeletal muscle contraction', *Ultrasound Med. Biol.*, vol. 39, no. 2, pp. 360–369, 2013, doi: 10.1016/j.ultrasmedbio.2012.09.005.

[28] R. Rohlén, E. Stålberg, and C. Grönlund, 'Identification of single motor units in skeletal muscle under low force isometric voluntary contractions using ultrafast ultrasound', *Sci. Rep.*, vol. 10, no. 1, pp. 1–11, 2020, doi: 10.1038/s41598-020-79863-1.

[29] K. Roeleveld, D. F. Stegeman, H. M. Vingerhoets, and A. Van Oosterom, 'The motor unit potential distribution over the skin surface and its use in estimating the motor unit location', *Acta Physiol Scand*, vol. 161, pp. 465–472, 1997.

[30] D. F. Stegeman, D. Dumitru, J. C. King, and K. Roeleveld, 'Near- and far-fields: Source characteristics and the conducting medium in neurophysiology', *J. Clin. Neurophysiol.*, vol. 14, no. 5, 1997, doi: 10.1097/00004691-199709000-00009.

[31] A. Botter, T. Vieira, M. Carbonaro, G. L. Cerone, and E. F. Hodson-Tole, 'Electrodes' Configuration Influences the Agreement between Surface EMG and B-Mode Ultrasound Detection of Motor Unit Fasciculation', *IEEE Access*, vol. 9, pp. 98110–98120, 2021, doi: 10.1109/ACCESS.2021.3094665.

[32] A. H. Caillet, A. T. M. Phillips, D. Farina, and L. Modenese, 'Estimation of the firing behaviour of a complete motoneuron pool by combining electromyography signal decomposition and realistic motoneuron modelling', *PLOS Comput. Biol.*, vol. 18, no. 9, p. e1010556, Sep. 2022, doi: 10.1371/journal.pcbi.1010556.

[33] A. Del Vecchio, A. Holobar, D. Falla, F. Felici, R. M. Enoka, and D. Farina, 'Tutorial: Analysis of motor unit discharge characteristics from high-density surface EMG signals', *J. Electromyogr. Kinesiol.*, vol. 53, p. 102426, 2020, doi: 10.1016/j.jelekin.2020.102426.

[34] P. W. H. Eduardo Martinez-Valdes, Roger M. Enoka, Aleš Holobar, Kevin McGill, Dario Farina, Manuela Besomi, François Hug, Deborah Falla, Richard G. Carson, Edward A. Clancy, Catherine Disselhorst-Klug, Jaap H. van Dieën, Kylie Tucker, Simon Gandevia, Madeleine Low, 'Consensus for experimental design in

electromyography (CEDE) project: Single motor unit matrix', *J. Electromyogr. Kinesiol.*, vol. 64, p. 102726, 2022, doi: 10.1016/j.jelekin.2022.102656.

[35] R. Merletti, A. Holobar, and D. Farina, 'Analysis of motor units with high-density surface electromyography', *J. Electromyogr. Kinesiol.*, vol. 18, no. 6, pp. 879–890, 2008, doi: 10.1016/j.jelekin.2008.09.002.

[36] T. M. Vieira, A. Botter, S. Muceli, and D. Farina, 'Specificity of surface EMG recordings for gastrocnemius during upright standing', *Sci. Rep.*, vol. 7, no. 1, Art. no. 1, Oct. 2017, doi: 10.1038/s41598-017-13369-1.

[37] M. Minetto *et al.*, 'Feasibility study of detecting surface electromyograms in severely obese patients.', *J. Electromyogr. Kinesiol.*, vol. 23, pp. 285–295, 2013, doi: 10.1016/j.jelekin.2012.09.008.

[38] K. G. Keenan, D. Farina, K. S. Maluf, R. Merletti, and R. M. Enoka, 'Influence of amplitude cancellation on the simulated surface electromyogram', *J. Appl. Physiol.*, vol. 98, no. 1, 2005, doi: 10.1152/japplphysiol.00894.2004.

[39] R. Waasdorp *et al.*, 'Combining Ultrafast Ultrasound and High-Density EMG to Assess Local Electromechanical Muscle Dynamics: A Feasibility Study', *IEEE Access*, vol. 9, pp. 45277–45288, 2021, doi: 10.1109/ACCESS.2021.3067162.

Chapter 5

Topic 3

5.1 Spatial repeatability approach to enhance the identification of US components associated with MU activity

In the previous Chapters, we evaluated the performance of the proposed algorithm for ultrafast US and HDsEMG data integration based on the spatio-temporal decomposition of tissue velocity sequence (STICA approach). In this Chapter, the joint analysis of HDsEMG and ultrafast US was used to assess the repeatability of the ultrasound decomposition processing. The decomposition algorithm based only on the UUS processing described in previous studies provides reliable identifications (anatomical location and twitch profile) of components associated with MU activity [1]–[4]. Our integrated algorithm (STICA algorithm) was based on the decomposition of tissue velocities estimated from UUS and used the firing instants obtained from HDsEMG decomposition to find groups of highly correlated ultrasound components with the electrical activity. In order to improve the quality of tissue velocities decomposition, in this study we proposed an innovative approach to enhance the identification of US components that are most likely associated with MU activity. A more reliable identification of these components may improve the outcomes of the integrated algorithm. For this reason, an assessment of the repeatability of the US-decomposed components (which may be associated with MU activity) is worth of investigation.

The tissue displacement velocities estimated from ultrafast US can be decomposed into multiple components, which comprise a spatial map (location of the component, related to MU territory) and a temporal signal (time course of its displacement velocity, related to MU spike train) [5]. A critical step of the EMG-US integration at the MU level is the association between MU activity and US components from high frame rate US sequences. To date, a procedure based on temporal signal characteristics was adopted to associate *US components* to MU activity decomposed from EMG (high density or needle) [1], [3]. For example, in our STICA approach we measured cross-correlation between the temporal components and a synthetic *train of MU velocity twitches* obtained from the MU firing instants (see Figure 3.4). The cross-correlation values obtained in our data were in general low. It is worth noting that also other metrics, e.g. the rate of agreement between the spike instants obtained from the US temporal components and those identified from needle EMG demonstrated a large proportion of US component' temporal signals not matched with MU firings [1], [2]. The relatively low agreement between the two measures was attributed to two factors. Firstly, the composition of linear and non-linear elastic tissue constituents is heterogenous, resulting in a non-linear combination of MU twitches [6]. Secondly, the variability in the firing of MUs [7], which can affect the temporal twitch parameters and alter the sequence of twitches [2], [6], even though the MU pool should remain stable during contractions.

In this Chapter, we propose a novel analysis based on *spatial* characteristics to identify US components associated with MU activity. This procedure is expected to enhance the decomposition of tissue velocity by providing new criteria to separate US components putatively associated with MUs from the noisy components (not associated with MU activity). The proposed approach is based on the assumption that, while the temporal firing characteristics of MU fibers may vary during constant force and isometric contractions, MU location within the muscle cross-section (spatial characteristic) should remain consistent. Therefore, components that have a stable and repeatable spatial map (i.e. spatial components) throughout the contraction are more likely to be linked to actual MU activations.

The goal of our study was to identify spatially repeatable components within a US sequence and explore whether such repeatability can help distinguish MU from noise in stable, low-force isometric contractions. We achieved this by segmenting tissue velocity images from eight-second US recordings into consecutive two-second epochs. We assessed the repeatability of the components' spatial maps across the epochs (*intra-sequence repeatability*) and investigated if the repeatable components were associated with MU activity. To do this, we used a set of reference MUs independently identified by HDsEMG decomposition [8]. Hence, in this study we used HDsEMG as a ground truth for the verification that spatially repeatable components are associated with MU activity.

If the proposed approach based of repeatability of spatial US components was proved effective, it could enhance integrated algorithms of HDsEMG and ultrafast US, as the one

proposed in this thesis, but it may also provide a foundation for developing a stand-alone method to identify MU in ultrafast US.

5.2 Methods

Figure 5.1 shows an overview of the data acquisition and processing performed for the assessment of US components' repeatability as a tool to select *putative MU* activity. In the following paragraphs all the steps are explained.

5.2.1 Experimental protocol

The details of the experimental protocol (Figure 5.1A) are reported in the previous Chapter. Briefly, for each low-level isometric constant-force elbow flexions, eight-second-long UUS recordings were recorded simultaneously with HDsEMG. Five subjects (31 ± 6 years, three males, and two females) were analysed in this study.

5.2.2 UUS and HDsEMG data processing

The radio frequency UUS data consisted of 20,000 frames (2176x128 pixels, about 53x40 mm, Figure 5.1B). After standard delay-and-sum beamforming, each eight-second dataset was segmented into seven sub-datasets of two seconds, with a one-second overlap between each ([0:2] s, [1:3] s, ..., [6:8] s) (Figure 5.1C). Each pixel in each sub-dataset underwent temporal filtering using a 1D median filter. The resulting image was cropped to 20x40 mm (850x128 pixels) (Figure 5.1D), as we demonstrated in the previous Chapter that the association with HDsEMG MU is stronger for superficial components. We therefore considered the superficial 20 mm of the muscle. Displacement velocity images were calculated for each two-second epoch using 2D autocorrelation velocity tracking [9] with a sliding window of 10 ms and a depth of 1 mm (Figure 5.1E). The temporal evolution of each pixel in the velocity images was high-pass filtered at 3 Hz using a 3rd order Butterworth filter (zero-phase) to remove slow movements unrelated to muscle contraction. The velocity images were downsampled to 63x128 pixels, corresponding to approximately 0.3x0.3 mm per pixel. The HDsEMG signals were bandpass filtered between 20-400 Hz and decomposed into individual MU spike trains (Figure 5.1K). The spike trains were edited [10] and resampled at the ultrasound frame rate. The amplitude distributions and centroids of MUAPs were calculated using the longitudinal single differential derivation and averaging with spike trains from HDsEMG decomposition [8]. As the mediolateral surface covered by the HDsEMG grid is larger than that of the ultrasound transducer (Figure 5.1A), any centroids with a mediolateral coordinate outside of the ultrasound field of view was truncated to the position of the first or last element of the probe (i.e., element 1 or 128).

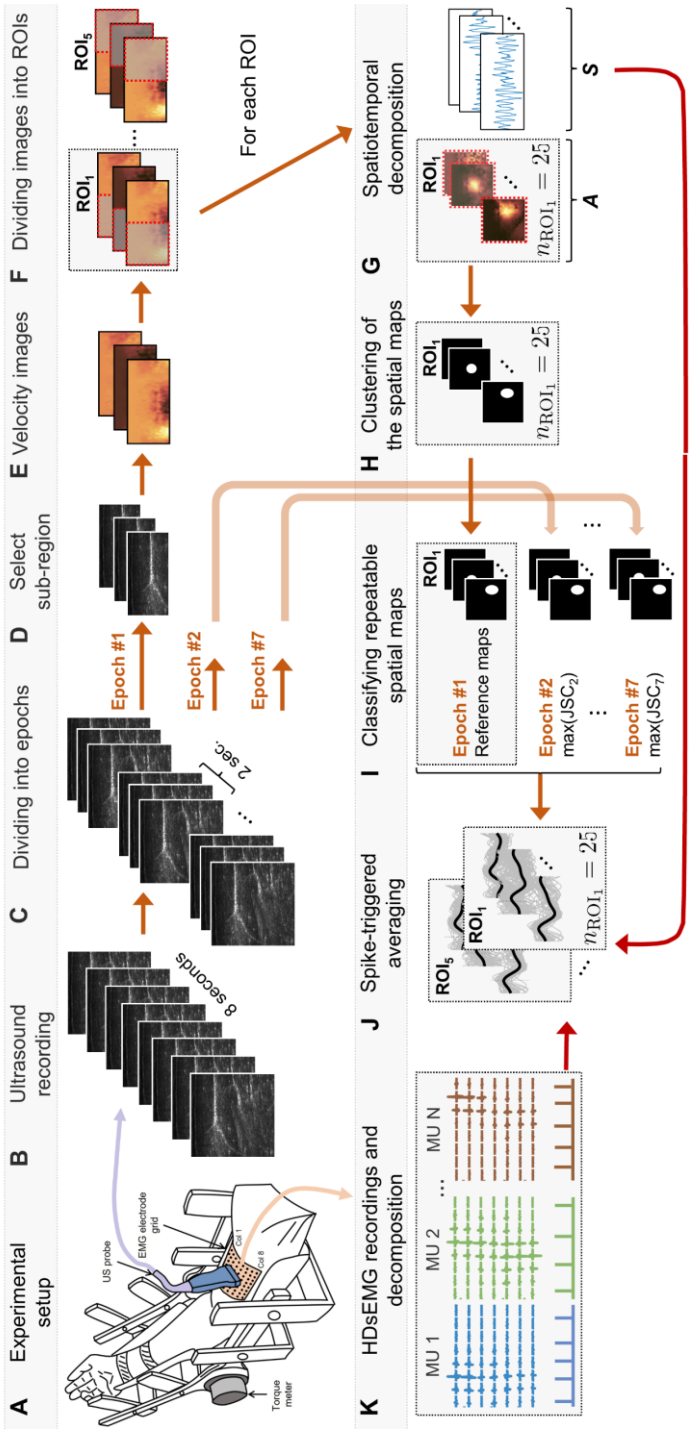

Figure 5.1 Illustration of the ultrasound data processing and intra-sequence repeatability approach. A. Experimental setup with simultaneous ultrafast ultrasound (UUS) and high-density surface electromyography (HDsEMG) recordings (see details in the previous chapter). B. Eight-second recordings using UUS (40x40 mm, 2500 Hz) plane wave imaging. C. The recordings were divided into seven partially overlapping epochs of two seconds each. D. A sub-region was selected within the HDsEMG detection volume (20x40 mm). E. Tissue velocity images were estimated. F. The velocity images were divided into five region-of-interests (ROIs), i.e., 20x20 mm each. G. Each ROI was decomposed into 25 components, i.e., 25 temporal signals (‘ S’) and 25 spatial maps (‘ A’). H. The spatial maps were clustered and processed to generate a binary map, with zeros being the background and ones being the largest intensity of the territory. I. The binary maps were used for calculating the Jaccard Similarity Coefficient (JSC) for each component in the epoch (second to the seventh) with the first epoch as a reference. The maximal JSC was retained for each epoch, and then the mean JSC (based on the maximal JSC for all epochs) was calculated. J. Then, spike-triggered averaging of the components’ temporal signal was performed using the motor unit (MU) spike trains instants from the K. HDsEMG decomposition.

5.2.3 Spatiotemporal decomposition of displacement velocity image

In this study, the displacement velocity images were analyzed using five partially overlapping Regions of Interest (ROIs) of 20x20 mm (5 mm increments) (Figure 5.1F) [1]. We employed spatiotemporal independent component analysis (stICA) with $\alpha = 1.0$ [11] to generate 25 spatial components (spatial maps) and corresponding temporal components (temporal signals) per ROI (Figure 5.1G). Therefore, we obtained 125 spatio-temporal *ultrasound components* for each recording.

Binary maps were generated from the spatial maps for the use in the following repeatability analysis (Figure 5.1H). To cluster the intensities of each spatial map, we employed the k-means algorithm with five clusters, using Euclidean distance. The cluster with the greatest intensity values was identified as the localized spatial region (territory) of interest. A binary map was then created based on this cluster. Any objects with fewer than 25 connected pixels (~1.5x1.5 mm2) were eliminated to eliminate noisy pixels in other areas of the image.

5.2.4 Repeatability analysis: selecting similar spatial maps across epochs (intra-sequence approach)

A Jaccard Similarity Coefficient (JSC) criterion based on the binary maps was used to select the set of spatial maps that were maximally similar across different time epochs. Specifically, the 25 spatial maps of the first two-second epoch for each ROI were considered as reference maps (Figure 5.1I). Jaccard Similarity Coefficients were computed between each reference map and the 25 maps obtained from each of the remaining six epochs. For each epoch, the map with the highest JSC was retained. Six spatial maps (one each epoch) that were maximally similar (JSC-wise) to each reference map were chosen (see Figure 5.4, in which the selected maps for each time windows are highlighted with all the JSC values). Using the chosen maps, the mean spatial map and mean JSC, which represents the degree of repeatability of a component, were then computed. Each of the five ROIs had a total of 25 mean spatial maps identified, for a total of 125 mean spatial maps (considering all five ROIs). This repeatability analysis is hereafter referred to as *intra-sequence repeatability approach*.

5.2.5 Association of components with MUs from HDsEMG

We investigated the relationship between the repeatable US spatial components selected in the previous paragraph and the characteristics of individual MUs identified through HDsEMG decomposition in order to confirm our hypothesis that spatially-repeatable US components are in fact related to MU activity and should be retained. In order to achieve this, we considered the average twitch computed from the firing pattern of the MUs found with HDsEMG decomposition and the temporal signal of the selected

spatial maps. We assumed that if the twitch obtained by spike-triggered averaging of the temporal signal using the firing of the MU has high signal to noise ratio, the component and the MU are likely associated. Although less rigorous, this metric is more robust than the RoA (between EMG and US identified firings) to local, missing firings, which may occur, especially in US decomposition.

For this purpose, the temporal signals of each set of selected components were spike-triggered averaged (Figure 5.1J) using the spike train of individual MUs identified from HDsEMG (Figure 5.1K). All the combinations of the selected ultrasound components and HDsEMG MUs were tested with this method, producing a large number of *putative twitches* (Figure 5.1J). Figure 5.2 shows a description of this step. Among these putative twitches, only those whose peak-to-peak amplitude was greater than a noise threshold were kept. The pair (ultrasound component - HDsEMG MU) resulting to the largest amplitude among this subset was referred to as the *MU-matched component* (Figure 5.2). The noise threshold was determined by producing 125 temporal components of colored noise (5-30 Hz bandwidth of white noise), which were then spike-triggered averaged with 100 random spike trains (mean firing rates between 8-20 Hz and standard deviation of 15% of the mean inter-pulse interval [31]) to determine the threshold. The mean plus three standard deviations of the peak-to-peak amplitudes of all the combinations of the inputs were used to calculate the threshold value (Figure 5.3).

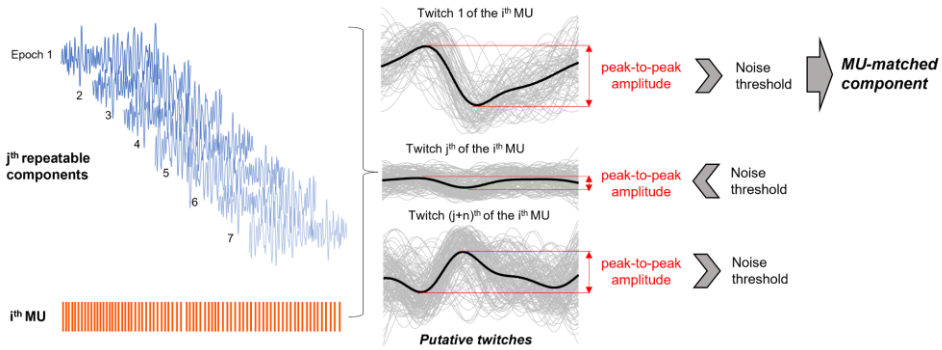

Figure 5.2 Association of components with MUs from HDsEMG. Pipeline for the computation of spike triggered averaging of all the combination of MUs and components. For the for all the j^{th} components, the averaged twitch is computed with respect to the i^{th} MU, generating a *putative twitch*. All the twitches showing peak-to-peak amplitude higher than the noise threshold were kept. The component with the greatest twitch amplitude among all the over-threshold putative twitches of the i^{th} MU was selected and referred as the *MU-matched component*. This procedure was repeated for all the EMG decomposed MUs. If none of the putative twitches exceeded the threshold the i^{th} MU was regarded as not identified.

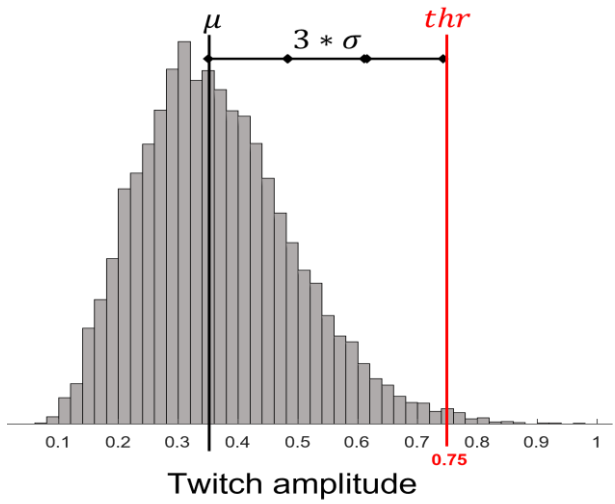

Figure 5.3 Noise threshold computation. Histogram of all the amplitudes calculated from the spike triggered averaging of 125 simulated components (colored noise, 5-30 Hz bandwidth) for all the 100 random spike trains. From this distribution the mean (μ) and the standard deviation (σ) were calculated to compute the threshold value of 0.75.

5.2.6 Number of MU-matched components: intra- and full-sequence approaches comparison

The method proposed in this Chapter requires the analysis of US sequences over short epochs (2-s) to perform a repeatability evaluation. It is therefore reasonable to ask if and to what extent the 2 s data segmentation (*intra-sequence approach*) impacts the results of the US decomposition in terms of number of components that can be matched with EMG MUs. We therefore compared the number of MU-matched components found using the intra-sequence repeatability method with those that were decomposed by the stICA applied over the entire sequence recording (*full-sequence approach*) [1]. The matching with HDsEMG MUs was carried out using the same procedure in both techniques, as previously mentioned (i.e. amplitude of the spike triggered average twitch).

5.2.7 Statistical analysis

In order to describe the components (identified with repeatability analysis and full-sequence analysis) and the MUs decomposed from HDsEMG, descriptive statistics were performed. We determined the area (a), equivalent diameter ($d = \sqrt{4a/\pi}$), and depth of the centroid of the component beneath the skin using the MU-matched component. We calculated for each MU-matched component the distance between the mediolateral centroids of the spatial map (based on the binary map) and MUAP spatial distribution

(based on the spike-triggered average on the HDsEMG signals using the MU spike trains), as metrics of accuracy of our identification as already explained in the previous chapters.

Using a two-sided Wilcoxon signed rank test, we examined the pairwise difference between the number of MU-matched components between the full- sequence method and the intra-sequence repeatability.

5.3 Results

5.3.1 MU identification and repeatable components

Out of 20 recordings, 99 MUs (4.9 ± 1.8 MUs per recording) were identified by decomposing HDsEMG signals.

We observed various degrees of intra-sequence repeatability across the 125 ultrasound components per recording, as shown by the large variability of JSC values (Figure 5.4). Figure 5.5 depicts an example of the output of the repeatability analysis with two examples of repeatable components (high mean JSC) and one non-repeatable component (low mean JSC) from one ROI of a representative subject recording.

5.3.2 Association of components with MUs from HDsEMG

The scatterplot in Figure 5.6 illustrates the correlation between JSC values and the amplitudes of putative twitches across all individuals and trials. The HDsEMG MU and ultrasound component associated with each data point in Figure 5.6 correspond to the putative twitches with the maximum amplitude (within all the combinations). Among these data points, those below the noise thresholds (*non-MU-matched components*, grey dots in Figure 5.6) were not considered because they were not associated with MUs. In several cases, the same MU and more ultrasound components provided a putative twitch above threshold (*duplicates*, colored dots in Figure 5.6). In these instances, only the component that produced the largest putative twitch (*MU-matched components*, red circles in Figure 5.6) was kept.

In comparison to the non-MU-matched (grey dots) components, the MU-matched components had a higher JSC (Figure 5.6, 0.61 ± 0.12 vs 0.26 ± 0.26; $p < 0.001$). Moreover, as depicted by the examples in Figure 5.7, MU-matched components were spatially (medio-laterally) adjacent to the MUAP distribution (Table 5.1), as demonstrated by the mediolateral distance between the centroid of the MUAP distributions and the centroid of the spatial maps (5.35 ± 5.17 mm, N = 35 MU). The centroids of the mean spatial maps were distributed across the whole field of view with depths between 2.90 mm and 14.01 mm (Table 5.1). In addition, the MU-matched components had a diameter of 4.03 ± 1.28 mm, similar to previously reported findings of MU territory size using scanning-EMG [12], [13].

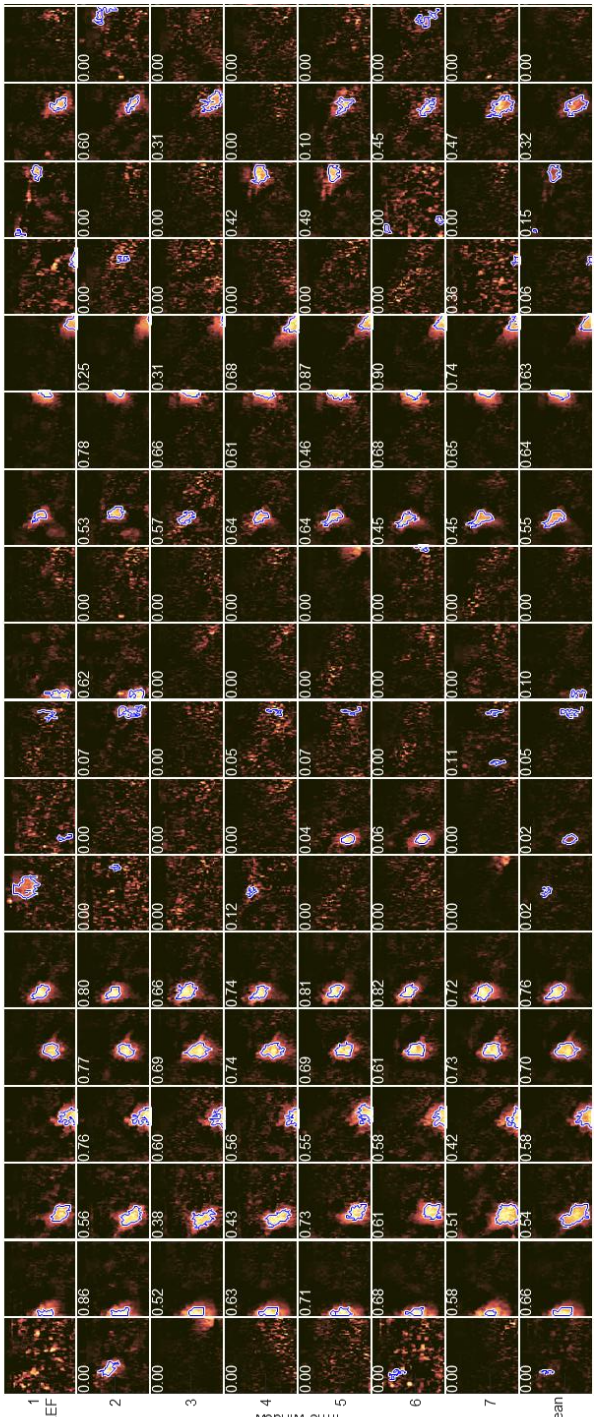

Figure 5.4 Example of repeatability analysis. Example of 18 (out of 25) components (columns) over the seven epochs (rows) with the corresponding Jaccard Similarity Coefficient (JSC) calculated with respect to the reference first epoch. The last row shows the averaged spatial maps. The blue lines represent the territories identified in the images with the k-means pixel clustering. This figure shows the large variability of JSC values.

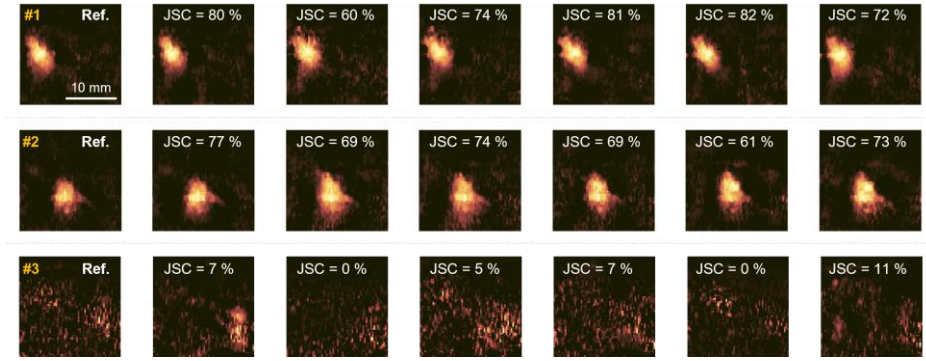

Figure 5.5 Examples of spatial maps. Two repeatable components (#1 to #2) and one non-repeatable component (#3) of the same recording and region-of-interest (ROI) based on the Jaccard Similarity Coefficient (JSC). The first two-second epoch is the reference (defined as Ref).

The MU-matched components had a mean JSC consistently higher than 0.38, indicating fair repeatability (see examples in Figure 5.4 and Figure 5.5). Each recording had 6.5 ± 3.3 repeatable components (without *duplicates* in Table 5.2) when the empirical criterion of 0.38 was used to define the components as repeatable (*US-RepMap* in Table 5.2).

The spatial agreement between MUAP distributions and spatial maps of the MU-matched components, as well as the associated velocity twitches derived using spike trigger

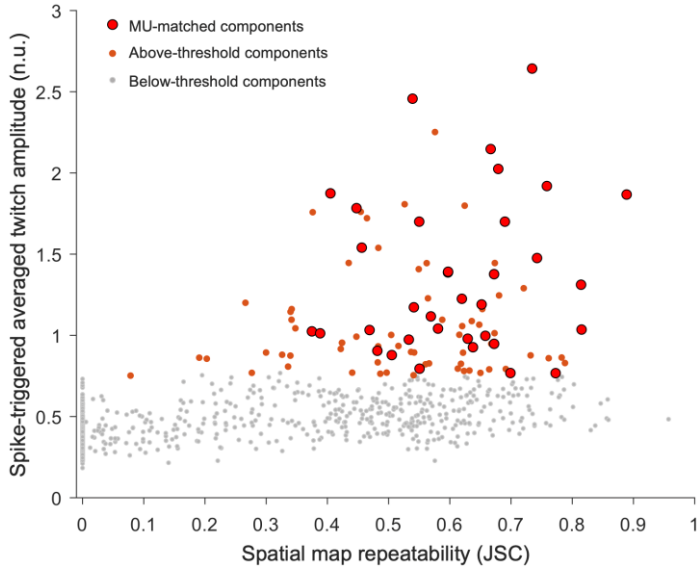

Figure 5.6 Relationship between Jaccard Similarity Coefficient (JSC) and putative twitches with the highest spike-triggered averaged twitch amplitude. Grey dots are the putative twitches below the noise threshold that were discarded. The red circles correspond to the 35 MU-matched components. All the MU-matched components have JSC over 0.38 (i.e., repeatable). Orange dots refer to multiple components associated with the same MU (e.g., twisting/split territory, duplicate components, etc., see Figure 5.8).

Table 5.1 Descriptive statistics about the motor unit-matched repeatable components.

MU-matched repeatable components	N = 35
Jaccard Similarity Coefficient, JSC	0.61 ± 0.13 (0.38; 0.89)
Amplitude (n.u)	1.35 ± 0.49 (0.76; 2.64)
Centroid-to-centroid (EMG-UUS) (mm)	5.35 ± 5.17 (0.01; 15.83)
Depth (mm)	9.47 ± 2.40 (2.90; 14.01)
Diameter (mm)	4.03 ± 1.28 (1.45; 7.25)
Area (mm^2)	14.06 ± 8.71 (1.66; 41.30)

Mean ± SD (min; max), MU = motor unit, EMG = electromyography, UUS = ultrafast ultrasound, n.u. = normalised units.

averaging over all the MU firings of all epochs, are illustrated by three representative cases in Figure 5.7.

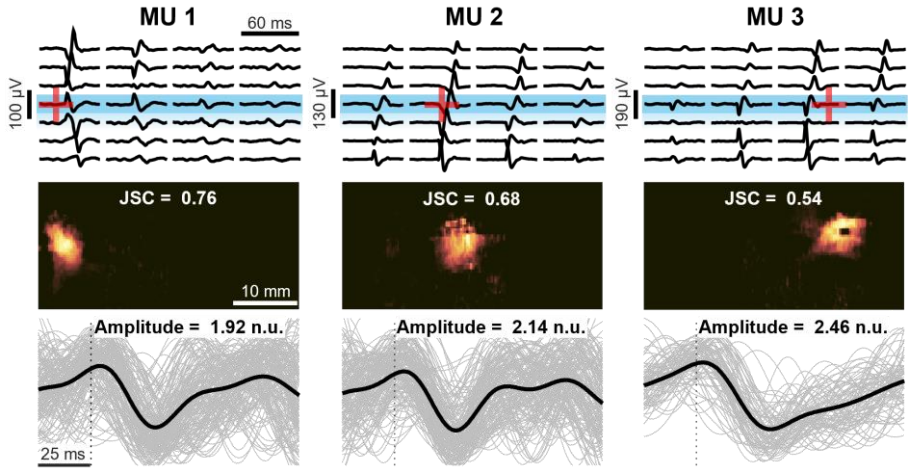

Figure 5.7 Three representative matches between repeatable components and the motor units (MUs). The upper panels show the MU action potentials and the centroid of the EMG distribution (red '+'). In this representation, only the four columns of the EMG grid superimposed on the ultrasound probe (blue rectangle) are shown. The middle panels show the mean spatial map of the repeatable component and the corresponding mean JSC. Finally, lower panels depict the spike-triggered averaged velocity twitch (black line) based on the triggered signals from all seven epochs (grey lines) and the corresponding peak-to-peak amplitude. The vertical dotted lines corresponded to the firing instants of the MUs identified from HDsEMG decomposition and used for the triggering.

Number of matched components with MUs from HDsEMG: intra and full sequence approach

A total of 35 MU-matched components were found by the intra-sequence analysis, 35.4% of the MUs found through HDsEMG (Table 5.2). We detected 36 matches by decomposing the entire eight-second UUS (full-sequence), 36.4% of the MUs determined by HDsEMG. Strikingly, we found no difference between intra- (2 s analysis) and full-sequence (8 s analysis) approaches in the total number of matched MUs across all recordings ($p = 0.9844$).

5.4 Discussion

This study investigated whether muscle tissue displacements related to single MU activation could be identified during steady low-force isometric contractions exploiting the spatial repeatability of components decomposed from UUS sequences. First, displacement velocity sequences estimated from eight second UUS recordings of consecutive two-second epochs were decomposed into spatial and temporal components using stICA. Then, we measured the spatial map repeatability of the components across epochs and looked for a correlation between the level of repeatability and the degree of agreement with reference to MUs identified through HDsEMG decomposition. We found three main results: (1) the components with JSC > 0.38 represented roughly 14% of the 125 initial components from each recording, (2) all the MU-matched components had a JSC larger than 0.38, and (3) the number of MU-component matches did not differ between the intra- and full-sequence approaches.

Approximately 14% of the spatiotemporal components found using stICA on UUS sequences matched with MUs that were independently decomposed from HDsEMG. The high JSC of the spatial maps was a common characteristic to all the MU-matched components. According to this data, spatial repeatability over a brief epoch is a crucial feature that can be used to identify potential MUs and apply data reduction to the initial ultrasound component set. This finding supports the initial idea that repeatable spatial maps are more likely to be associated to actual MUs since the placement of the MU fibers is an invariant property of the MU during stable isometric contractions. Whether this hypothesis applies to conditions other than isometric or constant force contractions likely depends on how MU territory is represented in the ultrasound scanning plane and how this representation changes during a contraction. For instance, changes in muscle shape caused by dynamic contractions may result in a shift or a change in the shape of the region inside the ultrasound scanning plane where the activation of MU fibers generates movement within the muscle cross-section. The assumption that underlies our hypothesis (i.e. MU territory spatial invariance) would be weakened by this. Similar variations in MU area representation may occur during isometric contractions, although to a smaller amount, for

example, during force-varying contractions, fatiguing contractions, or any circumstance causing a progressive MU recruitment or de-recruitment.

One third of the MUs identified through HDsEMG decomposition matched a repeatable ultrasound component. This proportion is similar to the number of accurate identifications (i.e. matches) found in earlier studies [1], [14]. This low percentages of matches with respect to the EMG reference has previously been linked to several aspects. First, the differences in the detection volumes and features of the two detection systems (EMG and ultrasound) [14] is a relevant aspect in this regard. The EMG spatial sensitivity is considered as a superficial, hemispherical volume while the US is sensitive to movements in a section of the tissue. While the action potential of excited fibers may cross the detection volume of EMG, it is possible that these fibers outside the scanning plane may not produce a detectable movement in the US image. On the other hand, a MU motion taking in place in the deeper muscle region can be captured by US but may not be visible in EMG signals. Second, it is important to remember again that the measured system (muscle tissue) is anticipated to be non-linear due to the heterogeneous mix of linear and non-linear elastic constituents [6]. The stICA algorithm relies on the main assumption of independent source signals mixed following a linear model. Thus, the identified components, although repeatable, cannot be properly matched with EMG-detected MUs. In our scenario, these non-linearities may have affected the number of matches because, already at 5–10% MVC, many MUs are active [15] and consequently the triggered twitch amplitude (our matching criteria) might be suppressed or degraded.

It is worth noting that, in this study, we found more repeatable ultrasound components for each recording (6.5 ± 3.3) than HDsEMG MUs (4.9 ± 1.8). Although HDsEMG has a lower spatial resolution and a smaller field of view than ultrasound, it is still unknown if these unmatched repeatable components are MUs. Moreover, the number of successful identifications may be skewed in the current investigation by one participant for whom our matching criteria produced no matched MUs. In both the intra-sequence repeatability technique and the original full-sequence decomposition, the exclusion of this subject would have improved the percentage of MU-matches from 35.4% to 42.7% and from 36.4% to 43.9%, respectively (Table 5.2).

Table 5.2 Descriptive statistics about the recordings, decomposed EMG MUs and ultrasound components.

Trials	Subject	MU	US-EMG match	% of US-EMG match	8s US-EMG match	8s % of US-EMG match	US-RepMap	% of US-RepMap	No-duplic.
1	**S1**	10	3	30.0%	5	50.0%	21	16.8%	9
2	**S1**	3	2	66.7%	2	66.7%	15	12.0%	6
3	**S1**	6	0	0.0%	1	16.7%	13	10.4%	4
4	**S1**	3	2	66.7%	2	66.7%	18	14.4%	4
5	**S2**	5	4	80.0%	4	80.0%	21	16.8%	7
6	**S2**	7	0	0.0%	1	14.3%	22	17.6%	7
7	**S2**	4	1	25.0%	2	50.0%	19	15.2%	9
8	**S2**	4	1	25.0%	1	25.0%	19	15.2%	8
9	**S2**	4	2	50.0%	2	50.0%	15	12.0%	7
10	**S3**	5	2	40.0%	4	80.0%	8	6.4%	2
11	**S3**	3	3	100.0%	1	33.3%	20	16.0%	6
12	**S4**	8	6	75.0%	4	50.0%	28	22.4%	9
13	**S4**	5	3	60.0%	3	60.0%	26	20.8%	14
14	**S4**	6	2	33.3%	2	33.3%	24	19.2%	11
15	**S4**	4	1	25.0%	0	0.0%	13	10.4%	4
16	**S4**	5	3	60.0%	2	40.0%	23	18.4%	10
17	**S5**	4	0	0.0%	0	0.0%	22	17.6%	7
18	**S5**	5	0	0.0%	0	0.0%	8	6.4%	2
19	**S5**	5	0	0.0%	0	0.0%	11	8.8%	3
20	**S5**	3	0	0.0%	0	0.0%	5	4.0%	1
	Total	**99**	**35**	**35.4%**	**36**	**36.4%**	**351**		**130**
	Average	**4.95**	**1.75**	**36.8%**	**1.8**	**35.8%**	**17.55**	**14.0%**	**6.5**
	SD	**1.8**	**1.6**	**31.6%**	**1.5**	**27.7%**	**6.3**	**5.1%**	**3.3**
	Without S5	**82**		**42.7%**		**43.9%**			

'US-EMG match' = number of MU that could be matched with an ultrasound component (high amplitude twitch).
'% US-EMG match' = percentage with respect to the number of EMG MUs.
'8s' when referring to the full-sequence approach, otherwise we referred to intra-sequence approach.
'US-RepMap' = components with JSC over the empirical threshold of 0.38 (i.e. repeatable).
'% of US-RepMap' = percentage of US-RepMap with respect to the total 125 decomposed ultrasound components.
No-duplic. = Duplicates and splitting components in the US-RepMap were counted as one component.
'Without S5' = without considering the subject 5 in which no MU could be matched.

We found a great number of ultrasound repeatable components (17.6 ± 6.3, Table 5.2). Although this number was already much smaller than the initial set of ultrasound component (14%), there were probably a considerable number of *multiple components.* In this regard, the use of the stICA over partially overlapping region of interest of the displacement velocity images created a relevant number of duplicate components. In the two examples shown in Figure 5.8a, three distinct components, that were decomposed into three successive ROIs each showing a twitch amplitude that was greater than the noise threshold, were attributed to the same MU. The component that produced the greatest twitch amplitude in this instance was considered to be the MU-matched component. Another important aspect to be considered in the generation of multiple components is that the stICA method we employed for decomposition assumes spatial independence [5]. If the MU activation causes complex motions such that regions that are spatially distant from each other observed to move synchronously or in unison, MU areas might split in more components. For instance, these split components may be caused by the interaction of active and passive tissue [16], [17] or tissue rotation caused by what is referred to as MU *twisting* [18]. Two instances of MU twisting of two observed MUs are shown in Figure 5.8b in this regard. In two regions of activation (blue and green spots in Figure 5.8b) close to each other, two components (matched with the same MU) are spatially separated and exhibit inverted twitch shapes (blue and green twitches in Figure 5.8b). The shape of the twitch is related to the direction of the movement. The blue twitches in Figure 5.8b are positive thus away from the probe (i.e. down with respect to the skin), whereas the green ones are negative thus towards the probe (i.e. up). The above-threshold components in

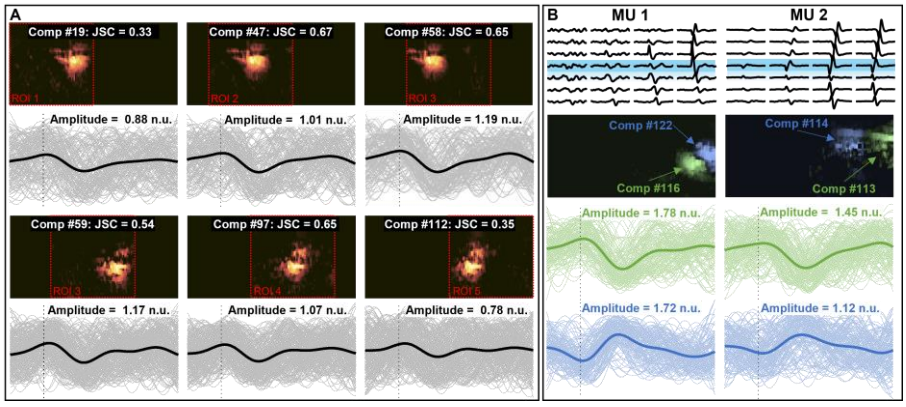

Figure 5.8 Examples of multiple components associated with the same MU. A. Two examples of three different components (belonging to different ROIs) with the same spatial map (active region) that were matched with MUs. In this case, the three components were regarded as unique repeatable components. B. Two examples of possible twisting MUs. The MUs were matched with two components showing active regions close to each other and the average twitches going in opposite directions (green is first positive/up and then negative/down; blue is first negative/down and then positive/up).

Figure 5.6 (little orange spots) are composed of all these cases of multiple components (duplicates, split, and twisting) that have now been separated. The real number of unique repeatable components (considering only one instead of multiple components) was represented by the count of 6.5 ± 3.3 components per trial (Table 5.2). Future research may integrate components from the same MU taking into account the spatial overlay or a correlation technique based on the temporal signals.

In our previous analysis, we demonstrated that our approach might offer an accurate MU displacement area (MU twitching area) estimates also considering short-duration recordings. In fact, the error in the identification of MU (measured with the centroid-to-centroid distance between MUAP and identified MU twitching area, see Figure 4.8), showed no statistical significant difference for the STICA-based identifications between eight or two seconds recordings. This result confirmed the findings of other studies showing the possibility to identify US components reliably associated to MU using short recording (two seconds) [1]. Thus, this ability to estimate displacement area accurately using brief signal epochs may be exploited to implement new STICA-based algorithms, that take advantage of the temporal segmentation to enhance the estimation using a spatial criterion of repeatability of components throughout the contraction. This feature of repeatability of spatial component may be exploited to identify MU activity, that should have stable and repeatable twitching area, excluding those noisy components which, on the other hand, do not show this repeatability.

The ability to identify MUs from a brief sequence with stICA has several advantages compared to the spike-triggered averaging approach. The blind source separation approach has benefits, such as lower memory and storage requirements and the potential to be used for applications like real-time imaging [4] and dynamic contractions. Future studies must take into account the lower constraint for the recording duration for these applications in order to detect MUs and enhance the classification of components into MUs or non-MUs training a classifier utilizing robust features. For instance, a feature for the classification of a component as a MU may be the Gaussian-like 2D distribution of velocities revealed in our work for the most repeated components and comparable to what has been discovered in earlier studies [3], [18]. Thus, having a classifier for MU/non-MU-associated components [19] enables the UUS approach to be stand-alone from HDsEMG.

In summary, this study investigated the relationship between individual MU activity and intra-sequence repeatable components. We observed that 1) a criterion based on spatial repeatability can be employed as a data reduction technique to identify putative MU activity during steady isometric contractions, and 2) the UUS decomposition method can detect potential MU activity in recordings lasting two seconds. These results lay the groundwork for the design of independent techniques for the detection of MU in ultrafast ultrasound, as well as a first step toward real-time imaging of active MU territories.

5.5 References

[1] R. Rohlén, E. Stålberg, and C. Grönlund, 'Identification of single motor units in skeletal muscle under low force isometric voluntary contractions using ultrafast ultrasound', *Sci. Rep.*, vol. 10, no. 1, pp. 1–11, 2020, doi: 10.1038/s41598-020-79863-1.

[2] R. Rohlén, R. Raikova, E. Stålberg, and C. Grönlund, 'Estimation of contractile parameters of successive twitches in unfused tetanic contractions of single motor units – A proof-of-concept study using ultrafast ultrasound imaging in vivo', *J. Electromyogr. Kinesiol.*, vol. 67, Dec. 2022, doi: 10.1016/j.jelekin.2022.102705.

[3] R. Rohlen, E. Stalberg, K. H. Stoverud, J. Yu, and C. Gronlund, 'A Method for Identification of Mechanical Response of Motor Units in Skeletal Muscle Voluntary Contractions Using Ultrafast Ultrasound Imaging - Simulations and Experimental Tests', *IEEE Access*, vol. 8, pp. 50299–50311, 2020, doi: 10.1109/ACCESS.2020.2980053.

[4] R. Rohlén, J. Lundsberg, N. Malesevic, and C. Antfolk, 'A fast blind source separation algorithm for decomposing ultrafast ultrasound images into spatiotemporal muscle unit kinematics', 2022.

[5] J. V. Stone, J. Porrill, N. R. Porter, and I. D. Wilkinson, 'Spatiotemporal independent component analysis of event-related fMRI data using skewed probability density functions', *NeuroImage*, vol. 15, no. 2, pp. 407–421, 2002, doi: 10.1006/nimg.2001.0986.

[6] E. Lubel *et al.*, 'Non-linearity in motor unit velocity twitch dynamics: Implications for ultrafast ultrasound source separation'. bioRxiv, p. 2023.03.24.533983, Mar. 25, 2023. doi: 10.1101/2023.03.24.533983.

[7] D. Farina, L. Fattorini, F. Felici, and G. Filligoi, 'Nonlinear surface EMG analysis to detect changes of motor unit conduction velocity and synchronization', *J. Appl. Physiol.*, vol. 93, no. 5, pp. 1753–1763, 2002, doi: 10.1152/japplphysiol.00314.2002.

[8] A. Holobar and D. Zazula, 'Multichannel blind source separation using convolution Kernel compensation', *IEEE Trans. Signal Process.*, vol. 55, no. 9, pp. 4487–4496, 2007, doi: 10.1109/TSP.2007.896108.

[9] T. Loupas, R. W. Gill, and J. T. Powers, 'An Axial Velocity Estimator for Ultrasound Blood Flow Imaging, Based on a Full Evaluation of the Doppler Equation by Means of a Two-Dimensional Autocorrelation Approach', *IEEE Trans. Ultrason. Ferroelectr. Freq. Control*, vol. 42, no. 4, pp. 672–688, 1995, doi: 10.1109/58.393110.

[10] A. Del Vecchio, A. Holobar, D. Falla, F. Felici, R. M. Enoka, and D. Farina, 'Tutorial: Analysis of motor unit discharge characteristics from high-density surface EMG signals', *J. Electromyogr. Kinesiol.*, vol. 53, p. 102426, 2020, doi: 10.1016/j.jelekin.2020.102426.

[11] R. Rohlén, J. Yu, and C. Grönlund, 'Comparison of decomposition algorithms for identification of single motor units in ultrafast ultrasound image sequences of low force voluntary skeletal muscle contractions', *BMC Res. Notes*, vol. 15, no. 1, p. 207, Jun. 2022, doi: 10.1186/s13104-022-06093-1.

[12] Í. Corera, A. Malanda, J. Rodriguez-Falces, S. Porta, and J. Navallas, 'Motor unit profile: A new way to describe the scanning-EMG potential', *Biomed. Signal Process. Control*, vol. 34, pp. 64–73, Apr. 2017, doi: 10.1016/j.bspc.2016.12.020.

[13] E. Stålberg and P. Dioszeghy, 'Scanning EMG in normal muscle and in neuromuscular disorders', *Electroencephalogr. Clin. Neurophysiol.*, vol. 81, no. 6, pp. 403–416, Dec. 1991, doi: 10.1016/0013-4694(91)90001-k.

[14] A. Botter, T. Vieira, M. Carbonaro, G. L. Cerone, and E. F. Hodson-Tole, 'Electrodes' Configuration Influences the Agreement between Surface EMG and B-Mode Ultrasound Detection of Motor Unit Fasciculation', *IEEE Access*, vol. 9, pp. 98110–98120, 2021, doi: 10.1109/ACCESS.2021.3094665.

[15] A. J. Fuglevand, D. A. Winter, and A. E. Patla, 'Models of recruitment and rate coding organization in motor-unit pools', *J. Neurophysiol.*, vol. 70, no. 6, pp. 2470–2488, 1993, doi: 10.1152/jn.1993.70.6.2470.

[16] J. M. Wakeling *et al.*, 'The Energy of Muscle Contraction. I. Tissue Force and Deformation During Fixed-End Contractions', *Front. Physiol.*, vol. 11, 2020, doi: 10.3389/fphys.2020.00813.

[17] W. Herzog, 'Skeletal muscle mechanics: questions, problems and possible solutions', *J. NeuroEngineering Rehabil.*, vol. 14, no. 1, p. 98, Dec. 2017, doi: 10.1186/s12984-017-0310-6.

[18] E. Lubel, B. Grandi Sgambato, D. Y. Barsakcioglu, J. Ibáñez, M. X. Tang, and D. Farina, 'Kinematics of individual muscle units in natural contractions measured in vivo using ultrafast ultrasound', *J. Neural Eng.*, vol. 19, no. 5, 2022, doi: 10.1088/1741-2552/ac8c6c.

[19] H. Ali, J. Umander, R. Rohlén, and C. Grönlund, 'A deep learning pipeline for identification of motor units in musculoskeletal ultrasound', *IEEE Access*, vol. 8, pp. 170595–170608, 2020, doi: 10.1109/access.2020.3023495.

Chapter 6

Conclusions

In this PhD project, an innovative multimodal approach to investigate the properties of the neuromuscular system was proposed. The research focused on studying the characteristics of single motor units (MUs) by combining electromyography (EMG) and ultrasonography (US) techniques. EMG and US are complementary approaches that provide electrical and mechanical information about muscle excitation and contraction. Advancements in detection systems have improved these techniques, allowing for innovative processing methods. The methods developed during the PhD project integrated high-density surface electromyography and ultrafast ultrasound to provide a comprehensive description of individual MUs, from neural excitation to tissue displacement. Results of the simulated and experimental tests proved the proposed approach suitable to characterize the electromechanical properties of skeletal muscles at a global and at a MU level.

In the following sections, the main achievements of the project are summarized and the future research lines, including applications of the proposed methods, are discussed.

6.1 Main findings

- Two algorithms for the physical and electrophysiological identification of MU characteristics have been developed and tested. Both algorithms were based on the processing of high-density electromyographic signals [1] and ultrafast ultrasound images of the muscle concurrently detected from the same muscle region.
- The algorithms provided as output: (i) the motor unit neural input, i.e. the MU spike train, from a previously described algorithm [1], (ii) the electrical representation in

terms of motor unit action potential; (iii) the anatomical position and dimension of the motor unit twitching territory, (iv) the displacement velocity of the muscle tissue activated by the excited motor unit fibers, i.e. the mechanical twitch (Figure 6.1).

- A simulated environment to control the parameters of the muscle contraction was developed providing high-density electromyographic signals and tissue velocity sequences of the muscle cross-section. This framework was used to test the two algorithms and to define the best parameters for the detection of the anatomical characteristics of single MUs. The comparison between the algorithms was focused on the quantification of the effects of the degree of neural excitation and the level of MU synchronization on the identification of MU twitching areas.
- The simulation results offered quantitative evidence that both algorithms were suitable for the anatomical and mechanical characterization of single MUs. The approach based on the decomposition of the tissue velocity sequences (STICA) outperformed the algorithm based on spike triggered averaging (STA), resulting in the better identification of MU territories with respect to the simulated ones.
- A strong correlation between the areas of the skin where MU action potentials were

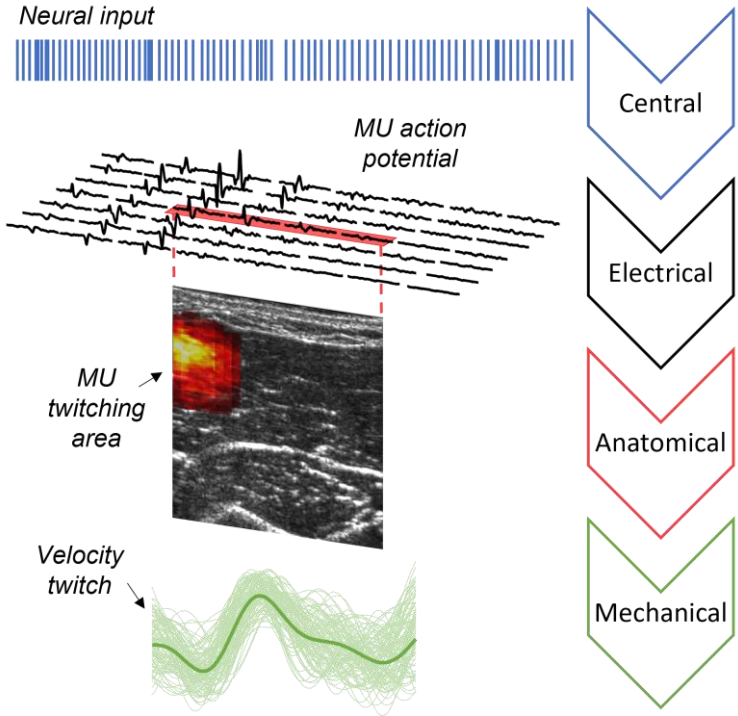

Figure 6.1 Output of the EMG-US method. Three-dimensional representation of the motor unit. The integrated method developed in this thesis allowed the complete neuromechanical characterization of the MU by providing central, electrical, anatomical, and mechanical information.

detected (in the EMG domain) and the corresponding muscle regions where MU mechanical responses were depicted (in the US domain) was obtained in the simulated cylindrical muscle. This US-EMG association was used in the experimental analysis as metric for successful identification of MU.

- The algorithms were applied to experimental data. A protocol for simultaneous high-density electromyography and ultrafast ultrasonography measurements of biceps brachii isometric constant-force contraction was designed.
- The strength of the spatial association between the anatomical and electrical MU representation was dependent on the depth of the MU fibers, suggesting a relevant effect of the EMG and US spatial sensitivity in the experimental results.
- The two proposed approaches demonstrated to be suitable for anatomical in vivo identification of MUs, however the experimental results confirmed the simulations results, suggesting STICA as the best performing algorithm in terms of detecting reliability.
- In the final study, the core of the STICA algorithm, which is the decomposition of ultrasound components from the tissue velocity sequence, was investigated. The spatial repeatability of ultrasound components was proposed to enhance the identification of MU activity and to improve the outcomes of the integrated US-EMG algorithm (i.e. STICA).
- The repeatability analysis strongly reduced the number of ultrasound components to be considered, in fact the components showing high consistency in the spatial representation along the acquisition had higher probability to be associated with MU activity.

6.2 Relevance and future works

This PhD project describes a new approach for identifying and evaluating the mechanical and electrical properties of MUs. It is now possible to associate the decomposed MUAPs to a specific muscle or muscle region by identifying the MU territory within the muscle cross-section. This is important for understanding the relationship between neural and physical MU properties and can be used to improve musculoskeletal models since it may provide an experimental foundation for the definition of the model parameters. While MUs' electrical properties and behaviors have been the subject of extensive study over the years, in vivo research into their location and mechanical response to excitation are still in the early stages. If we want to address acknowledged gaps in our knowledge of how entire muscles convert brain commands activating contractile cells into contractions and how neural and mechanical variables interplay to generate force and movement, this is a critical step forward.

The proposed approach can provide new tools to investigate both fundamental aspects of MU and muscle function (e.g., to inform the enhancement of finite element models of

muscle), and the changes caused by aging (e.g., MU loss and muscle weakness), as well as neuromuscular diseases (e.g., Motor Neuron Diseases). These applications can benefit from this multi-modal approach and on its possible future evolutions. In fact, although the focus of this investigation was the identification of the MU fibers location, the technique offers the opportunity to develop methods for quantifying the area or spatial contours together with estimating the mean tissue velocity temporal profile (twitch) and its relationship with MU territory. Moreover, the observed mismatch between electrical and mechanical events within the same muscle volume suggests a relevant difference in the spatial sensitivity of the two techniques (EMG and US), that could be exploited to improve decomposition methods based on integrated EMG and US detections.

Future research is necessary to better describe the effect of different factors that may limit the applicability of the proposed approach to conditions other than those tested in this project. For instance, it is unknown how much variables like physical changes in muscle length and tissue characteristics (such as fibrosis, and adipose tissue infiltration), affect the physical muscle tissue MU representation. In this study, tissue velocity sequences were used to indirectly estimate the MU physical properties. It is important to note that in the studies presented here tissue velocities were estimated along one direction (i.e. superficial-depth). The contraction and relaxation of a group of fibers is known to exert force on the adjacent fibers and connective tissue creating complex dynamics in both directions. The investigation in the medio-lateral direction would help to enlighten the interactions between active and non-active tissue. Furthermore, this 2D tissue velocities could increase the sensitivity of decomposition algorithms for the identification of MUs which, as mentioned in this thesis, are affected by the non-linearities of the system. The multi-modal approaches, like the ones described in this thesis, can significantly contribute to answer such questions and represent a chance for new research in this field to be accomplished.

6.3 References

[1] A. Holobar and D. Zazula, ‘Multichannel blind source separation using convolution Kernel compensation’, *IEEE Trans. Signal Process.*, vol. 55, no. 9, pp. 4487–4496, 2007, doi: 10.1109/TSP.2007.896108.

[2] W. Herzog, ‘Skeletal muscle mechanics: questions, problems and possible solutions’, *J. NeuroEngineering Rehabil.*, vol. 14, no. 1, p. 98, Dec. 2017, doi: 10.1186/s12984-017-0310-6.

[3] J. M. Wakeling *et al.*, ‘The Energy of Muscle Contraction. I. Tissue Force and Deformation During Fixed-End Contractions’, *Front. Physiol.*, vol. 11, 2020, doi: 10.3389/fphys.2020.00813.

[4] H. Degens, J. Attias, D. Evans, F. Wilkins, and E. HodsonTole, ‘The mobility limitation in healthy older people is due to weakness and not slower muscle contractile properties’, *PLoS ONE*, vol. 16, no. 6 June, 2021, doi: 10.1371/journal.pone.0253531.

[5] P. J. Harding, I. D. Loram, N. Combes, and E. F. Hodson-Tole, 'Ultrasound-Based Detection of Fasciculations in Healthy and Diseased Muscles', *IEEE Trans. Biomed. Eng.*, vol. 63, no. 3, pp. 512–518, 2016, doi: 10.1109/TBME.2015.2465168.

[6] T. Deffieux, J. L. Gennisson, M. Tanter, and M. Fink, 'Assessment of the mechanical properties of the musculoskeletal system using 2-D and 3-D very high frame rate ultrasound', *IEEE Trans. Ultrason. Ferroelectr. Freq. Control*, vol. 55, no. 10, pp. 2177–2190, 2008, doi: 10.1109/TUFFC.917.

[7] E. Lubel et al., 'Non-linearity in motor unit velocity twitch dynamics: Implications for ultrafast ultrasound source separation'. bioRxiv, p. 2023.03.24.533983, Mar. 25, 2023. doi: 10.1101/2023.03.24.533983.

List of Publications (2019-2023)

Peer-reviewed publications in international journals

1. **M. Carbonaro**, O. R. Seynnes, N. A. Maffiuletti, C. Busso, M. A. Minetto, and A. Botter
   Architectural changes in superficial and deep compartments of the tibialis anterior during electrical stimulation over different sites
   IEEE Trans. Neural Syst. Rehabil. Eng Sci. Rep., 2020, 28(10), 2557–2565.

2. A. Botter, T. Vieira, **M. Carbonaro**, G. L. Cerone, and E. F. Hodson-Tole
   Electrodes' Configuration Influences the Agreement between Surface EMG and B-Mode Ultrasound Detection of Motor Unit Fasciculation
   IEEE Access, 2021, 9, 98110–98120.

3. **M. Carbonaro**, K. M. Meiburger, S. Seoni, E. F. Hodson-Tole, T. Vieira, and Alberto Botter
   Physical and electrophysiological motor unit characteristics are revealed with simultaneous high-density electromyography and ultrafast ultrasound imaging
   Sci. Rep., 2022, 12(1), 8855.

4. R. Rohlén†, **M. Carbonaro**†, G. L. Cerone, K. M. Meiburger, A. Botter, and C. Gronlund
   Spatially repeatable components from ultrafast ultrasound are associated with motor unit activity in human isometric contractions
   Accepted in *J. Neural Eng.*, 2023, preprint in bioRxiv 2023.04.17.537211.
   † R. Rohlén and M. Carbonaro equally contributed to this study

Peer-reviewed international conference proceedings

1. A. Botter, **M. Carbonaro**, T. M. Vieira, and E. F. Hodson-Tole
   Identification of muscle fasciculations from surface EMG: comparison with ultrasound-based detection
   41st Annu. Int. Conf. IEEE Eng. Med. Biol. Soc. EMBC, 2019, 5117–5120.

2. A. Giangrande , M. Viganò, **M. Carbonaro**, M. Gilardone, P. Tropea, G.L. Cerone, M. Corbo, M. Gazzoni, A. Botter
   Swallowing onset detection : comparison of endoscopy- and accelerometry-based estimations
   IFMBE Proceedings, 2021, 1–10.

3. **M. Carbonaro**, S. Zaccardi, S. Seoni, K. M. Meiburger, and A. Botter
   Detecting anatomical characteristics of single motor units by combining high density electromyography and ultrafast ultrasound: a simulation study *
   IEEE Eng. Med. Biol. Soc. Annu. Int. Conf., 2022, 748–751.
   * Awarded paper: selection as finalist of the Student Paper Competition

4. **M. Carbonaro**, R. Rohlén, S. Seoni, K.M. Meiburger, T. Vieira, C. Grönlund, A. Botter
   Combining high-density electromyography and ultrafast ultrasound to assess individual motor unit properties in vivo
   VIII Congress of the National Group of Bioengineering (GNB), 2023.

Conference abstracts

1. **M. Carbonaro**, M.A. Minetto, O.R. Seynnes, N.A. Maffiuletti, and A. Botter
   Effect of electrical stimulation site on architectural changes and fatigue of tibialis anterior
   Proc. XX Congr. della Soc. Ital. di Anal. dell Mov. Clin., 2019.

2. **M. Carbonaro**, G. Agostinelli, G. L. Cerone, and A. Botter,
   Feasibility of interleaved stimulation in peroneal stimulators: the effect of surface electrode configuration on foot kinematics
   Proc. XXII Congr. della Soc. Ital. di Anal. dell Mov. Clin, Gait Posture, 2022.

3. **M. Carbonaro**, K. M. Meiburger, S. Seoni, E. F. Hodson-Tole, T. Vieira, and A. Botter
   Detecting electrical and mechanical motor unit characteristics using high density electromyography and ultrafast ultrasound
   XXIV ISEK Congress, 2022.